AD_____

AWARD NUMBER: DAMD17-00-1-0291

TITLE: A Training Program in Breast Cancer Research Using NMR Techniques

PRINCIPAL INVESTIGATOR: Paul C. Wang, Ph.D.

CONTRACTING ORGANIZATION: Howard University
                          Washington, DC 20059

REPORT DATE: July 2006

TYPE OF REPORT: Final

PREPARED FOR: U.S. Army Medical Research and Materiel Command
              Fort Detrick, Maryland 21702-5012

DISTRIBUTION STATEMENT: Approved for Public Release;
                        Distribution Unlimited

The views, opinions and/or findings contained in this report are those of the author(s) and should not be construed as an official Department of the Army position, policy or decision unless so designated by other documentation.

REPORT DOCUMENTATION PAGE

Form Approved
OMB No. 0704-0188

Public reporting burden for this collection of information is estimated to average 1 hour per response, including the time for reviewing instructions, searching existing data sources, gathering and maintaining the data needed, and completing and reviewing this collection of information. Send comments regarding this burden estimate or any other aspect of this collection of information, including suggestions for reducing this burden to Department of Defense, Washington Headquarters Services, Directorate for Information Operations and Reports (0704-0188), 1215 Jefferson Davis Highway, Suite 1204, Arlington, VA 22202-4302. Respondents should be aware that notwithstanding any other provision of law, no person shall be subject to any penalty for failing to comply with a collection of information if it does not display a currently valid OMB control number. **PLEASE DO NOT RETURN YOUR FORM TO THE ABOVE ADDRESS.**

1. REPORT DATE *(DD-MM-YYYY)*	2. REPORT TYPE	3. DATES COVERED *(From - To)*
01-07-2006	Final	1 Jul 2000 – 30 Jun 2006

4. TITLE AND SUBTITLE

A Training Program in Breast Cancer Research Using NMR Techniques

5a. CONTRACT NUMBER

5b. GRANT NUMBER
DAMD17-00-1-0291

5c. PROGRAM ELEMENT NUMBER

6. AUTHOR(S)

Paul C. Wang, Ph.D.

E-Mail: pwang@howard.edu

5d. PROJECT NUMBER

5e. TASK NUMBER

5f. WORK UNIT NUMBER

7. PERFORMING ORGANIZATION NAME(S) AND ADDRESS(ES)

Howard University
Washington, DC 20059

8. PERFORMING ORGANIZATION REPORT NUMBER

9. SPONSORING / MONITORING AGENCY NAME(S) AND ADDRESS(ES)
U.S. Army Medical Research and Materiel Command
Fort Detrick, Maryland 21702-5012

10. SPONSOR/MONITOR'S ACRONYM(S)

11. SPONSOR/MONITOR'S REPORT NUMBER(S)

12. DISTRIBUTION / AVAILABILITY STATEMENT
Approved for Public Release; Distribution Unlimited

13. SUPPLEMENTARY NOTES

14. ABSTRACT

This is a six year training program in breast cancer research using NMR techniques. This program has supported seven predoctoral students and five postdoctoral students. All the trainees have learned the theory and instrumentation of MRI. They have been actively involved in one of the seven research projects: (1) NMR studies of phosphorus metabolites of breast cancer cells using an improved cell perfusion system (2) Segmentation of mammographic masses (3) Establishment of an image database for computer-aided-diagnosis (CAD) research development (4) F19 NMR detection of trifluoperazine crossing Blood-Brain-Barrier through Pgp modulation (5) Tumor-targeted MR Contrast Enhancement by Anti-transferrin Receptor scFv-Immunoliposome Nanoparticles (6) MRI and histological correlations of cortical brain volumes in APP/PS1 mice (7) Enhanced molecular imaging with fused optical and MRI images. The trainees have attended the weekly seminars in the Cancer Center and also attended a special NMR seminar series in the Department of Radiology. Eight papers have been published and 16 abstracts have been presented in the national and international meetings. Five grants including a USAMRMC postdoctoral award have received.

15. SUBJECT TERMS
Training, Nuclear Magnetic Resonance, Breast Cancer

16. SECURITY CLASSIFICATION OF:			17. LIMITATION OF ABSTRACT	18. NUMBER OF PAGES	19a. NAME OF RESPONSIBLE PERSON USAMRMC
a. REPORT	b. ABSTRACT	c. THIS PAGE			19b. TELEPHONE NUMBER *(include area code)*
U	U	U	UU	86	

Standard Form 298 (Rev. 8-98)
Prescribed by ANSI Std. Z39.18

Table of Contents

A Training Program In Breast Cancer Research Using NMR Techniques

I.   INTRODUCTION

The purpose of this proposal was to develop a research training program in breast cancer research at Howard University Cancer Center utilizing nuclear magnetic resonance (NMR) imaging and spectroscopy techniques. This program was a multidisciplinary consortium of five departments including College of Medicine MD/PHD program, Radiology, Radiation Oncology, Biology and Electrical Engineering. Through this program, we have trained seven predoctoral students and five postdoctoral students in six years. The predoctoral students were either from the MD/PhD program or from the Department of Electrical Engineering. The MD/PhD program is a seven-year program in which the students do research in the Department of Biochemistry and Molecular Biology. The postdoctoral fellows were from a medical or physical science background with strong interests in breast cancer research. All the students have participated in the research projects conducted in the Biomedical NMR Laboratory. In the later years of the program, the postdoctoral fellows were encouraged to develop their own research projects. Although the research component of the training was focused on NMR applications in breast cancer research, the trainees received a broad exposure to other aspects of breast cancer research through a rigorous curriculum, interactions with faculty, and participation in seminars and other research activities in the Howard University Cancer Center. The program was flexible and tailored to the trainees' backgrounds to ensure the trainees receive a well-rounded education. This program has accomplished its goal to provide an educational and research opportunity to promising young African-American students to become productive breast cancer researchers.

II.   BODY

Statement of Work   (All the tasks in the Statement of Work have completed).

For Predoctoral Students

Year 1:
- Introduction to the Biomedical NMR Laboratory and Cancer Center. Meeting with mentors to learn the on-going breast cancer projects (months 1 - 3)
- Learn NMR instruments (months 4 -12)
- Start departmental course work with the respective department (months 4 - 12)
- Seminar presentation by the student each semester (months 4 - 12)
- Clinical preceptorship one half day per week (months 4 - 12)
- Report to MD/PhD committee and respective department on research progress (month 12)

Year 2-3:
- Take departmental comprehensive exams (months 13 - 15)
- Submit a five page pre-proposal 30 days before taking comprehensive exam (months 13-15)
- Write an expanded research proposal and defend the proposal (months 16-18)
- Once the student has passed the written and oral comprehensive exams, the student is qualified as a Ph.D. candidate

- Select a thesis committee (month 18)
- Start thesis project (month 18)
- Report to MD/PhD committee and respective department on research progress each semester (months 18 - 36)
- Clinical preceptorship one half day per week (months 13 - 36)

Year 4:
- Conclude the thesis project and write up thesis (months 37 - 42)
- Thesis defense and writing of scientific papers for publication (month 43 - 48)

For Postdoctoral Students:

Year 1:
- Introduction to the Biomedical NMR Laboratory at the Cancer Center. Meeting with mentors to learn the on-going projects (months 1-2)
- Participate in weekly Cancer Center Seminars (months 1-2)
- Learn to use three NMR instruments in the laboratory (months 1-12)
- Take cell biology course taught by Dr. Bremner and NMR course taught by Dr. Wang (months 3-12)
- Select an on-going project and start to get involved with the research project (months 4-12)

Year 2:
- Participate in weekly Cancer Center Seminars (months 13-24)
- Organize weekly research group meeting (months 13-24)
- Continue research project (month 13-24)
- Present progress report to the Executive Committee (months 18 and 24)
- Clinical preceptorship one half day per week (months 13-24)

Years 3-4:
- Select a new research project approved by the Executive Committee (months 25-27)
- Clinical preceptorship one half day per week (months 25-48)
- Conduct the new research project (months 28-48)
- Present progress report to the Executive Committee once every six months (months 28-48)
- Present research results to the Cancer Center faculty and National Meeting
- Write scientific papers

Students trained in this program:

Pre-doctoral students: (graduate program, current position)

Emmanuel Agwu (MD/PhD, Biochemistry, internal medicine resident at HUH)
O'tega Ejofodomi (Electrical Engineering, graduate student at HU)
Lisa Kinnard (Electrical Engineering, researcher at FDA)
Raymond Malveaux (medical student at Howard University)
Armand Oei (Biology, student at New England School of Optometry)
Shani Ross (Electrical Engineering, graduate student at U Michigan)
Furia Thomas (Electrical Engineering, graduate student at Catholic University)

Postdoctoral students: (current position)

Yusuf Ali, MD (radiology resident at Howard University Hospital)
Ercheng Li, PhD (staff, Chemistry Department, Georgetown University)
Huafu Song, MS (Engineer, NMR industry)
Jianwei Zhou, PhD (assistant professor, Quiyang Normal University, China)
Renshu Zhang, MD (research associate, Department of Radiation Oncology, HUH)

Research Projects

In this training grant, students have participated in seven research projects listed as follows:

(1)   NMR Studies of Phosphorus Metabolites of Breast Cancer Cells Using an Improved Cell Perfusion System

P^{31} NMR has been used to study the high energy phosphorus metabolites in tumors. It can be used to monitor the effectiveness of cancer treatment. Since the NMR signals of the phosphorus metabolites in cells are weak and the NMR study usually are long. During the long data acquisition time, the cancer cells need to be maintained in a good living environment. In this project, we developed an improved NMR cell-perfusion system, which was used to study the phosphorus metabolites of breast cancer cells for an extended period. The improved perfusion system is driven by a peristaltic pump. The portion of the system before the pump is under negative pressure, and the portion after the pump is under positive pressure. This design helps the removal of air bubbles trapped in the perfusion medium and avoid the degradation of the quality of NMR spectrum. Using this perfusion system, NMR study of the breast cancer cells can be extended for more than a week not hours as it used to be. The P^{31} NMR spectrum of the wild type MCF7 breast cancer cells shows three distinct phases, which reflect the proliferation of the cells. Study of oxygenation of the agarose-encased cells in this perfusion system suggests that the cells utilized aerobic respiration. The ability for this perfusion system to maintain cells viable for more than a week allowed us to determine the longitudinal relaxation times (T1 values) of the P^{31} metabolites of MCF7/WT cells in vitro. A progressive saturation recovery NMR technique was used for T1 measurement. Accurate T1 values are crucial in designing P^{31} MRS studies. This study has demonstrated that the long time bubble-free NMR cell perfusion system could be a useful tool for in vitro breast cancer research.

(2)   Segmentation of Mammographic Masses

Mammography combined with a clinical examination is a standard method used for the detection and diagnosis of breast cancer. However, mammography alone can produce a high percentage of false positives. A computer-aided diagnostic (CADx) system can serve as a more accurate clinical tool for the radiologist, consequently lowering the rate of missed breast cancer and ultimately lowering morbidity and mortality. Breast cancer can exist not only in the form of masses, but also in the forms of microcalcifications, asymmetric density, and architectural distortion. These abnormalities can be seen using imaging techniques such as mammography, ultrasound and magnetic resonance imaging (MRI). Breast images have different appearances based upon their amounts of fibroglandular and fatty tissue. Fibroglandular tissue usually consists of a combination of breast glands (lobules), ducts, and surrounding fibrosis (fibrous connective tissue and scarring). It appears denser or brighter than fatty tissue on mammograms

due to its higher x-ray attenuation. The diseased tissue usually also becomes denser over time. Masses can have unclear borders and are sometimes overlapped with glandular tissue in mammograms; therefore, the radiologists can overlook them during their search for suspicious areas. Proper segmentation to include the shape and boundary characteristics is an essential step in aiding the computer for the analysis and malignancy determination of the mass. While many CAD_x systems have been developed, the development of effective image segmentation algorithms for breast masses remains unsolved in this field, particularly in the cases where the breast tissue is dense. Since cancerous masses often appear to be light and have ill-defined borders, it is quite challenging for mammographers to extract them from surrounding tissue. It is even more difficult to automatically segment masses from dense tissue. In this study, a fully automated segmentation algorithm has been developed. It delineates the complete mass as with minimum normal structures in dense and mixed tissue mammograms.

(3)   Establishment of an Image Database for Computer-Aided-Diagnosis (CADx) Research Development

The success of CADx is based on the accuracy and completeness of the mammographic image database, of which the CADx extracts the features of different types of pathology. The current available mammographic image databases are all obtained from the Caucasian population. There are very few African American cases. It is well known that African American women generally have denser breasts. The appearance of mammograms from African American breast cancer patients may not be the same as those images from Caucasian breast cancer patients. Howard University Cancer Center has a well maintained cancer registry. It has more than 200 new African American breast cancer cases each year. We have digitized more than 5000 images from 260 patients' records using a high resolution Kodak LS85 laser scanner. The database system and web-based search engine were developed using MySQL and PHP. The database has been evaluated by medical professionals and the experimental results obtained are promising with high image quality and fast access time. We have also developed an image viewing system, D-Viewer, to display these digitized mammograms. This viewer is coded in Microsoft Visual C++ and is intended to help medical professionals view and retrieve large data sets in near real time. Finally, we have developed an image content-based retrieval function for the database system in order to provide improved search capability for the medical professionals.

(4) F^{19} NMR Detection of Trifluoperazine Crossing Blood-Brain-Barrier Through Pgp Modulation

Cancer patients are often treated with combination therapy for secondary symptoms such as depression, and cardiopulmonary diseases. The potential for drug-drug interaction under these conditions is high. Such interactions may cause changes in the pharmacokinetics, especially for drugs with narrow therapeutic indices. These changes can alter efficacy and toxicity of the administered drugs. Drug-drug interactions may occur due to common metabolic pathways, but also due to interference at the P-glycoprotein (Pgp) level. Pgp, a nonspecific transport protein, is expressed constitutively at the blood-brain-barrier (BBB), intestine, kidney, liver, and in activated T-cells. Interaction at the blood-brain-barrier may occur if one of the two concomitantly administered drugs blocks Pgp thus allowing the other drug to retain in the brain or increase in brain uptake of therapeutic drugs. The potential for drug-drug interactions is not routinely studied at the Pgp level during drug development. Its presence is assumed only after unexpected clinical symptoms. We have shown using a dynamic NMR method based on

detection of a fluorinated drug, trifluoperazine (TFP), in the brain, in combinations with an immune suppressor, cyclosporin A to demonstrate drug penetration across blood-brain-barrier after Pgp modulation.

(5)   Tumor-targeted MR Contrast Enhancement by Anti-transferrin Receptor scFv-Immunoliposome Nanoparticles

The development of improvements in MRI that would enhance sensitivity, thus leading to earlier detection of cancer and visualization of metastatic disease, is an area of intense exploration. In this study, we developed the cationic immunoliposome system that includes an anti-transferrin receptor single chain antibody fragment (TfRscFv) as the targeting molecule was used to encapsulate the MR contrast agent gadolinium (TfRscFv-Lip-GAD-d) for specific targeting to cancer cells and MR contrast enhancement. This system was evaluated for in vivo MR imaging in MDA-MB-435 breast cancer cells growing as solid tumor xenografts in athymic nude mice. The TfRscFv-Lip-GAD-d complex was administered intravenously at an encapsulated contrast agent. The MRI signal intensity of tumors was significantly enhanced compared to free contrast agent and the enhancement was closely related to the pathology of the tumors. These results indicate that this TfRscFv-Lip-GAD-d system significantly enhances the image contrast in solid tumors and is much superior to the contrast agent alone for identifying the tumor pathological features. This targeted immunoliposome system may serve as a powerful MR imaging probe for early detection and differential diagnosis of tumors.

(6)   MRI and Histological Correlations Of Cortical Brain Volumes In APP/PS1 Mice

Quantitative analyses indicate that brain atrophy on ante-mortem neuroimages and post-mortem tissue strongly correlates with the severity of cognitive impairment in Alzheimer's disease (AD). The absence of cortical atrophy in the age-matched, non-demented elderly suggests that volumetric studies of ante-mortem neuroimages may provide an early marker of AD in aging populations. In this study we used design-based stereology to quantify cortical volumes in double transgenic mice that deposit AD-type mutant ß-amyloid proteins (Aß) in cortical tissue. Spin-echo T1-weighted, high-resolution magnetic resonance imaging (MRI) was applied to the brain of male and female double transgenic mice aged 4-28 months of age that co-express AD-type mutations in amyloid precursor protein (APP) and presenilin-1 (PS-1), and, age-matched non-tg littermate controls (wild-type, WT). From a systematic-random series of coronal MRI images, total volumes of the hippocampal formation (V_{HF}) and whole brain (V_{brain}) were quantified by the Cavalieri-point counting method. The same sampling and estimation methods were used to quantify the same brain regions after perfusion and tissue processing. Strong correlations were found between V_{HF} and V_{brain} estimates from MRI images and histological sections. Agonal and tissue processing changes accounted for about 65 to 75% differences in cortical volumes between *in situ* and coverslipped sections. No differences were present in mean V_{HF} or mean V_{brain} for dtgAPP/PS1 compared to WT mice. These stereological studies of MRI neuroimages and postmortem tissue do not show cortical atrophy in association with widespread cortical deposition of AD-type amyloid plaques in aged dtg APP/PS1 mice, in contrast to the severe cortical atrophy in AD. Future studies with dtgAPP/PS1 mice will explore the possibility that high contrast ligands bound to mutant Aß proteins associated with amyloid plaques could facilitate early diagnosis of AD by ante-mortem neuroimaging.

(7)   Enhanced Molecular Imaging with Fused Optical and MRI Images

Improvement in molecular and cell biology techniques in recent years have had remarkable impact on our understanding of the cellular and molecular mechanisms of biological processes and the underlie development of diseases. Significant development have been made in noninvasive, high-resolution, in vivo imaging modalities such as positron emission tomography (PET), magnetic resonance imaging (MRI), and optical imaging (OI) for better diagnosis of patients, and imaging of cells and small animals of diseased models. In vivo molecular imaging, which utilizes these two fronts, opens up extraordinary opportunities for basic scientists and clinicians to study diseases, and in many cases, quantitatively at the molecular level. The early assessment of illness depends on anatomic and physiological changes of the disease, which are a late manifestation of the molecular changes that truly triggers the disease. Imaging early molecular changes at "predisease states" would be useful in patient care and management by allowing much earlier detection of the disease, designing more effective drugs, and evaluation of therapy. This research is to combine the strength of MRI and optical imaging modalities for better spatial and functional information in small animal imaging. The technique would be useful to evaluate targeting specificity of near infrared dye conjugated ligands in molecular imaging of tumor bearing animals.

III.   KEY RESEARCH ACCOMPLISHEMENTS

Year 1 (2000-01)
- An improved NMR cell-perfusion system driven by peristaltic pump was constructed. This system totally eliminated the air bubbles from the perfusion medium.
- The cell viability study of the MCF-7 breast cancer cells was extended successfully from hours to more than a week.

Year 2 (2001-02)
- Intravascular MRI contrast agent has been used to detect high blood flow, vascular density, and capillary permeability of tumors.
- Dynamic MRI contrast enhancement is an important parameter for tumor characterization, and it correlates well with histopathological findings.
- Using pixel aggregation and likelihood analysis techniques, the segmentation method can delineate the tumor body as well as tumor peripheral regions covering typical mass boundaries and some speculation patterns.

Year 3 (2002-03)
- We found that the maximum likelihood method in conjunction with fuzzy shadow approach is an effective approach not only for segmenting masses in mammogram, but also for using its results to separate malignant and benign masses.
- We have demonstrated that cyclosporin A, an immune suppressor, enhances the drug penetration through the blood-brain-barrier.

Year 4 (2003-04)
- A fully automated segmentation algorithm for Computer-Aided-Diagnosis has been developed. It delineates the complete masses with minimum normal structures in dense and mixed tissue mammograms.
- Drug penetration of trifluoperazine through the blood-brain-barrier due to Pgp modulation was detected using a dynamic in vivo F^{19} NMR method.

- Utilizing a well maintained cancer registry at the Howard University Cancer Center, mammograms from more than 200 African American breast cancer patients were digitized to establish a breast cancer image database. It will be available on the Internet to the CADx software developers and researchers.
- Developed a TfR scFv-immunoliposome system to be used as a MR contrast agent delivery vehicle for improving affinity and specificity of contrast agent to tumor association.

Year 5 (2004-05)

- An improved NMR cell-perfusion system was developed. It has been used to study the phosphorus metabolites of breast cancer cell for an extended period longer than one week. Using this perfusion system, the T1 relaxation times of phosphorus metabolites were accurately measured.
- The image digitization of more than 1000 mammograms from 220 African American breast cancer patients has completed. This huge image database is available to be used in the further development of Computer-Aided-Diagnosis system.
- MRI contrast agent is incorporated into an anti-transferrin receptor single chain antibody (TfRsc) liposome nanoparticle for MRI molecular imaging. This significantly improves the image contrast between tumor and surrounding tissues. This improves the specificity of MRI imaging of tumor.

Year 6 (2005-06)

- Based on the finished mammography database of 260 African American (40 more cases), two previously supported students, Ms. Ross and Ms Ejofodomi wrote a paper entitled "A Mammography Database and View System for African American Patients". The paper has been submitted to the Journal of Digital Imaging for publication. This huge image database is available to be used in the further development of Computer-Aided-Diagnosis system.
- A graduate student, Mr. Furia Thomas, has worked on a project for image fusion of MRI images and optical images. The MRI images provide detail anatomical information and the optical images provide functional information of the tissue. The greater imaging sensitivity of optical imaging technique can be complemented by the high resolution MRI images when these two images are fused together. Mr. Thomas has submitted an abstract entitled "Enhanced Molecular Imaging with Fused Optical and MRI Images" to the 28th IEEE Engineering in Medicine and Biology Conference Management System, July 2006.
- The PI has continued developing the nanosize cationic immunoliposome system that includes an anti-transferrin receptor single chain antibody fragment (TfRscFv) as the targeting molecule was used to encapsulate the MR contrast agent gadolinium-DTPA (TfRscFv-Lip-GAD-d) for specific targeting to cancer cells and MR image contrast enhancement. This system was evaluated for MR imaging of breast cancer cells in vitro as well as in vivo. The signal intensity of tumors was significantly enhanced compared to free contrast agent and the enhancement was closely related to the pathology of the tumors.

IV.   REPORTABLE OUTCOMES

Research

Reprints (Listed in the Appendices section)
1. Kinnard L, Lo S-C.B, Wang P, Freedman MT, Chouikha M, Separation of Malignant and Benign Masses in Mammography using Maximum-Likelihood Modeling and Neural Networks. Proc. of SPEI Vol 4684: 733-741, 2002.
2. Lo S-C.B, Li H, Wang Y, Kinnard L, Freedman M, A Multiple Circular Path Convolution Neural Network System for Detection of Mammographic Masses, IEEE Transactions on Medical Imaging, Vol 21, No 2 pp 150-158. 2002
3. Kinnard L, Lo S-C B, Wang PC, Freedman MT, Chouikha M, Automatic Segmentation of Mammographic Masses Using Fuzzy Shadow and Maximum-likelihood Analysis, Proc of IEEE Symposium on Biomedical Imaging (Cat 02EX608C): pp. 241-244, 2002.
4. Kinnard L, Lo S-C.B, Wang PC, Freedman MT, Chouikha M, Separation of Malignant and Benign Masses Using Image and Segmentation Features. Proc. of SPIE, 2003
5. Kinnard L, Lo SB, Makariou E, Osicka T, Wang PC, Freeman M, Chouikha M. Likelihood Function Analysis For Segmentation of Mammographic Masses For Various Margin Groups. Proc of IEEE Symposium on Biomedical Imaging. pp 113-116, 2004.
6. Liang XJ, Yin JJ, Zhou JW, Wang PC, Taylor B, Cardarelli C, Kozar M, Forte R, Aszalos A, Gottesman M. Changes in Biophysical Parameters of Plasma Membranes Influence Cisplatin Resistance of Sensitive and Resistant Epidermal Carcinoma Cells. Exp Cell Research 293:283-291, 2004.
7. Kinnard L, Lo SB, Makariou E, Osicka T, Wang P, Chouikha MF, Freedman MT. Steepest changes of a probability-based cost function for delineation of mammographic masses: A validation study. Med. Phys. 31(10):2796-2810, 2004.
8. Pirollo K, Dagata J, Wang PC, Freedman M, Vladar A, Fricke S, Ileva L, Zhou Q, Chang EH. A Tumor-Targeted Nanodelivery System to Improve Early MRI Detection of Cancer. J Mol Imaging 5(1):41-52, 2006.

Presentations
1. Zhou JW, Agwu CE, Li EC, Wang PC. An Improved NMR Perfusion System For Breast Cancer Cell Study. 42nd Experimental NMR Conference, March 11-16, 2001, Orlando, FL.
2. Ting P, Wang PC, Kinnard L, Herman MM, Cohn R. Early EEG and Diffusion MRI (dMRI) Changes in an Experimental Model of Severe Periventircular Leukomalacia (PVL). The Annual Pediatric Academic Societies Meetings, May 1-5, 2001, Baltimore, MD.
3. Agwu EC, Zhou JW, Sridhar R, Wang PC. An Improved NMR Perfusion System For Breast Cancer Cell Study. Association For Academic Minority Physicians 15th Annual Scientific Meeting, October 12-14, Washington, DC. 2001.
4. Zhang RS, Li EC, Ali YD, Song HF, Fan KJ, Pirollo KF, Chang EH, Wang PC. Dynamic Magnetic Resonance Imaging of Prostate Cancer in Mice. American Association for Cancer Research Conference, Molecular Imaging in Cancer: Linking Biology, Function, and Clinical Application In Vivo, January 23-27, 2002, Orlando, Fl.
5. Kinnard L, Lo S-C.B, Wang P, Freedman MT, Chouikha M, Separation of Malignant and Benign Masses in Mammography using Maximum-Likelihood Modeling and Neural Networks. SPEI Med Imaging, Feb. 2002, San Diego, CA.
6. Kinnard L, Lo S-C B, Wang PC, Freedman MT, Chouikha M. A Maximum-likelihood

Automated Approach to Breast Mass Segmentation. 2002 1st IEEE International Symposium on Biomedical Imaging: Macro to Nano, Washington, DC, July 7-10, 2002.

7. Kinnard L, Lo S-C B, Wang PC, Freedman MT, Chouikha M. Likelihood Features with Circular Processing-based Neural Network for the Enhancement of Mammographic Mass Classification. SPIE Medical Imaging Conference. San Diego, CA, February, 2003.

8. Wang PC, Aszalos A, Li E, Zhang R, Song H. A Pharmacokinetic Study of Trifluoperazine Crossing Blood-Brain-Barrier Due to P-glycoprotein Modulation. ISMRM, Workshop on Dynamic Spectroscopy and Measurement of Physiology and Function. September 6-8, 2003, Orlando, Fl.

9. Kinnard L, Lo SB, Makariou E, Osicka T, Wang PC, Freeman M, Chouikha M. Likelihood Function Analysis For Segmentation of Mammographic Masses For Various Margin Groups. International Society of Biomedical Imaging, April 15-18, 2004, Arlington, VA.

10. Wang PC, Aszalos A, Li E, Zhang R, Song H, Malveaux R. A NMR Study of Trifluoperazine Crossing Blood-Brain-Barrier Due to P-glycoprotein Modulation. ISMRM 12th Annual Meeting, May 17-21, 2004, Kyoto, Japan.

11. Wang PC, Li E, Zhang R, Song H, Pirollo K, Chang EH. MR Image Enhancement by Tumor Cell Targeted Immunoliposome Complex Delivered Contrast Agent. Society for Molecular Imaging 3rd Annual Meeting, September 9-12, 2004, St. Louis, MO.

12. Manaye KF, Wang PC, O'Neil J, Oei A, Song H, Tizabi Y, Ingram DK, Mouton PR. In vivo and In vitro Stereological Analysis of Hippocampal and Brain Volumes in Young and Old APP/PS1 Mice Using Magnetic Resonance Neuroimages. Society of Neuroscience 34th Annual Meeting, October 23-27, 2004 San Diego, CA.

13. Wang PC, Aszalos A, Li E, Zhang R, Song HF, Malveaux R. Increased Transport of Trifluoperazine Across the Blood-Brain-Barrier Due to Modulation of P-glycoprotein. 9th RCMI International Symposium on Health Disparities. December 8-11, 2004, Baltimore, MD.

14. Agwu CL, Zhou J, Li E, Sridhar R, Wang PC. NMR Studies of Phosphorus Metabolites of Breast Cancer Cells Using An Improved Cell Perfusion System Applications for the Improved NMR Perfusion System for Breast Cancer Cell Study. 9th RCMI International Symposium on Health Disparities. December 8-11, 2004, Baltimore, MD.

15. Manaye KF, Wang PC, O'Neil J, Oei A, Song HF, Tizabi Y, Ingram DK, Mouton PR. In-Vivo and In-vitro Stereological Analysis of Hippocampal and Brain Volumes in Young and Old APP/PS1 Mice Using Magnetic Resonance Neuroimages. 9th RCMI International Symposium on Health Disparities. December 8-11, 2004, Baltimore, MD.

16. Wang PC, Pirollo K, Song HF, Shan L, Bhujwalla Z, Chang E. Evaluation of Transferrin Receptor Targeted Immunoliposome Contrast Agent Delivery System for In Vivo MR Imaging in Solid Tumor Xenografts. The Society of Molecular Imaging 4th Annual Meeting, September 7-10, 2005, Cologne, Germany.

Career Development

Degrees Awarded
1. Mr. Emmanuel Agwu, an MD/PhD student, received a MD degree from the School of Medicine in June 2003.

2. Ms. Lisa Kinnard received a PhD degree in June 2003 from the Department of Electrical Engineering. Her PhD thesis title is "Segmentation of Malignant and Benign Masses in Digitized Mammograms Using Region Growing Combined with Maximum-Likelihood".
3. Mr. Raymond Malveaux received a MD degree from the School of Medicine in June 2005.
4. Ms. Shani Ross received her B.S. degree in June 2004 from the Department of Electrical Engineering. She went to a graduate program in the Department of Biomedical Engineering at University of Michigan.
5. Ms. O'tega Ejofodomi received her B.S. degree in June 2004 from the Department of Electrical Engineering. She went to a graduate program in the Department of Electrical Engineering at the Howard University pursuing medical imaging research.

Employment/Research Positions
1. Mr. Armand Oei is going to attend professional school at the New England School of Optometry, 2005.
2. Dr. E. Chikezirim Agwu has entered a residency program at Howard University Hospital, 2006.
3. Dr. Lisa Kinnard has joined FDA as a research scientist to continue the CADX work, 2006.

Awards

1. Mr. Emmanuel Agwu received the Association for Academic Minority Physician, 2001 Minority Medical Student Research Summer Fellowship, a Merck/AAMP scholarship.
2. Mr. Emmanuel Agwu received a 2001 Scandrett Scholarship Award, a scholarship for disable students.
3. Dr. Wang (PI) was chosen as a recipient of an AACR-HBCU Faculty Scholar Award in Cancer Research for the AACR Special Conference entitled "Molecular Imaging in Cancer: Linking Biology, Function, and Clinical Application In Vivo" held January 23-27, 2002 Lake Buena Vista, Fl.

Funding Received:

1. Computer-Aided Detection of Mammographic Masses in Dense Breast Images. US Army Medical Command Post-Doctoral Award, Dr. Lisa Kinnard (PI), USAMRMC (DAMD17-03-1-0314) 07/03-06/05.
2. Tumor-targeted MR Contrast Enhancement by Anti-transferrin Receptor scFv-Immunoliposome Nanoparticles. Dr. Paul Wang is the principal investigator of this pilot project; Dr. Nancy Davidson(PI) (NIH SPORE, P50 CA88843-04), 06/04-05/05
3. F19 NMR Detection of Trifluoperazine Crossing Blood-Brain-Barrier Through Pgp Modulation. Dr. Paul Wang (PI), Radiology Society of Northern America Research and Education Foundation Medical Student Departmental Grant (MSD0306), 06/03-08/03.
4. Tumor-targeted MR Contrast Enhancement Using Molecular Imaging Techniques. National Cancer Institute's Minority Institution/Cancer Center Partnership (MI/CCP) program Pilot Project Initiative, (NIH 5U54CA091431), 03/04-02/05.

5. A Partnership Training Program in Breast Cancer Research Using Molecular Imaging Techniques. This is a four year training grant partnership with the Johns Hopkins University, In vivo Cellulous and Molecular Imaging Center. The proposal is funded by the U.S. Army Medical Research and Materiel Command (W81XWH-05-1-0291), 07/05-06/09.

V.   CONCLUSIONS

This is a six year training program in breast cancer research using NMR imaging and spectroscopy techniques. This program is a multidisciplinary consortium of five departments including College of Medicine MD/PhD program, Radiology, Radiation Oncology, Biology and Electrical Engineering. This program has supported seven predoctoral students and five postdoctoral students. All the trainees have been actively involved in one of the seven ongoing research projects conducted in the Biomedical NMR Laboratory. They have learned the theory and instrumentation of NMR. Besides participating in the specific research project, the trainees also have attended the weekly seminars in the Cancer Center and special NMR seminar series in the Department of Radiology. The trainees have received a broad training in breast cancer and tumor biology. Based on the trainees' research, eight papers have been published and 16 abstracts have been presented in the national and international meetings. In addition, five grants including a USAMRMC postdoctoral award have received. This program has accomplished its goal to provide an educational and research opportunity to promising young African-American students to become productive breast cancer researchers.

VI.   ABBREVIATIONS

AD   Alzheimer's disease
APP   amyloid precursor protein
BBB   blood-brain-barrier
CADx   computer-aided diagnostic
dtg   double transgenic
HUH   Howard University Hospital
MCF7
MCF7/WT
MR   magnetic resonance
MRI   magnetic resonance imaging
MRS   magnetic resonance spectroscopy
NMR   nuclear magnetic resonance
OI   optical imaging
PET   positron emission tomography
Pgp   P-glycoprotein
PS-1   presenilin-1
TFP   trifluoperazine
TfRsc   transferrin single chain antibody
TfRscFv   transferrin single chain antibody variable fragment
TfRscFv-Lip-GAD-d transferrin single chain antibody variable fragment – lipid-gadolinium

VII. APPENDICES (Reprints)

1. Kinnard L, Lo S-C.B, Wang P, Freedman MT, Chouikha M, Separation of Malignant and Benign Masses in Mammography using Maximum-Likelihood Modeling and Neural Networks. Proc. of SPEI Vol 4684: 733-741, 2002.
2. Lo S-C.B, Li H, Wang Y, Kinnard L, Freedman M, A Multiple Circular Path Convolution Neural Network System for Detection of Mammographic Masses, IEEE Transactions on Medical Imaging, Vol 21, No 2 pp 150-158. 2002
3. Kinnard L, Lo S-C B, Wang PC, Freedman MT, Chouikha M, Automatic Segmentation of Mammographic Masses Using Fuzzy Shadow and Maximum-likelihood Analysis, Proc of IEEE Symposium on Biomedical Imaging (Cat 02EX608C): pp. 241-244, 2002.
4. Kinnard L, Lo S-C.B, Wang PC, Freedman MT, Chouikha M, Separation of Malignant and Benign Masses Using Image and Segmentation Features. Proc. of SPIE, 2003
5. Kinnard L, Lo SB, Makariou E, Osicka T, Wang PC, Freeman M, Chouikha M. Likelihood Function Analysis For Segmentation of Mammographic Masses For Various Margin Groups. Proc of IEEE Symposium on Biomedical Imaging. pp 113-116, 2004.
6. Liang XJ, Yin JJ, Zhou JW, Wang PC, Taylor B, Cardarelli C, Kozar M, Forte R, Aszalos A, Gottesman M. Changes in Biophysical Parameters of Plasma Membranes Influence Cisplatin Resistance of Sensitive and Resistant Epidermal Carcinoma Cells. Exp Cell Research 293:283-291, 2004.
7. Kinnard L, Lo SB, Makariou E, Osicka T, Wang P, Chouikha MF, Freedman MT. Steepest changes of a probability-based cost function for delineation of mammographic masses: A validation study. Med. Phys. 31(10):2796-2810, 2004.
8. Pirollo K, Dagata J, Wang PC, Freedman M, Vladar A, Fricke S, Ileva L, Zhou Q, Chang EH. A Tumor-Targeted Nanodelivery System to Improve Early MRI Detection of Cancer. J Mol Imaging 5(1):41-52, 2006.

Separation of Malignant and Benign Masses using Maximum-Likelihood Modeling and Neural Networks

Lisa Kinnard[a,b], Shih-Chung B. Lo[a], Paul Wang[c], Matthew Freedman[a], Mohamed Chouikha[b]

[a]ISIS Center, Department of Radiology, Georgetown University Medical Center, Washington, D.C.
[b]Department of Electrical Engineering, Howard University, Washington, D.C., USA
[c]Biomedical NMR Laboratory, Department of Radiology, Howard University, Washington, D.C.

ABSTRACT

This study attempted to accurately segment the masses and distinguish malignant from benign tumors. The masses were segmented using a technique that combines pixel aggregation with likelihood analysis. We found that the segmentation method can delineate the tumor body as well as tumor peripheral regions covering typical mass boundaries and some spiculation patterns. We have developed a multiple circular path convolution neural network (MCPCNN) to analyze a set of mass intensity, shape, andtexture features for determination of the tumors as malignant or benign. The features were also fed into a conventional neural network for comparison. We also used values obtained from the maximum likelihood values as inputs into a conventional backpropagation neural network. We have tested these methods on 51 mammograms using a grouped Jackknife experiment incorporated with the ROC method. Tumor sizes ranged from 6mm to 3cm. The conventional neural network whose inputs were image features achieved an A_z value of 0.66. However the MCPCNN achieved an A_z value of 0.71. The conventional neural network whose inputs were maximum likelihood values achieved an A_z value of 0.84. In addition, the maximum likelihood segmentation method can identify the mass body and boundary regions, which is essential to the analysis of mammographic masses.

Keywords: Computer-assisted diagnosis, breast cancer, convolution neural networks, feature extraction

1. INTRODUCTION

While many breast cancer diagnostic systems have been developed, fully-automated mass segmentation continues to be a major challenge in this area. Several investigators exploited methods using intensity values to decide if a pixel should be placed in the region of interest (ROI) or background [14,9,5,7]. Petrick[12] et al. developed the density weighted contrast enhancement (DWCE) method which applies a series of filters to the image in an attempt to extract masses. Li[6] et al. developed a competetitive classification strategy, which uses a combined soft and hard classification method for deciding if segmented regions are true or false positives. Li[7] et al. developed a segmentation method that uses probability to determine segmentation contours. Most of these methods are successful at segmenting the tumor body, however, they sometimes do not properly obtain the extended boundaries of the tumor. While conventional region-growing is an excellent pixel-based segmentation method, it may not suitable to use this method alone. It produces many segmentation contours for one tumor image,

---

Further author information: (Send correspondence to Lisa M. Kinnard)
Lisa M. Kinnard: E-mail: kinnard@isis.imac.georgetown.edu, Telephone: 1 202 687 5135
S.C. Ben Lo: E-mail: lo@isis.imac.georgetown.edu, Telephone: 1 202 687 1659,
Address: ISIS, Georgetown University, 2115 Wisconsin Avenue, NW, Washington DC, USA

but does not decide which segmentation contour is the best. Based on the above reasons, we have developed a tumor segmentation method that combines region-growing with probability assessment to determine final segmentation contours for various breast tumor images.

The most recognized obstacles in breast cancer diagnosis are (1) difficulties of diagnostic decision making in calling back patient for further breast examination, (2) the large number of suspected lesions of which only part of them are malignant lesions; and (3) missed diagnosis of breast cancer. The callback rates vary from 5% to 20% in today's breast cancer screening programs[1,16]. At some medical centers, the positive predictive rate can be 30% to 35%[4,1]while at others this rate can be as low as 10% to 15%. It is well known that effective treatment of breast cancer calls for early detection of cancerous lesions (e.g., clustered microcalcifications and masses associated with malignant cellular processes)[16,11,15] Tumors can be missed because they are obscured by glandular tissue and it is therefore difficult to observe their boundaries. We were motivated by this clinical obstacle and have developed a computer-assisted diagnostic system attempted to tackle this issue as demonstrated in the following sections.

2. METHODS

Computer-assisted breast cancer diagnosis is divided into three parts, namely, image segmentation, feature calculation, and classification. The next several section will theoretically describe the methods used in the study.

2.1. Segmentation

It is well known that lesion segmentation is one of the most important aspects of computer-assisted diagnosis (CAD_x) because one of the main characteristics of malignant tumors is ill-defined, and/or spiculated borders. Conversely, benign tumors typically have well-defined, rounded borders. Segmentation is therefore extremely important because the diagnosis of a tumor can strongly depend upon image features.

Pixel aggregation is an automated segmentation method in which the region of interest begins as a single pixel and grows based on surrounding pixels with similar properties, e.g., grayscale level or texture.[2] It is a commonly used method[13,14,9]due to its simplicity and accuracy. The computer will use the maximum intensity as the "seed point" -a pixel that is similar to the suspected lesion and is located somewhere inside the suspected lesion. The next 4- or 8-neighboring pixel is checked for similarity so that the region can grow. If pixels in the 4- or 8-neighboring region are similar, they are added to the region. The region continues to grow until there are no remaining similar pixels that are 4- or 8-neighbors of those in the grown region.

Our implementation of this method checks the 4-neighbors of the seed pixel and uses a graylevel threshold as the similarity criterion. If a 4-neighbor of a pixel has an intensity value greater than or equal to a set threshold, it is included in the region of interest. The 4-neighbors were checked instead of the 8-neighbors so that surrounding tissue will not be included. The intensity threshold was used as a similarity criterion due to its simplicity and effectiveness.

By using the same seed point with multiple intensity threshold values we obtained between 150 and 300 of gray level change per lesion; however, the computer did not have the ability to choose the best partition. We added a maximum-likelihood component to the region-growing algorithm. The algorithm can be summarized in five steps. The image was first multiplied by a 2D shadow, whose size was approximately the same size as the ROI. We will henceforth refer to the image to which the 2D shadow has been applied as the "fuzzified" image. We started the threshold value at the maximum intensity in the image and decreased the intensities in successive steps. Consequently, we obtained a sequence of growing contours (S_i), where intensity value was the similarity criterion. There was an inverse relationship between intensity value and contour size, i.e., the lower the intensity value, the larger the contour. Next, we calculated the composite probability (P_i) for each contour (S_i):

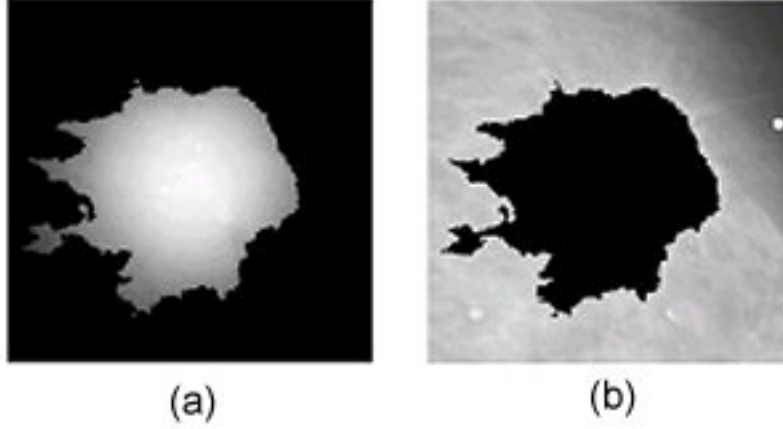$$P_i = p(S_i|pdf_i) \times p(outside S_i|ROI). \tag{1}$$

Figure 1: Figure (a) is used to calculate $p(S_i|pdf_i)$. Figure (b) is used to calculate $p(outsideS_i|ROI)$

where $p(S_i|pdf_i)$ is the probability density function (pdf) of the ROI subject to the fuzzified image (see Fig. 1). This pdf is calculated *inside* the contour, S_i, where i is the thresholding step. The quantity $p(outsideS_i|ROI)$ is the pdf of the ROI subject to the original image. This pdf is calculated *outside* the contour, S_i. Next we find the logarithm of the composite probability, P_i in the following way:

$$log(P_i) = log(p(S_i|pdf_i)) + log(p(outsideS_i|ROI)),\qquad(2)$$

Finally, we determine the likelihood that the contour represents the tumor body by assessing the maximum likelihood function:

$$argmax(Log(P_i)),\qquad(3)$$

Equation 3 intends to find the maximum value of the aforementioned likelihood values as a function of intensity threshold. We assess (so as other investigators[5]) that the intensity value corresponding to this maximum likelihood value is the optimal intensity for the tumor body contour. We also determine the likelihood that the contour represents the tumor extended borders by assessing the maximum change of the likelihood function:

$$argmax\left(\frac{dLog(P_i)}{di}\right),\qquad(4)$$

i.e., find the steepest jump on the aforementioned function. An intensity value between this jump and the maximum value on the function produces the best contour of the tumor body and its extended borders.

2.2. Feature Calculation

One extremely important task in the separation of malignant and benign tumors is feature selection and calculation. Benign tumors can be lucent at the center and can have well-defined borders; while malignant tumors can have spiculated and/or fuzzy borders. We used the following features:

Global Features

$$Skewness = \frac{1}{N}\frac{\sum_{i,j=0}^{N-1}[g(i,j)-\overline{g(i,j)}]^3}{\sqrt{\sum_{i,j=0}^{N-1}[g(i,j)-\overline{g(i,j)}]^3}}\qquad(5)$$

where $g(i,j)$ is intensity value and $\overline{g(i,j)}$ is average intensity value.

$$Kurtosis = \frac{1}{N} \frac{\sum_{i,j=0}^{N-1}[g(i,j) - \overline{g(i,j)}]^4}{\sqrt{\sum_{i,j=0}^{N-1}[g(i,j) - \overline{g(i,j)}]^4}} \qquad (6)$$

$$Circularity = \frac{A_1}{A}, \qquad (7)$$

where A is the area of the actual ROI; A_1 is the area of the overlapped region of A and the effective circle A_c, which is defined as the circle whose area is equal to A and is centered at the corresponding centroid of A.

$$Compactness = \frac{p^2}{a}, \qquad (8)$$

where, p=tumor perimeter and a=tumor area

$$perimeter = tumor\ perimeter. \qquad (9)$$

Local Features

These intensity features were calculated on the 10° ROI as it was divided into 10° sectors in the polar coordinate system, therefore each tumor contained 36 sectors.

$$\overline{g(i,j)} = \frac{1}{N} \sum_{i,j=0}^{N-1} g(i,j), \qquad (10)$$

where Mean $= \overline{g(i,j)}$, N is the total pixel number inside the ROI

$$Contrast = \frac{P_f - P_b}{P_f}, \qquad (11)$$

where P_f is the average gray-level inside the ROI's and P_b is the average gray-level surrounding the ROI.

$$\sigma_f^2 = \frac{1}{N} \sum_{i=1}^{N} (g(i,j) - \overline{g(i,j)})^2, \qquad (12)$$

where σ_f^2 = standard deviation.

$$Area = tumor\ area \qquad (13)$$

$$\sigma_n = \frac{1}{N_b} \sum_{i=1}^{N_b} (r_i - \bar{r})^2, \qquad (14)$$

where σ_n = Deviation of the Normalized Radial Length, N_b is the total number of pixels located on the boundary of the ROI, r_i is the value of the normalized radial length from the boundary coordinate (x_i, y_i) to the centroid of the ROI; $\bar{r}$ is the mean of r_i.

$$Roughness = ([\frac{1}{N_b} \sum_{i=1}^{N_b} (r_i - \bar{r})^4]^{\frac{1}{4}} - [\frac{1}{N_b} \sum_{i=1}^{N_b} (r_i - \bar{r})^2]^{\frac{1}{2}})/\bar{r}. \qquad (15)$$

$$radial\ length = length\ of\ radius, \qquad (16)$$

where *length of radius* is the distance from the center of the tumor to its edge.

Given a second-order joint probability matrix $P_{d,\theta}(i,j)$, where $P_{d,\theta}(i,j)$ is the joint gray level distribution of a pixel pair (i,j) with the distance d and in the direction θ, six texture features are defined as follows:

$$E_{d,\theta}(i,j) = \sum_{i=1}^{L}\sum_{j=1}^{L} P_{d,\theta}(i,j)^2, \tag{17}$$

where $E_{d,\theta}(i,j)$ = energy.

$$I_{d,\theta}(i,j) = \sum_{i=1}^{L}\sum_{j=1}^{L} (i-j)^2 P_{d,\theta}(i,j), \tag{18}$$

where $I_{d,\theta}(i,j)$ = inertia.

$$E = \sum_{i=1}^{L}\sum_{j=1}^{L} P_{d,\theta}(i,j)log_2 P_{d,\theta}(i,j), \tag{19}$$

where E = entropy.

$$IDM_{d,\theta} = \sum_{i=1}^{L}\sum_{j=1}^{L} \frac{1}{1+(i-j)^2} P_{d,\theta}(i,j), \tag{20}$$

where, $IDM_{d,\theta}$ = Inverse Difference Moment.

$$DE_{d,\theta} = -\sum_{k=0}^{n-1} P_{x-y}(k)log_2 P_{x-y}(k), \; P_{x-y}(k) = \sum_{i=0}^{n-1}\sum_{j=0}^{n-1} P_{d,\theta}(i,j), \tag{21}$$

for $|i-j| = k, k = 0, 1, ..., n-1$ where, $DE_{d,\theta}$ = Difference Entropy.

2.3. Classifiers

We used a conventional backpropagation neural network for two of the three studies described in this paper. It is comprised of an input layer, one hidden layer, and one output. We used the multiple circular path neural network[8] for the third study described in this paper. It is comprised of 3 input layers, one hidden layer and one output. The first input layer is fully connected, i.e., all inputs connect to all hidden nodes. The second input layer is called a self correlation path, i.e., each node on the layer connects to a single set of the 18 image features for the fan-in and fully connects to the hidden nodes for fan-out. The third input layer is called a neighborhood correlation path, i.e., each node on the layer connects to the input nodes of adjacent sectors for the fan-in and fully connects to the hidden nodes for fan-out. Our study used 18 hidden layer nodes. A more detailed explanation of the MCPCNN can be found the work done by Lo et. al.[8].

3. EXPERIMENT

The image samples were chosen from several databases compiled by the ISIS Center of the Georgetown University (GU) Radiology Department and the University of Florida's Digital Database for Screening Mammography (DDSM).[3] They are a mixture of "obvious" cases and "not obvious" cases. The "obvious" cases contain tumors that are easily identifiable as malignant or benign while the "not obvious" cases are those that radiologists find difficult to observe and/or classify. Forty malignant and forty benign tumors were tested during this experiment. The GU films were digitized at a resolution of 100μm using a Lumiscan digitizer. The DDSM films were digitized at 43 and 50 μm's using both the Lumiscan and Howtek digitizers. We compensated for this difference in resolution by reducing the DDSM images to half their normal sizes. The images were of varying contrasts and the tumors were of varying sizes. There were 28 malignant cases and 23 benign cases.

Experiment	Features	Neural Network
1	Image Features	Conventional NN
2	Image Features	MCPCNN
3	ML-curve as features	Conventional NN

Table 1: This table summarizes the studies presented in this paper.

The experiment was subdivided into three studies as shown in table 1 below.

Experiments 1 and 2 used 6 global and 12x36 sector features to yield a total of 438 image features per tumor. There were 18 hidden nodes and 1 output for both the BP and MCPCNN classifiers. The training and testing method used was the jackknife method. Experiment 3 used 19 likelihood feature values per tumor. There were 15 hidden nodes and 1 output for the BP classifier. The training and testing method used was the jackknife method. The results were analyzed using the LABROC4 program.[10]

4. RESULTS

Here are two examples of segmentation results for both malignant (see Fig. 2) and benign (see Fig. 4) cases. Each example gives the segmentation result produced by the maximum likelihood value on the curves described in section 2.1.

The following is a table, which gives the A_z values produced by the neural network.

Experiment	Features	Neural Network	Az
1	Image Features	Conventional NN	0.66
2	Image Features	MCPCNN	0.71
3	ML-curve as features	Conventional NN	0.84

Table 2: Results from Experiments 1-3.

5. CONCLUSION AND DISCUSSION

In analyzing the segmentation results we drew several conclusions. We discovered that there was a marked difference between the likelihood functions in malignant cases and the likelihood functions in benign cases. The likelihood function in the benign case often experiences a sharp drop, while the likelihood function in the malignant case is often smoother. In the image, a sharp drop value in the likelihood function represents an abrupt change in the area as well as likelihood value. We observed thatin benign cases, the likelihood function sharp changes are much more evident because benign tumors usually have well-defined borders. Conversely, in many malignant cases, the likelihood functions are smoother because many of their the borders are ill-defined. In analyzing the likelihood functions for malignant cases we recognized that those curves with very sharp changes were produced from tumors with well-defined borders and vice versa; i.e., there were malignant tumors that could be mistaken as benign and vice versa.

The maximum likelihood curves used as inputs to the BP neural network produced the best performance overall. The image features used as inputs to the MCPCNN produced the second best performance. The image features used as inputs to the BP produced the worst performance. Since we received the best results by using the likelihood functions as features, we expect that the MCPCNN may improve the overall results by giving the likelihood functions in every sector.
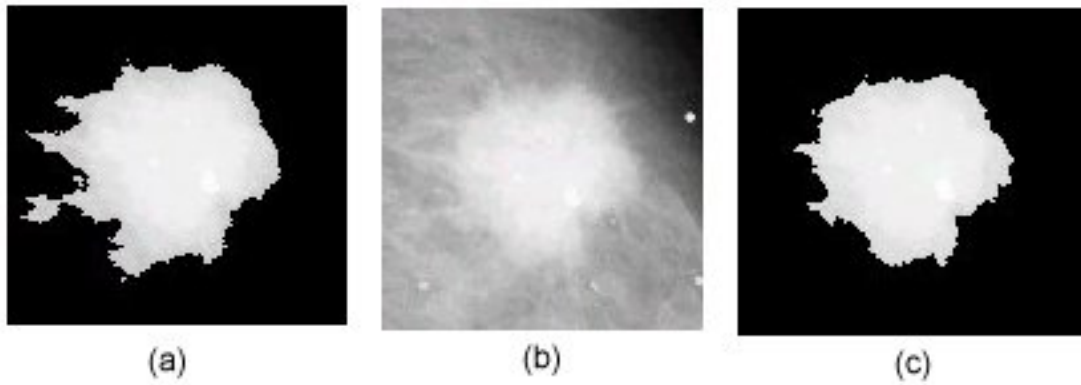
Figure 2. The segmentation results for a malignant tumor. Part (a) shows the segmentation result produced by the maximum likelihood change intensity choice, part (b) shows the original image, and part (c) shows the segmentation result produced by the maximum likelihood intensity choice.
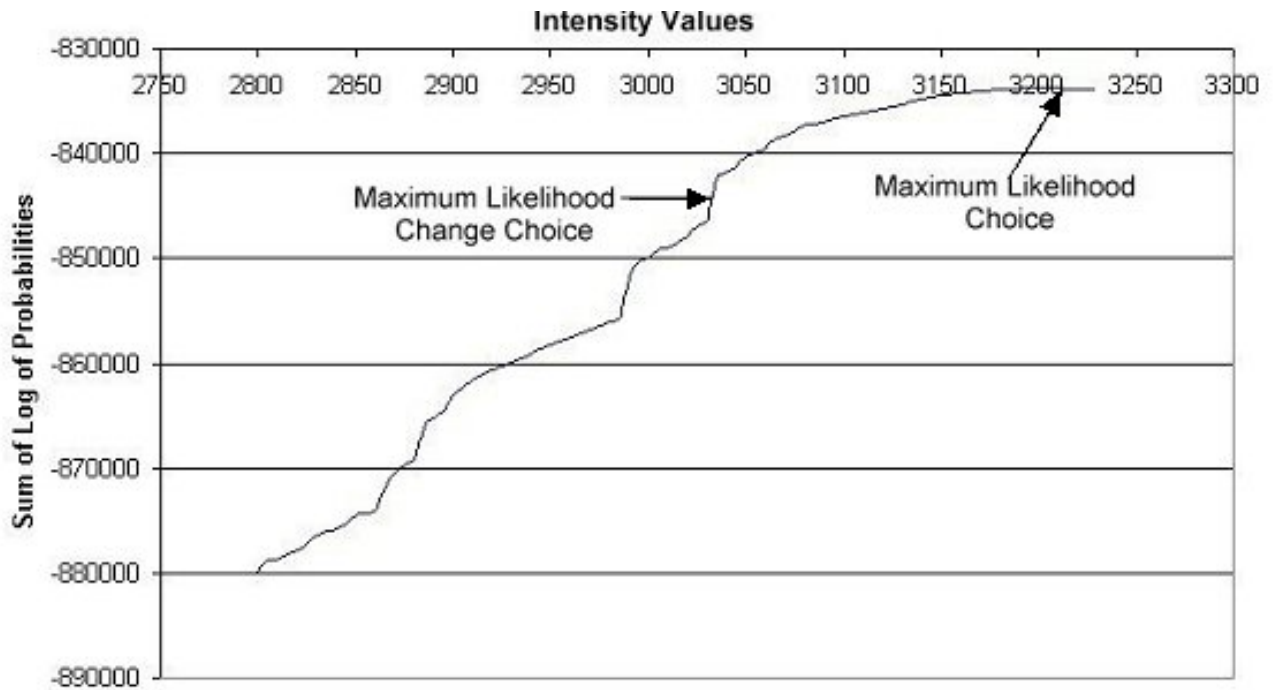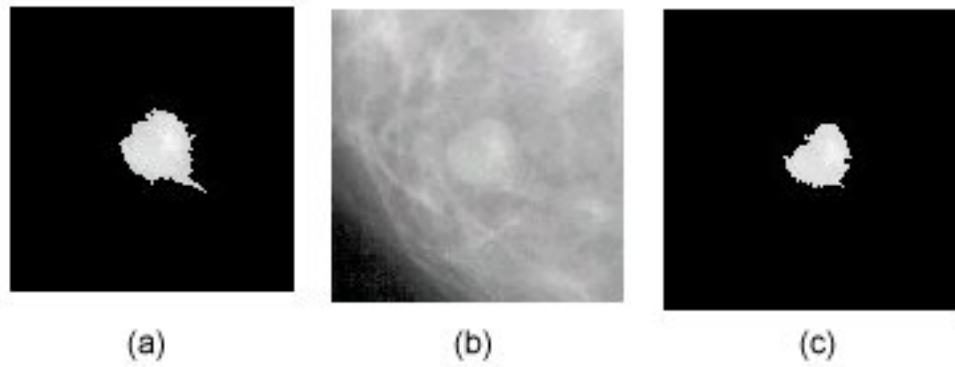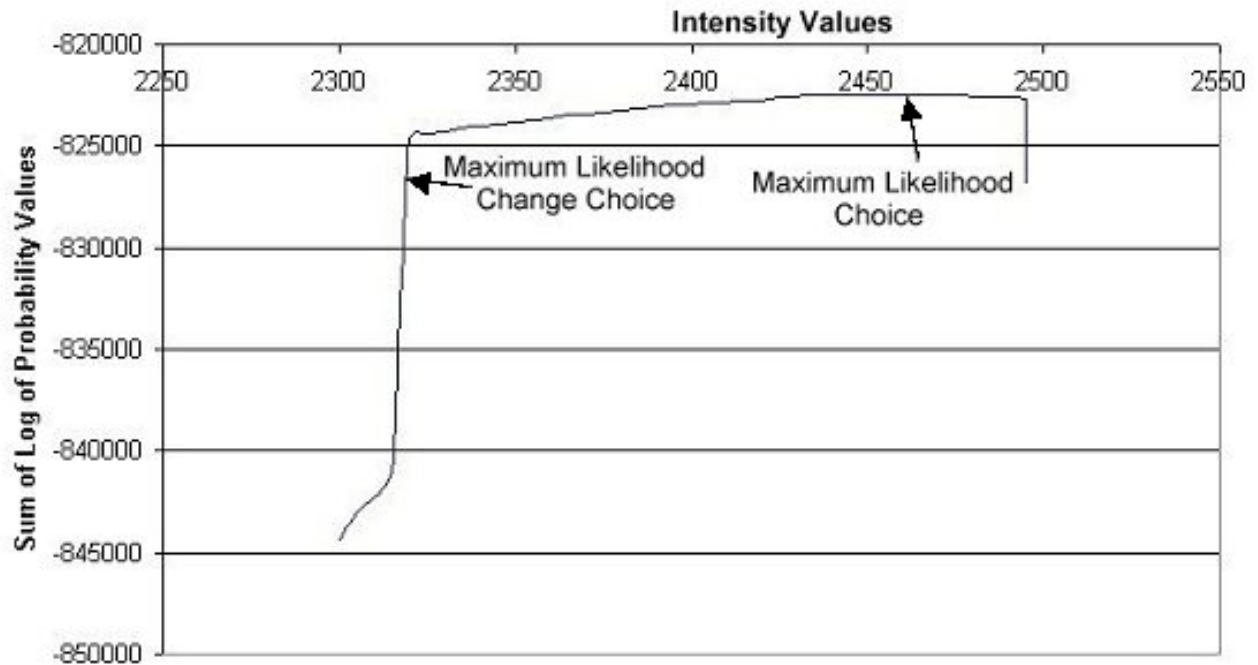

Figure 3. A likelihood function with respect to threshold values for all segmentation steps (malignant case) shown in Fig. 2.

ACKNOWLEDGMENTS

Figure 4. The segmentation results for a benign tumor. Part (a) shows the segmentation result produced by the maximum likelihood change intensity choice, part (b) shows the original image, and part (c) shows the segmentation result produced by the maximum likelihood intensity choice.

..

Figure 5. A likelihood function with respect to threshold values for all segmentation steps (benign case) shown in Fig. 4.

REFERENCES

1. Frankel SD, Sickel EA, Curpen BN, Sollito RA, Ominsky SH, Galvin HB, *Initial versus subsequent screening mammography: Comparison of findings and their prognostics significance.* AJR, 1995, vol. 164, pp. 1107-1109.
2. Gonzalez RC, Woods RE. Digital Image Processing Reading, MA: Addison Wesley, 1992.

3. Heath M, Bowyer KW, Kopans D et al, *Current status of the Digital Database for Screening Mammography*, Digital Mammography, Kluwer Academic Publishers, 1998, pp. 457-460.

4. Kopans DB. *The positive predictive value of mammography*, AJR, 1991, vol. 158, pp. 521-526.

5. Kupinski MA, Giger ML, *Automated Seeded Lesion Segmentation on Digital Mammograms*, IEEE Transactions on Medical Imaging, 1998, vol. 17, no. 4, pp. 510-517.

6. Li L, Zheng Y, Zhang L, Clark R, *False-positive reduction in CAD mass detection using a competitive classification strategy*, Medical Physics, 2001, Vol. 28, no. 2, pp. 250-258.

7. Li H, Wang Y, Liu KJR, Lo S-C, Freedman MT, *Computerized Radiographic Mass Detection - Part I: Lesion Site Selection by Morphological Enhancement and Contextual Segmentation*, IEEE Transactions on Medical Imaging, 2001, vol. 20, no. 4, pp. 289-301.

8. Lo SC, Li H, Wang J, Kinnard L, Freedman MT, *A Multiple Circular Path Convolution Neural Network System for Detection of Mammographic Masses*, IEEE Transactions on Medical Imaging, 2002, vol. 21, No. 2, (Accepted for publication).

9. Mendez AJ, Tahoces PG, Lado MJ, Souto M., Vidal JJ, *Computer-aided diagnosis: Automatic detection of malignant masses in digitzed mammograms*, Medical Physics, 1998, vol. 25, no. 6, pp. 957-964.

10. Metz C, LABROC Program, ftp://radiology.uchicago.edu/roc.

11. Nystrom L, Rutqvist LE, Wall S, Lindgren A, Lindqvist M, Ryden S, et. al., *Breast cancer screening with mammography: Overview of Swedish randomized trials*, Lancet, 1993, vol. 341, pp. 973-978.

12. Petrick N, Chan H-P, Sahiner B, Wei D, *An Adaptive Density-Weighted Contrast Enhancement Filter for Mammographic Breast Mass Detection*, IEEE Transactions on Medical Imaging, 1996, vol. 15, no. 1, pp. 59-67.

13. Pohlman S, Powell KA, Obuchowski NA, Chilcote WA, Grundfest-Broniatowski S, *Quantitative classification of breast tumors in digitized mammograms*, Medical Physics, 1996, vol. 23, no. 8, pp. 1336-1345.

14. Sahiner B, Chan HP, Wei D, Petrick N, Helvie MA, Adler DD, Goodsit MM, *Image feature selection by a genetic algorithm: Application to classification of mass and normal breast tissue*, Medical Physics, 1996, vol. 23, no. 10, pp. 1671-1684.

15. Shapiro S, *Screening: Assessment of current studies*, Cancer, 1994, vol. 74, pp.231-238.

16. Tabar L, Fagerberg G, Duffy S, Day NE, Gad A, Grontoft O. *Update of the Swedish two-country program of mammographic screening for breast cancer*, Radiology Clinics of North America: Breast Imaging - Current Status and Future Directions, 1992, vol. 30, pp. 187-210.

A Multiple Circular Path Convolution Neural Network System for Detection of Mammographic Masses

Shih-Chung B. Lo*, *Member, IEEE*, Huai Li, *Member, IEEE*, Yue Wang, *Member, IEEE*, Lisa Kinnard, and Matthew T. Freedman

Abstract—A multiple circular path convolution neural network (MCPCNN) architecture specifically designed for the analysis of tumor and tumor-like structures has been constructed. We first divided each suspected tumor area into sectors and computed the defined mass features for each sector independently. These sector features were used on the input layer and were coordinated by convolution kernels of different sizes that propagated signals to the second layer in the neural network system. The convolution kernels were trained, as required, by presenting the training cases to the neural network.

In this study, randomly selected mammograms were processed by a dual morphological enhancement technique. Radiodense areas were isolated and were delineated using a region growing algorithm. The boundary of each region of interest was then divided into 36 sectors using 36 equi-angular dividers radiated from the center of the region. A total of 144 Breast Imaging—Reporting and Data System-based features (i.e., four features per sector for 36 sectors) were computed as input values for the evaluation of this newly invented neural network system. The overall performance was 0.78–0.80 for the areas (A_z) under the receiver operating characteristic curves using the conventional feed-forward neural network in the detection of mammographic masses. The performance was markedly improved with A_z values ranging from 0.84 to 0.89 using the MCPCNN. This paper does not intend to claim the best mass detection system. Instead it reports a potentially better neural network structure for analyzing a set of the mass features defined by an investigator.

Index Terms—BI—RAD, computer-aided diagnosis, convolution neural network, mammography masses, neural network, sector features.

I. INTRODUCTION

IT IS KNOWN that effective treatment of breast cancer calls for early detection of cancerous lesions (e.g., clustered microcalcifications and masses associated with malignant cellular processes) [1]–[3]. Breast masses appear as areas of increased density on mammograms. It is particularly difficult for radiologists to detect and analyze a suspected area where a mass is overlapped with dense breast tissue. These masses are more readily seen as time progresses, but the further the tumor has progressed, the lower the possibility of a successful treatment. Therefore, increasing the chances of early breast cancer detection in improving today's clinical system is of vital importance in breast cancer diagnosis.

Several research groups have developed computer algorithms for automated detection of mammographic masses [4]–[8]. Some of these methods involved in classification of masses and normal dense breast tissues [7], [8]. Investigators also attempted to classify the malignant or benign nature of the detected tumors [9]–[11]. It is conceivable that correct segmentation of the masses [12] plays an important processing step prior to further mass analysis. In short, the results of these detection programs indicate that a high true-positive (TP) rate can be obtained at the expense of two or three false-positive (FP) detections per mammogram. Mammographically, a multiplicity (more than two) of similar benign-appearing breast lesions argues strongly for benignity [13]–[16] and, indeed, the more masses that are identified, the less chance that they represent cancer [17]. If the computer indicates multiple suspicious locations on a mammogram, the radiologist has to seek out one mass that possesses mammographic features, which are different from the others. The significant lesion may be missed due to the multiplicity of possible lesions. We, therefore, believe that a more useful and fundamental approach to computer-aided diagnosis (CAD) of masses is to devise computer programs to analyze features of a suspected area [18], [19] and to provide feature measures and estimates of the likelihood of malignancy by making comparisons within a digital mammographic database. The computer, therefore, serves as a second opinion and also provides a reproducible and an objective evaluation of the mass. With this aid, the radiologist may also increase his/her sensitivity by lowering the threshold of suspicion, while maintaining the overall specificity and reading efficiency.

II. CLINICAL BACKGROUND OF BREAST LESIONS AND TECHNICAL APPROACH IN MASS DETECTION

A. Description of Clinical Background

Most commonly, breast cancer presents itself as a mass. The same lesion shows a somewhat different picture from one projection to the other. Difficulties in masses also vary with the underlying breast parenchyma. In the fatty breast, masses are generally easy to detect. In the dense breast, mass detection is more difficult and auxiliary signs aid this detection. When the breast contains one mass, the decision process is based on its size, shape, and margins. When there are several masses, one looks at each, trying to determine whether any has features to suggest cancer. Furthermore, one looks to see if any mass is different in appearance from the others. Multiple small, well-defined, similar masses that present themselves bilaterally are all likely to be benign. Large, poorly defined, spiculated and unusually radiodense masses are extremely likely to be malignant. In this study, we used several computational features (see Section III-B) highly associated with four major features of breast masses routinely used in clinical reading:

Density: Malignant lesions tend to have greater radiographic density due to high attenuation and less compressibility of cancer than normal tissue. Radiolucent lesions are typically benign and the diagnosis can be made from the mammogram.

Size: If the lesion has morphological features suggesting malignancy, it should be considered suspicious regardless of the size. Isolated masses with noncystic densities greater than 8 mm in diameter can be malignant. In general, the larger a lesion, the more suspicious it is.

Shape: The more irregular the shape of a lesion, the more likely the possibility of malignancy. Lesions tend to be round, ovoid and/or lobulated. Small and frequent lobulations are suspicious. Lesions in the lateral aspect of the breast near the edge of the parenchyma with a reniform shape and a hilar indentation or notch usually represent a benign intramammary lymph node. Breast carcinoma hidden in the dense tissues can cause parenchymal retraction, which possess different shapes.

Margins: The margins of the lesion should be carefully evaluated for areas of spiculation, stellate patterns or ill-defined regions. Most breast cancers have ill-defined margins secondary to tumor infiltration and associated fibrosis. The appearance of spiculations and a more diffuse stellate pattern are almost pathognomonic for cancer. Lesions with sharply defined margins have a high likelihood of being benign; however, up to 7% of malignant lesions can be well circumscribed.

These are known clinical features and have been adapted in "Breast Imaging—Reporting and Data System" (BI—RAD) [20] of the American College of Radiology. Fig. 1(a) and (b) shows two breast images containing masses. In Fig. 1(a), a malignant mass is superimposed on the dense glandular tissue.
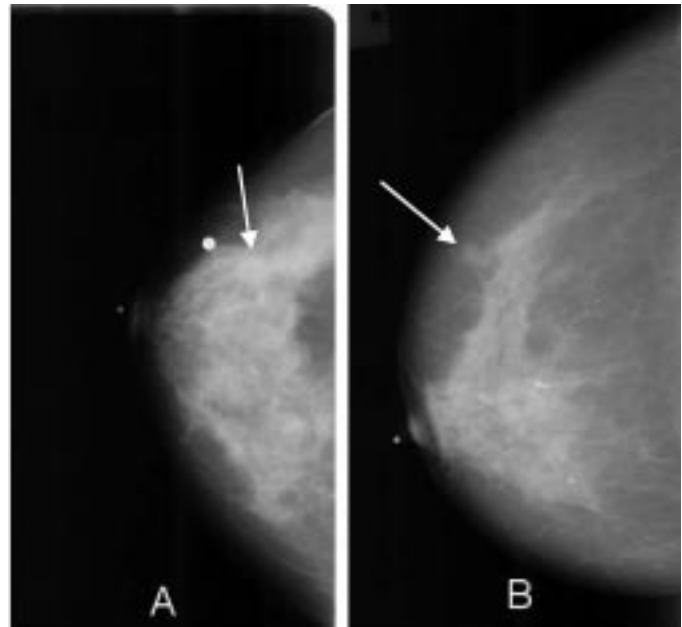

Fig. 1.   (a) Dense breast containing a malignant mass. (b) Fatty and glandular breast containing a malignant mass.

However, its spiculated nature makes it easily identifiable. In Fig. 1(b), another malignant mass is located on the fatty background but is associated with a large body of glandular tissue. This mass is not easily detectable by the computer because its density is lower than the neighboring glandular tissue. Furthermore, one end of the mass is fully connected with this tissue.

B. Technical Approach for Detection of Mammographic Masses

In this study, our goal was to detect clinically suspicious lesions. The differentiation of benign and malignant status of the mammographic masses can be extended from this study model and will be reported in our future work. The study was conducted with the following steps: 1) use background correction method and morphological operations to extract radio-opaque areas; 2) delineate the boundary of the areas; 3) compute the features and texture of the masses with emphasis on the boundary; and 4) design training strategy using neural networks as classifiers for the recognition of mass features. The overall detection scheme of the study framework is shown in Fig. 2.

III. DEVELOPMENT OF TECHNICAL METHODS

A. Preprocessing and Extraction of Suspicious Masses

In automatic mass detection, accurate selection of suspected masses is considered a critical first step due to the variability of normal breast tissue and the lower contrast and ill-defined margins of masses. In our previous study [18], we aimed to improve the task of lesion site selection using model-based image processing techniques for unsupervised lesion site selection. We focused on two essential issues in the stochastic model-based image segmentation: enhancement and model selection. Based on the differential geometric characteristics of masses against
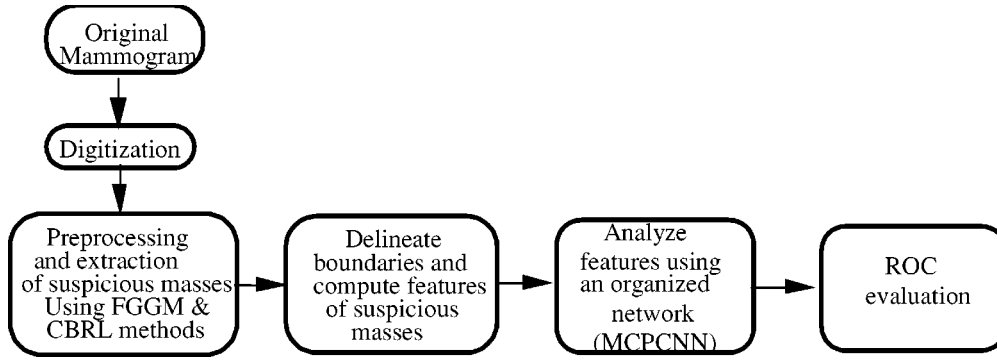
Fig. 2. A system flow chart for the detection of masses in this study.

the background tissues, we proposed one type of morphological operation to enhance the mass patterns on mammograms by removing high intensity background caused by breast tissues while maintaining mass-signals [18]. Then we employed a finite generalized Gaussian mixture (FGGM) distribution to model the histogram of the mammograms where the statistical properties of the pixel images are largely unknown and are to be incorporated. We incorporate the expectation-maximization algorithm with two information theoretic criteria to determine the optimal number of image regions and the kernel shape in the FGGM model. Finally, we applied a contextual Bayesian relaxation labeling (CBRL) technique to perform the selection of suspected masses.

We consistently processed the mammograms using this prescreening segmentation method. In the previous study [18], the FGGM method isolated 1142 potential masses including 114 of the 186 true masses in 200 mammograms. The mammograms were collected from the Mammographic Image Analysis Society (MIAS) database [21] and Brook Army Medical Center (BAMC) database. After morphological enhancement, 3143 potential masses were extracted using the FGGM technique. Of them, 181 were masses; however, five masses were not extracted. The results demonstrated that more true masses were picked up after enhancement although more false cases were also included. The undetected areas mainly occurred at the lower intensity side of the shaded objects or more obscured by fibroglandular tissues that, however, were extracted on morphological enhanced mammograms. Additionally, when the margins of masses are ill defined, only parts of suspicious masses were extracted from the original mammograms. We, therefore, decided to use the proposed morphological operation as a preprocessing step for the image enhancement prior to a segmentation method for the extraction of potential masses on the mammograms.

Based on the CBRL segmented region of interest (ROI), we employed a region growing method using a four-neighbors connection method assisted with a template masking operation to fill unconnected holes in the ROI

$$\text{IF } f(x-a, y-b) > V \text{ and } f(x, y) \in S,$$
$$\text{then } f(x-a, y-b) \in S \quad (1)$$
$$\text{IF } f(x-d, y-d) \in S, \text{ then } f(x-t, y-s) \in S$$
$$\text{for } t \leq d \text{ and } s \leq d \quad (2)$$

where V denotes the threshold value of the originally CBRL segmented ROI, S represents the set of growing region, and $[a, b]$ is a set of four conditions (i.e., $[1, 0]$, $[-1, 0]$, $[0, 1]$, and $[0, -1]$) for the four neighboring pixels. In (2), d is the size of template. In practice, we found that d should be set at five pixels to fill the holes without disrupting the boundary.

B. Feature Extraction of the Masses

Feature extraction methods play an essential role in many pattern recognition tasks. Once the features associated with an image pattern are extracted accurately, they can be used to distinguish one class of patterns from the others. Recently, many investigators have found that the multilayer perceptron (MLP) neural network using the error backpropagation training technique is a very powerful tool to serve as a classifier [22], [23]. In fact, the use of MLP neural network system for classification of disease patterns has been widely applied in the field of CAD [24]–[28].

The success of using a classifier for a pattern recognition task would rely on two factors: 1) selected features that could describe a discrepancy between image patterns and 2) accuracy of the feature computation. Should either one fail, no analyzer or classifier would be able to achieve an expected performance. By analyzing many clinical samples of various sizes of masses, we found that the peripheral portion of the mass plays an important role for mammographers to make a diagnosis. The mammographer usually evaluates the surrounding background of a radio-dense area when a region is suspected.

We used the CBRL segmented ROI to compute the center. Since the segmented ROIs were somewhat smaller than the mammographer's delineation and on the denser region of the suspected patch, the computed centers were quite close to the visual center. We then divided the boundary of the ROI into 36 sectors (i.e., 10° per sector) using 36 equi-angular dividers radiated from the center of the ROI. The following features were computed within each 10° sector of the region.

a) "l"—the length from the center of the ROI to the boundary segment of the sector.
b) "a"—the $\cos(\theta)$ (where θ is the normal angle of the boundary).
c) "g"—the average gradient of gray value on the segment along the radial direction (i.e., $g = \sum_{i=1}^{N} \{g_i/N\}$) where N is the number of pixels of i along the radial direction from $l/3$ inside the boundary to the boundary (see the left
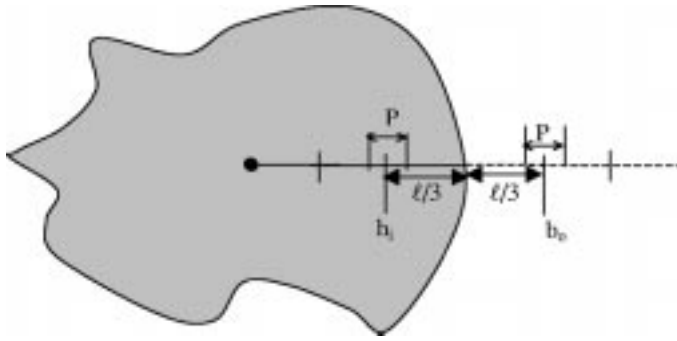
Fig. 3. A suspicious mass is delineated and shown as the shaded region. Contrast is computed by subtracting the average background pixel value (i.e., b_o, $o = 1, 2, \ldots P$) from the average foreground value (i.e., h_i, $i = 1, 2, \ldots P$).

$l/3$ line segment, Fig. 3). Technically speaking, this set of gradient values may also serve as a fuzzy system on the input layer in the neural network (to be described in Section III-C).

d) "c"—the gray value difference (i.e., contrast) along the radial direction. Specifically, $c = \sum_{i=1}^{P} \{h_i/P\} - \sum_{o=1}^{P} \{b_o/P\}$ where h_i (or b_o) represents a pixel value along the radial direction. The position $l/3$ inside the boundary is the center of pixels h_i ($i = 1, 2, 3, \ldots P$) and position $l/3$ outside the boundary is the center of pixels b_o ($o = 1, 2, 3, \ldots P$), and P is the number of pixels equivalent to a segment of $l/6$ and was used for averaging (see Fig. 3).

Hence, a total of 144 computed features (four features/sector for 36 sectors) were used as input values for the classification of the ROI. The relationship between the computed features and BI—RADS descriptors are discussed below.

i) ROI Size—The size of ROI is provided by the 36 "l" values.

ii) ROI Shape (round, oval, lobulated, or irregular)—The 36 "l" and 36 "a" values can describe the shape of the ROI.

iii) ROI Margin (circumscribed, microlobulated, obscured, ill- defined, or spiculate)—The 36 "g" and 36 "l" values can describe the ROI margin.

iv) ROI Density (fat-containing, low density, isodense, or highly dense)—The 36 "c" and 36 "g" values can be used to describe the density distribution of the ROI.

In short, the selected features are greatly associated with the main mass descriptors indicated in the BI—RADS. The reason for using 36 values for each nominated feature is four-fold: 1) mass boundary varies, it is difficult to describe an image pattern using a single value; 2) due to the general shape of the masses, the features of masses can be easily analyzed by the polar coordinate system; 3) in case some features are inaccurately computed in several directions due to the structure noises, such as the breast slender lines, there may still exist a sufficient number of correct features; and 4) generally more accurate results can be produced by using subdivided parameters rather than using global parameters in a pattern recognition task when the parameters are barely discernable and sample sizes are sufficiently large. Other computational features (e.g., difference

entropy [19] and other higher order features) are eligible but require further investigation.

C. The Neural Network Structure Specifically Designed for the Extracted Boundary Features

1) Multiple Paths With Circular Networking to Instruct the Neural Network in Analyzing Sector Features: This paper focuses on neural network design and arrangement of features for effective pattern recognition of ROIs. We designed several neural network connections between the input and the first hidden layers as shown in Fig. 4. In this neural network system, the first layer also functions as a correlation layer that transforms and encodes the signals from input nodes into correlation features for further neural network process. Fig. 4(a)–(c) illustrates the full connection (FC), a self correlation (SC) network, and a neighborhood correlation (NC) network, respectively. Network connections with multiple sectors (i.e., 20°, 30°, 40°, and 50° of the NC) are grouped separately as independent NC paths. In the following study, we used four SC paths for a single sector and thirteen NC paths for four types of multisectors. The method of using the multiple correlation connections was motivated by our research experience in two-dimensional (2-D) convolution neural network (CNN) [(2-D CNN)] where we found that more than ten multiple convolution kernels in the CNN were necessary in the detection of lung nodules and microcalcifications [25].

Compared with 2-D CNN systems, the computation required in the one-dimensional (1-D) CNN (e.g., 144 input features) is relatively small. The combination of the networking paths described earlier for multiple circular path convolution neural network (MCPCNN) was implemented using C programming language. The internal computation algorithm used in the MCPCNN shares the same convolution process as that in the 2-D CNN [25]. Rotation invariance and flip invariance for training the 1-D convolution kernels in the MCPCNN were employed.

The fully connected neural network is a conventional feedforward MLP neural network. The signals of the fully connected neural network join the other network processes (i.e., SC paths and NC paths) at the single node of the output layer. The signal received at the output node is scaled between zero and one. During the training, zero and one were assigned at the output node to perform backpropagation computation for a nonmass and a mass, respectively. The backpropagation is computed in such a way that the computed incremental errors [see equations (9) and (10)] are retraced into every independent network path. Excluding the output layer, the SC and NC signals are independently arranged and are processed through the 1-D convolution process in the forward propagation. The learning algorithms for all three types of circular network paths are based on the backpropagation training method.

Let $V^0(n', s')$ represents an input signal at the node n' and sector s'. The signal processed through an NC path and to be received at each node, n, on the first hidden layer is

$$N^1_{j[NC]}(n)$$

$$= \left[\sum_{s'} \sum_{n'} V^0(n', s') \cdot W_{j[NC]}(n', s'; n) \right] + b^0_{j[NC]}(n) \quad (3)$$
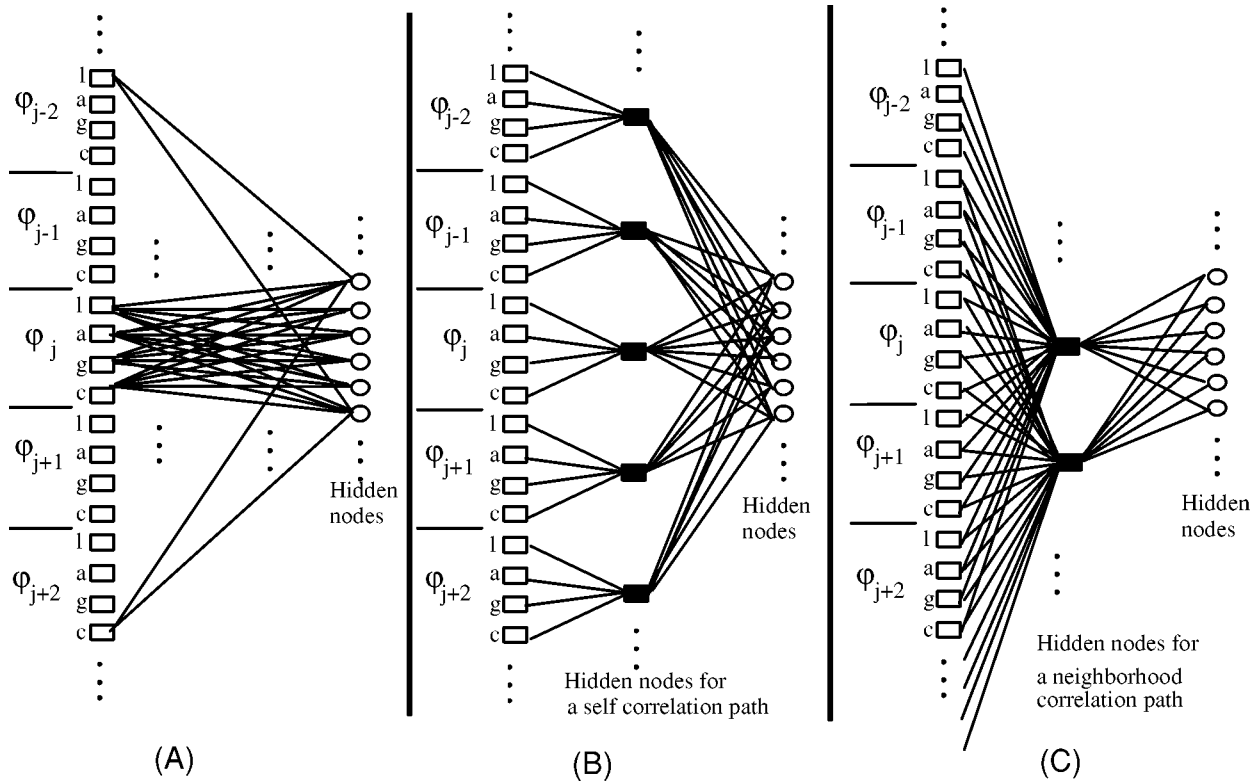
Fig. 4. Three types of network paths connecting the input and the hidden layers in the MCPCNN. (a) FC path. (b) SC path. Eeach node on the layer connects to a single set of the features (l, a, g, c) for the fan-in and fully connects to the hidden nodes for fan-out. (c) A NC path. Each node on the layer connects to the input nodes of adjacent sectors for the fan-in and fully connects to the hidden nodes for fan-out. The fan-in nets emphasizing SC in (b) and NC in (c) represent convolution weights (i.e., the same type of sectors possess the same set of weighting factors).

where $b^0_{j[NC]}(n)$ represents the bias term and $W_{j[NC]}(n', s'; n)$ is an array associated the 2-D nets that fan-in to a given receiving node, n. Each element of $W_{j[NC]}(n', s'; n)$ is the weight factor connected to node n from node n' sector s' through a NC path, j, and s' covers a range of neighborhood sectors corresponding to each type of NC path. Note that multiplications between the input nodes and connecting weights are computed first followed by taking the sum of the products for those nodes and sectors involved. The operation is repeated by shifting the weights from one set of sectors to the next. The procedure involving array multiplication passing through every sector is referred as the 1-D convolution operation that takes place in the sector dimension. The signal processed through an SC path and to be received at a node, n, on the first hidden layer is a special case of an NC path when s' only covers one sector

$$N^1_{i[SC]}(n) = \left[\sum_{n'} V^0(n', s') \cdot W_{i[SC]}(n'; n) \right] + b^0_{i[SC]}(n)$$

$$(4)$$

where $W_{i[SC]}(n'; n)$ is the weight factor connected to n from node n' through a SC path, i, regardless of the sectors. A total of 18 paths (1 FC, 4 SC paths, and 13 NC paths for four types of multisectors) were used in our experiment described later. Nevertheless, the signals processed through a path and to be received at each node, n, on the first hidden layer is

$$V^1_P(n) = S\left(N^1_P(n)\right) \qquad (5)$$

where p is one of the network paths and $S(z)$ is a sigmoid function given by

$$S(z) = \frac{1}{1 + \exp(-z)}. \qquad (6)$$

The sigmoid function would produce modulated values ranging from zero to one. The signals on other hidden layers in each path are processed the same as a conventional fully connected neural network. Other than the first hidden layer, the receiving signals at a hidden layer, l, collected from the previous hidden layer, l to one, are merged from the nodes in the last layer and are given by

$$V^l(n) = S\left(N^l(n)\right)$$
$$= S\left(\sum_{n'} V^{l-1}(n') \cdot W^{l-1}(n'; n) + b^{l-1}(n) \right) \quad (7)$$

where n' and n denote the nodes at layers $l - 1$ and l, respectively.

Let the tth change of the weight be $\Delta W^l_p(n', s'; n)$ and the tth change of the bias be $\Delta b^l(t)$. The error function is defined as

$$E = \frac{1}{2}(T - O)^2 \qquad (8)$$

where T and O denote the target output value and the actual output value, respectively when the input values $V^0(n', s')$, are
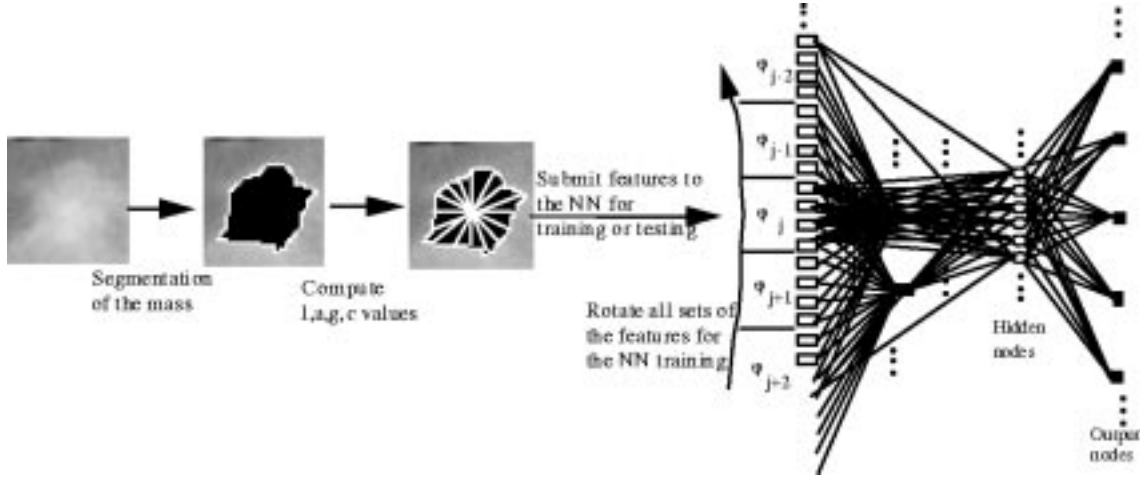
Fig. 5. A schematic diagram, showing the MCPCNN and sector features of masses, that was used in the following study.

entered in the network. In this model, the error backpropagation algorithm, which updates the kernel weights, is given below

$$\Delta W_p^l[t+1]$$
$$= \eta \left(\sum_n \sum_s \delta_p^{l+1}(n', s'; n, s) \cdot V_p^{l+1}(n, s) \right)$$
$$+ \alpha \Delta W_p^l[t] \tag{9}$$

$$\Delta b_p^l[t+1] = \eta \sum_n \sum_s \delta_p^{l+1}(n', s'; n, s) + \alpha \Delta b_p^l[t] \tag{10}$$

$$\delta_p^l(n', s'; n, s)$$
$$= S'\left(N_p^l(n', s')\right) \left(\sum_n \sum_s \delta_p^{l+1}(n, s) \cdot W_p^{l+1}(n, s) \right). \tag{11}$$

In the case of the last layer

$$\delta^L(n) = S'\left(N^L(n)\right)(T(n) - O(n)) \tag{12}$$

where $S'(z)$, η, α, and T denote the derivative of $S(z)$, the learning rate, the weighting factor contributed by the momentum term, and the desired output image, respectively. Furthermore, s or $s' = 1$ and $p = 1$ when $l \neq 0$.

During the training, we added an isotropic constraint to the weights of the 1-D convolution kernels so that

$$W_q^0(n, -s) = W_q^0(n, s) \tag{13}$$

where q is not the fully connected path. These additional constraints are used to induce the kernels functioning as correlation processing filters and could facilitate the algorithm in searching for an appropriate filter.

2) Resampling the Training Set Through Utilization of Rotation and Flip Invariance of the Features: In this neural network model, there are no starting and ending sectors. The forward and backpropagation computation can start from any sector. Considering a flipped patch, the characteristics of mass feature should remain the same. To take advantage of this flip invariance, the same numerical target value can be assigned at the output node

for the flipped image patch in order to double the amount of cases during training.

Since we designed a 10° increment for each rotation, every SC or NC path would process through 36 times using the defined features for each image patch. To simplify this network computation, we shifted one small sector (four nodes) on the input layer at a time to conduct the circular convolution process with the SC and NC kernels in the following experiments. By reversing the sequence of the sector, one can train the flipped version of the suspicious masses. Hence, using the properties of the rotation invariance and flip invariance for the neural network training literally increases the number of the training set by a factor of 72.

In summary, we have developed a complete detection procedure for the automatic recognition of mammographic masses including background adjustment, contrast enhancement, ROI segmentation, feature extraction, and MCPCNN system with a training method. Fig. 5 shows a flow diagram for the essential sections of the computational procedures.

IV. EXPERIMENTS AND RESULTS

As described in Section III-A, the 200 mammograms were selected from the MIAS database and the BAMC database for the study. Of the 200 mammograms, 50 mammograms are normal, and each of the 150 abnormal mammograms contains at least one mass case of varying size, subtlety, and location. Both the cranio-caudal (CC) and medio-lateral oblique (MLO) projection views were used. The films were digitized with a computer format of $2048 \times 2500 \times 12$ bits (for an $8'' \times 10''$ area where each image pixel represents $100 \, \mu$m square). Ninety-one mammograms, either a CC or an MLO view film, were selected from 91 patient film jackets. No two mammograms were selected from the same patient. All the digitized mammograms were miniaturized to $512 \times 625 \times 12$ bits using 4×4 pixel averaging before the method was applied. According to radiologists, the size of small masses is 3–15 mm in effective diameter. A 3-mm object in an original mammogram occupies 30 pixels in a digitized image with a $100–\mu$m resolution. After reducing the image size by four times, the object will occupy the range of about 7–8 pixels. The object with the size of seven pixels

is expected to be detectable by any computer algorithm. After preprocessing and an object screening based on the circularity test and the size test (between 3 and 30 mm), a total of 125 suspicious areas were selected from the testing mammograms (91 cases) for this study. Specifically, the screening procedure of reducing FPs involves two steps: 1) image patches with circularity less than 0.25 or diameter greater than 30 mm were eliminated and 2)) using probability modular neural network to rule out the majority of FPs. Of the 125 suspicious areas, 75 ROIs contained masses based on corresponding biopsy reports with one experienced radiologist reading. Of 75 masses, 39 were malignant and 36 were benign. This set of ROIs was used in [19] and discussed in [19, Fig. 6 and Table II].

A. Experiment 1

Of the 125 suspicious areas, we randomly selected 54 computer-segmented ROIs where 30 patches were matched with the radiologist's mass identification and 24 were not. This database was used to train two neural network systems: 1) a conventional three-layer neural network and 2) the proposed MCPCNN training method using the same neural network learning algorithm. The structure of the MCPCNN was described earlier. In the study, we used one fully connected path, four SC paths, four NC paths covering two sectors, four NC paths covering three sectors, three NC paths covering four sectors, and two NC paths covering five sectors in the first step network connection for the MCPCNN. All paths in the neural network have their hidden layers. Only one hidden layer per path was used. Both neural network systems were trained by the error backpropagation algorithm by feeding the features from the input layer and registering the corresponding target value at the output node. Completion of the training was determined by the mean square error [i.e., $\sum_{i=i}^{N}(T_i - O_i)^2/N$, where N is number of samples] when it was approximately reduced to 3×10^{-5}. Once the training of the neural networks was completed, we then used the remaining 71 computer segmented ROIs for the testing. Forty-five out of 71 ROIs were masses and 26 ROIs were not. Neither the images nor their corresponding patients in the testing set could be found in the training set. The neural network output values were fed into the LABROC4 program [29] for the performance evaluation. The results indicated that the areas (A_z) under the receiver operating characteristic (ROC) curves were 0.7869 ± 0.0536 and 0.8443 ± 0.0457 using the conventional neural network (MLP) and the MCPCNN, respectively. The ROC curves of these two neural network systems are shown in Fig. 6(a). The A_z value was 0.7869 ± 0.0536 when using the MLP method with 125 hidden nodes. The performance of the MLP remains about the same at 0.7809 ± 0.0551 of A_z using the same neural network parameters but with 30 hidden nodes.

We also invited another senior mammographer to conduct an observer study using the ROC study protocol. The mammographer was asked to rate each patch using a numerical scale ranging from zero to ten for its likelihood of being a breast mass. The image patches were displayed on a SUN monitor (Model: GDM-20D10). The image size shown on the monitor was reduced to approximately $7'' \times 9''$ as compared with the original film size ($8'' \times 10''$). These 71 numbers were also fed into the LABROC4 program. The A_z of the mammographer's perfor-
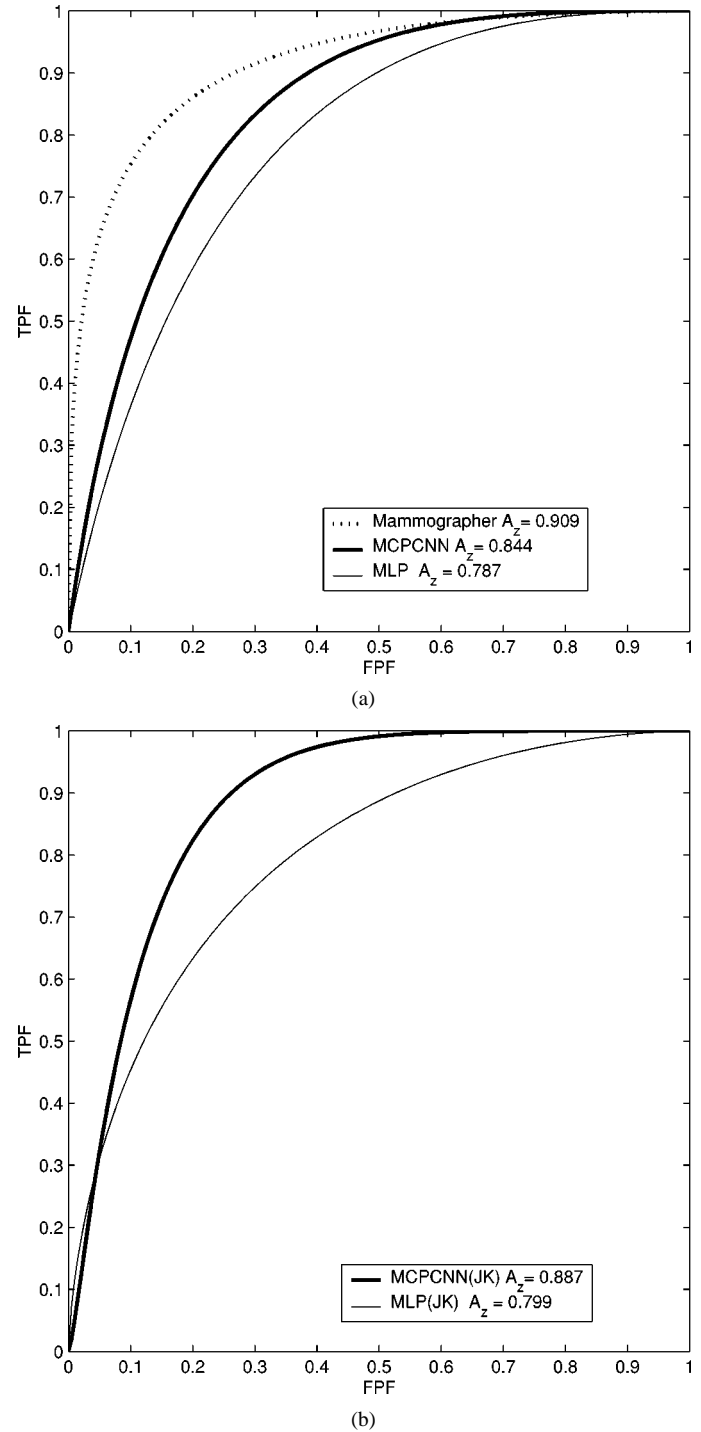

Fig. 6. The ROC curves obtained from corresponding experiments. (a) Shows that the performance of MCPCNN training method is superior to that of the conventional MLP method. The highest curve is the ROC performance of the senior mammographer. (b) Shows that the ROC results were increased using the leave-one-case-out procedure in both neural network systems. The MCPCNN still showed higher performance than conventional MLP method.

mance on this set of test cases was 0.909 ± 0.0340. The corresponding ROC curve is also shown in Fig. 6(a).

B. Experiment 2

We also conducted a leave-one-case-out experiment (i.e., jackknife procedure) using the same database. In this experiment, we used those image patches extracted from 90

TABLE I
ROC PERFORMANCE OF THE TEST METHODS IN DISTINGUISHING TRUE AND FALSE MASSES

	Comparative Analyses of Methods	A_z of Method (1)	A_z of Method (2)	P Values	Statistical Significance
Experiment 1	(1) Radiologist vs. (2) MCPCNN	0.909 ±0.0340	0.8443±0.0457	0.1855	No
	(1) Radiologist vs. (2) MLP	0.909 ±0.0340	0.7869 ±0.0536	0.0447	**Yes**
	(1) MCPCNN vs. (2) MLP	0.8443±0.0457	0.7869 ±0.0536	0.1344	No
Experiment 2	(1) MCPCNN vs. (2) MLP	0.8866 ±0.0289	0.7985 ±0.0394	0.0241	**Yes**

mammograms (one mammogram per case) for the training and used the image patches (most of them are single) extracted from the remaining one mammogram as test objects. The procedure was repeated 91 times to allow every ROI extracted from each mammogram to be tested in the experiment. For each individual ROI, the computed features were identical to those used in Experiment 1. Again, the training was stopped when the mean square error value approximately equal to 3×10^{-5}. Both neural network systems were independently trained and evaluated with the same procedure. The results indicated that the A_z values were 0.7985 ± 0.0394 and 0.8866 ± 0.0289 using the conventional neural network (MLP) and the MCPCNN, respectively. The performance of the MLP decreased to an A_z of 0.7608 ± 0.0429 using the same neural network parameters but with 30 hidden nodes. Fig. 6(b) shows the ROC curves of these two neural network systems using the leave-one-case-out procedure [30] in the experiment.

We also used CLABROC program [31] to analyze the ROC data and compare the ROC results. The results and their statistical significances using two tailed p value of 0.05 as the threshold are shown in Table I. The radiologist's performance is greater than conventional neural network system with a p value of 0.0447 in the first experiment. The MCPCNN was also proven to be superior to the MLP with a statistically significant result ($p = 0.0241$).

V. DISCUSSION

It is known in the field of artificial intelligence that the key factors in pattern recognition are: 1) effective methods in the extraction of features and 2) classification methods for the extracted features. In this study, we showed that the training method designed to guide the analyzer is also an important factor for a pattern recognition task. Though this finding is not new, the research of developing training methods for various pattern recognition tasks has not been established in the field of medical imaging. Our studies demonstrated that with proper network connections and task-oriented guidance, organized features would assist the neural network in performing the task.

Technically speaking, a feed-forward MLP neural network provides an integrated process for classification and sometimes for feature extraction. The output values of the hidden nodes can be interpreted as a reorganized set of features presented to the output layer for classification. The drawback of the MLP is, the user has a very little control and little understanding about the network learning. The MCPCNN is a network design that partially remedies these issues and is applicable for any pattern recognition task associated with ROIs. The MCPCNN (a member of the CNN family) possesses shared weights in the hidden layer(s) that act as filter kernels for extracting correlated features. With a higher resolution mammogram, a finer sector ($<10°$) would be preferred for the analysis mass, especially for the study of classification of masses. During forward and back-propagation training, the kernels would comply with both signals from input and output layers for all training cases, so as to maximize the classification performance. We do not recommend using 2D CNN for the detection of masses because the mass sizes vary from a few millimeters to 4 cm or even larger. It would require a large fixed size to cover the maximum mass size when using the 2-D CNN. The varieties of mass shapes and potential long spiculated patterns make the use of the 2-D CNN not practical. Since the MCPCNN processes the features computed from sectors, it does not limit the sizes of its ROIs. Best of all, the MCPCNN also has the ability to classify partially obscured masses. The 2-D CNN, however, would be more appropriate for the detection of microcalcifications and small lung nodules.

As far as the research in the detection of masses is concerned, we have shown that use of MCPCNN with sector features is an effective approach. Since the MCPCNN coordinates the input data and performs correlation between features of adjacent sectors in the first stage of data processing, the internal neural network learning algorithm can be changed if a learning algorithm is found to be more effective. In fact, the MCPCNN is a technique that can effectively classify features arranged in the polar coordinate system. A technique using the rubber band straightening transformation, independently developed by Sahnier *et al.* [11], for the detection of masses also employs a similar concept in extracting feature and/or texture in the polar coordinate system. We believe that integration of features and texture values computed at small sectors will be the research trend in mass detection and tumor classification.

VI. CONCLUSION

In the clinical course of detecting masses, mammographers usually evaluate the surrounding background of a radiodense area when an ROI is suspected. In this study, we simulated this fundamental concept with a neural network system (i.e., MCPCNN). In order for the MCPCNN to function, boundary features of the suspicious region in each radial sector were computed. We found that the MCPCNN is capable of analyzing correlated features within the sector and between adjacent sectors, which led to an improvement in detecting mammographic masses.

Through this study, we found that the selected features are somewhat effective in the detection of masses. These features

were "computationally translated" from the qualitative descriptors of BI—RAD. These features can be extended for the improvement of the mass detection, but this task is beyond the scope of this paper. With the preliminary studies shown above, we found the MCPCNN coupling with the proposed training method produced greater results than the conventional neural network. We found that the performances of both neural network systems were improved in Experiment 2. This may have occurred due to the number of training samples that was increased from 54 to 124. In Experiment 2, the A_z value was improved by 0.042 using the MCPCNN, which was higher than the A_z difference of 0.012 obtained by the conventional training method. The results implied that the MCPCNN learned more effectively than the conventional neural network when the number of training cases was increased. With the use of a larger database and advanced texture features proposed by others, it is expected that the performance of MCPCNN should be significantly improved. This paper does not intend to claim the best mass detection system, in comparison to similar systems; but rather its goal is to report a potentially better neural network structure for analyzing a set of mass features.

REFERENCES

[1] L. Nystrom, L. E. Rutqvist, S. Wall, A. Lindgren, M. Lindqvist, and S. Ryden *et al.*, "Breast cancer screening with mammography: Overview of Swedish randomized trials," *Lancet*, vol. 341, pp. 973–978, 1993.

[2] S. Shapiro, "Screening-assessment of current studies," *Cancer*, vol. 74, pp. 231–238, 1994.

[3] L. Tabar, G. Fagerberg, S. Duffy, N. E. Day, A. Gad, and O. Grontoft, "Update of the Swedish two-country program of mammographic screening for breast cancer," *Radiol. Clin. N. Amer.: Breast Imag.—Current Status Future Directions*, vol. 30, pp. 187–210, 1992.

[4] D. Brzakovic, X. M. Luo, and P. Brzakovic, "An approach to automated detection of tumors in mammograms," *IEEE Trans. Med. Imag.*, vol. 9, p. 233, Sept. 1990.

[5] R. Zwiggelaar, T. C. Parr, J. E. Schumm, I. W. Hutt, C. J. Taylor, S. M. Astley, and C. R. M. Boggis, "Model-based detection of spiculated lesions in mammograms," *Med. Image Anal.*, vol. 3, no. 1, pp. 39–62, 1999.

[6] N. Petrick, H. P. Chan, D. Wei, B. Sahiner, M. A. Helvie, and D. D. Adler, "Automated detection of breast masses on mammograms using adaptive contrast enhancement and texture classification," *Med. Phys.*, vol. 23, no. 10, pp. 1685–1696, 1996.

[7] B. Sahiner, H. P. Chan, N. Petrick, D. Wei, M. A. Helvie, D. D. Adler, and M. M. Goodsitt, "Classification of mass and normal breast tissues: A convolution neural network classifier with spatial domain and texture images," *IEEE Trans. Med. Imag.*, vol. 15, pp. 598–610, Oct. 1996.

[8] D. Wei, H. P. Chan, M. A. Helvie, B. Sahiner, N. Petrick, D. D. Adler, and M. M. Goodsitt, "Classification of mass and normal breast tissue on digital mammograms: Multiresolution texture analysis," *Med. Phys.*, vol. 25, no. 4, pp. 516–526, 1998.

[9] L. Hadjiiski, B. Sahiner, H. P. Chan, N. Petrick, and M. A. Helvie, "Classification of malignant and benign masses based on hybrid ART2LDA approach," *IEEE Trans. Med. Imag.*, vol. 18, pp. 1178–1187, Dec. 1999.

[10] H. Kobatake, M. Murakami, H. Takeo, and S. Nawano, "Computerized detection of malignant tumors on digital mammograms," *IEEE Trans. Med. Imag.*, vol. 18, pp. 369–378, May 1999.

[11] B. Sahiner, H. P. Chan, N. Petrick, M. A. Helvie, and M. M. Goodsitt, "Computerized characterization of masses on mammograms: The rubber band straightening transform and textures analysis," *Med. Phys.*, vol. 25, no. 4, pp. 516–526, 1998.

[12] M. A. Kupinski and M. L. Giger, "Automated seeded lesion segmentation on digital mammograms," *IEEE Trans. Med. Imag.*, vol. 17, pp. 510–517, Aug. 1998.

[13] D. D. Adler, "Breast Masses: Differential Diagnosis," in *ARRS Categorical Course Syllabus on Breast Imaging*, S. A. Feig, Ed. Reston, VA: Amer. Roent. Ray Soc., 1988, p. 31.

[14] M. J. Homer, "Imaging features and management of characteristically benign and probably benign breast lesions," *Radiol. Clin. N. Amer.*, vol. 25, p. 939, 1987.

[15] S. Pohlman, K. A. Powell, N. A. Obuchowski, W. A. Chilcote, and S. Grundfest-Broniatowski, "Quantitative classification of breast tumors in digitized mammograms," *Med. Phys.*, vol. 23, no. 8, pp. 1337–1345, 1996.

[16] M. Moskowitz, "Circumscribed lesions of the breast," in *Diagnostic Categorical Course in Breast Imaging*, M. Moskowitz, Ed. Oak Brook, IL: Radiol. Soc. N. Amer., 1986, p. 31.

[17] E. A. Sickles, "The rule of multiplicity and the developing density sign," in *ARRS Categorical Course Syllabus on Breast Imaging*, S. A. Feig, Ed. Reston, VA: Amer. Roent. Ray Soc., 1988, p. 177.

[18] H. Li, Y. Wang, K-J. R. Liu, S-C. B. Lo, and M. T. Freedman, "Computerized radiographic mass detection—Part I: Lesion site selection by morphological enhancement and contextual segmentation," *IEEE Trans. Med. Imag.*, pp. 289–301, Apr. 2001.

[19] ——, "Computerized radiographic mass detection—Part II: Decision support by featured database visualization and modular neural networks," *IEEE Trans. Med. Imag.*, pp. 302–313, Apr. 2001.

[20] *Breast Imaging—Reporting and Data System*. Reston, VA: Ame. Coll. Radiol., 1993.

[21] J. Suckling, J. Parker, D. Dance, S. Astley, I. Hutt, C. Boggis, I. Ricketts, E. Stamatakis, N. Cerneaz, S. Kok, P. Taylor, D. Betal, and J. Savage, "The mammographic images analysis society digital mammogram database," in *Exerpta Medica*, ser. Int. Congr., 1994, vol. 1069, (e-mail for inquiry: mias@sv1.smb.man.ac.uk.), pp. 375–378.

[22] S. Haykin, *Neural Networks: A Comprehensive Foundation*, 2nd ed. Englewood Cliffs, NJ: Prentice-Hall., 1999.

[23] D. E. Rumelhart, G. E. Hinton, and R. J. Williams, "Learning internal representation by error propagation," in *Parallel Distributed Processing: Explorations in the Microstructure of Cognition*, D. E. Rumelhart and J. L. McClelland, Eds. Cambridge, MA: M.I.T. Press, 1986, vol. 1, Foundation, ch. 8, pp. 318–362.

[24] S.-C. B. Lo, S. L. Lou, J. S. Lin, M. T. Freedman, M. V. Chien, and S. K. Mun, "Artificial convolution neural network techniques and applications to lung nodule detection," *IEEE Trans. Med. Imag.*, vol. 14, pp. 711–718, Dec. 1995.

[25] S.-C. B. Lo, H. P. Chan, J. S. Lin, H. Li, M. T. Freedman, and S. K. Mun, "Artificial convolution neural network for medical image pattern recognition," *Neural Networks*, vol. 8, no. 7/8, pp. 1201–1214, 1995.

[26] H. P. Chan, S.-C. B. Lo, B. Sahiner, K. L. Lam, and M. A. Helvie, "Computer-aided diagnosis of mammographic microcalcifications: Pattern recognition with an artificial neural network," *Med. Phys.*, vol. 24, no. 10, pp. 1555–1567, 1995.

[27] Y. Wu, K. Doi, M. L. Giger, and R. M. Nishikawa, "Computerized detection of clustered microcalcifications in digital mammograms: Applications of artificial neural networks," *Med. Phys.*, vol. 19, pp. 555–560, 1992.

[28] Y. Wu, M. T. Freedman, S.-C. B. Lo, R. A. Zuurbier, A. Hasegawa, and S. K. Mun, "Classification of microcalcifications in radiographs of pathological specimen for the diagnosis of breast cancer," *Acad. Radiol.*, vol. 2, pp. 199–204, 1995.

[29] C. E. Metz, B. A. Herman, and J. H. Shen, "Maximum likelihood estimation of receiver operating characteristic (ROC) curves from continuously-distributed data," *Statist. Med.*, vol. 17, pp. 1033–1053, 1998.

[30] K. Fukunaga and R. R. Hayes, "Effects of sample size in classifier design," *IEEE Trans. Pattern Anal. Machine Intell.*, pp. 873–885, Aug. 1989.

[31] C. E. Metz, P.-L. Wang, and H. B. Kronman, "A new approach for testing the significance of differences between ROC curves measured from correlated data," in *Information Processing in Medical Imaging*, F. Deconinck, Ed. The Hague, The Netherlands: Martinus Nijhoff, 1984, vol. PAMI-II, pp. 432–445.

AUTOMATIC SEGMENTATION OF MAMMOGRAPHIC MASSES USING FUZZY SHADOW AND MAXIMUM-LIKELIHOOD ANALYSIS

Lisa Kinnard[a,b,c], Shih-Chung B. Lo[a], Paul Wang[c], Matthew T. Freedman[a], Mohamed Chouikha[b]

[a]ISIS Center, Dept. of Radiology, Georgetown University Medical Center, Washington, D.C., USA
[b]Dept. of Electrical Engineering, Howard University, Washington, D.C., USA
[c]Biomedical NMR Laboratory, Department of Radiology, Howard University, Washington, D.C., USA

ABSTRACT

This study attempted to accurately segment tumors in mammograms. Although this task is considered to be a preprocessing step in a computer analysis program, it plays an important role for further analysis of breast lesions. The region of interest (ROI) was segmented using the pixel aggregation and region growing techniques combined with maximum likelihood analysis. A fast segmentation algorithm has been developed to facilitate the segmentation process. The algorithm repetitively sweeps the ROI horizontally and vertically to aggregate the pixels that have intensities higher than a threshold. The ROI is then fuzzified by the Gaussian envelope. With each segmented region for a given threshold step in the original ROI, the likelihood function is computed and is comprised of probability density functions inside and outside of the fuzzified ROI. We have implemented this method to test on 90 mammograms. We found the segmented region with the maximum likelihood corresponds to the body of tumor. However, the segmented region with the maximum change of likelihood corresponds to the tumor and it extended margin.

INTRODUCTION

The goal of breast mass segmentation is to separate suspected masses from surrounding tissue as effectively as possible. While it is a pre-processing step of Computer Assisted Diagnosis (CAD_x) it is extremely important in the diagnostic process, because a major characteristic used to separate malignant and benign tumors is shape [1, 12]. Over the years researchers have used many methods to segment masses in mammograms. Petrick [8] et al. used a filtering method called the Density Weighted Contrast Enhancement (DWCE) method. Karssemeijer and te Brake implemented a discrete dynamic contour model [1]. Li et al. developed a competetitive classification stragegy, which uses a combined soft and hard classification method for deciding if segmented regions are true or false positives. Furthermore, many researchers have implemented methods based on pixel aggregation [3, 5, 7, 9].

A major issue faced by CAD_x researchers is the ability to properly obtain the boundaries of masses because these boundaries are often obscured by surrounding breast tissue. While benign masses can be easily detected due to their well-defined boundaries, the borders of malignant tumors often blend into surrounding tissue, making it exceedingly difficult to properly segment them as effectively as possible. We have developed a maximum likelihood method [3] and have added a component to not only segment the tumor body, but to segment the extended tumor borders as well.

2. METHODS

The next several sections will describe the database, as well as provide the theoretical background used to develop our algorithm.

2.1. Database

The image samples were chosen from several databases compiled by the ISIS Center of the Georgetown University Radiology Department as well as the University of South Florida's (USF) Digital Database for Screening Mammography [2]. They are a mixture of "obvious" cases and "not obvious" cases. The "obvious" cases contain tumors that are easily identifiable as malignant or benign while the "not obvious" cases are those that radiologists find difficult to observe and/or classify. Forty malignant and forty benign tumors were tested during this experiment. The Georgetown University films were scanned at a resolution of 100μm while the USF films were scanned at 43.5 and 50 μm's. We compensated for this discrepancy in resolution by reducing the USF images to half their normal sizes. Hence, the original test images for this study all contain 12 bits per pixel with approximately 100 μm pixel size.

2.2. Pixel Aggregation and Region Growing

Pixel aggregation is an automated segmentation method in which the region of interest begins as a single pixel (seed point) and grows based on surrounding pixels with similar properties, e.g., grayscale level or texture [4, 11]. Typically, the seed is located at somewhere in the center region with the highest intensity in the suspected lesion. It is a commonly used method [7, 9, 10] due to its simplicity and accuracy. The next 4-neighboring pixel is checked for similarity so that the region can grow. Our algorithm checks the 4-neighbors of the seed pixel and its grown pixels uses a graylevel threshold. The threshold was used as a similarity criterion. The algorithm repetitively sweeps the ROI horizontally and vertically to aggregate the pixels that have intensities higher than a threshold. Sweeping the neighboring pixels in the alternate direction is a fast region aggregation algorithm that we have recently developed. The iteration ends when no more pixels are acquired in the sweeping step (see **Figure 1**). The segmented region can be grown by repeating the same method with a lower threshold value. Based on these segmented regions, we can evaluate the regions and region changes with respect to the threshold values. We do not recommend using the 8-neighbor connectivity method for it may

invade the surrounding tissue at the critical threshold to be discussed below.

At the conclusion of the each region segmentation in the sweeping process, there were several holes located inside the detected ROI. We used a chain code to detect the boundaries of these holes and then fill them using a threshold criterion. The output images of the above computer procedures are then used as templates (S_i) for the maximum likelihood analysis.

2.3. Fuzzy Shadow and Maximum Likelihood Analysis

By using the same seed point with multiple intensity threshold values, we obtained between 20 and 50 segmentation partitions per lesion. Kupinski and Giger proposed a maximum-likelihood based method to choose the best partition [3]. However, their method did not completely address the issue in identifying the tumor margin. Since the mammographic masses may or may not have their extended boundaries, it is important to separate the region of tumor body from its extended region. We adapt Kupinski and Giger's point in composing the ROI with a Gaussian envelope, which further fuzzies the tumor margin.

With each segmented region for a given threshold step in the original ROI, the likelihood function is computed so that it consists of probability density functions inside and outside of the fuzzified ROI.

The maximum likelihood method is based upon the probability density function (pdf), which for an image, is the histogram. Given a template S_i, which was described in section 2.1.1. we can model the image's pixel probabilities in the following way:

$$p\left(f(x,y)\middle|S_i,\sigma_l^2\right)=\begin{cases}His\left(f(x,y)\exp\left[-(x^2+y^2)/(2\sigma_i^2)\right]\right):(x,y)\in S_i\\His(f(x,y)):\qquad\qquad(x,y)\notin S_i\end{cases}\quad(1)$$

where Hist represents the histogram function. A Gaussian envelope with variance σ_l^2 centered at the seed point gray level was employed. The Gaussian envelope is a special case of the proposed fuzzy shadow. The size and standard deviation (σ_1) used in the experiment were 1400 and 160 pixels, respectively. These values were found experimentally, however, there are more statistical methods found in literature. Equation (2) defines the likelihood that a tumor is contained in the segmented region S_i:

$$p\left(I\middle|S_i,\sigma_l^2\right)=\prod_{(x,y\in L_i)}p\left(f(x,y)\middle|S_i,\sigma_l^2\right)\quad(2)$$

Equation (2) was implemented by summing the log of the probabilities of all pixel values inside S_i (segmented region) and outside S_i (background). Note that S_i is the segmented region based on the original ROI, not the fuzzified ROI. The likelihood for various partitions was then analyzed to obtain the final segmentation. The partition is chosen for the body of the tumor based on the following criterion:

$$p\left(I\middle|S_{body},\sigma_l^2\right)=\arg\max_i p\left(f(x,y)\middle|S_i,\sigma_l^2\right)\quad(3)$$

Based on our investigation, we further define that the step before maximum changes of likelihood value is the tumor margin:

$$p\left(I\middle|S_{m\arg in},\sigma_l^2\right)=\arg\max\left[\frac{d\ p\left(f(x,y)\middle|S_i,\sigma_i^2\right)}{d\ i}\right]\quad(4)$$

3. RESULTS

The following graphics are experimental results for one patient. **Figure 1** shows the a portion of the pixel aggregation process, **Figure 2**, is the plot produced by summing all probability values inside and outside L_i for various intensities, and **Figure 3** shows the original image followed by the tumor body image and the extended tumor body image.
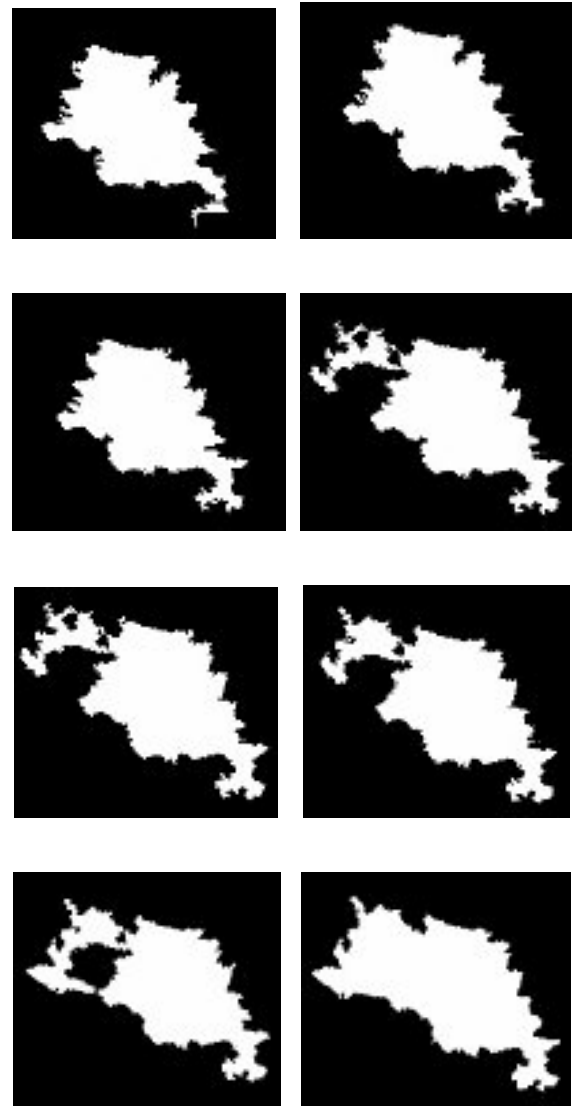

Figure 1 – Several iterations of the pixel aggregation process
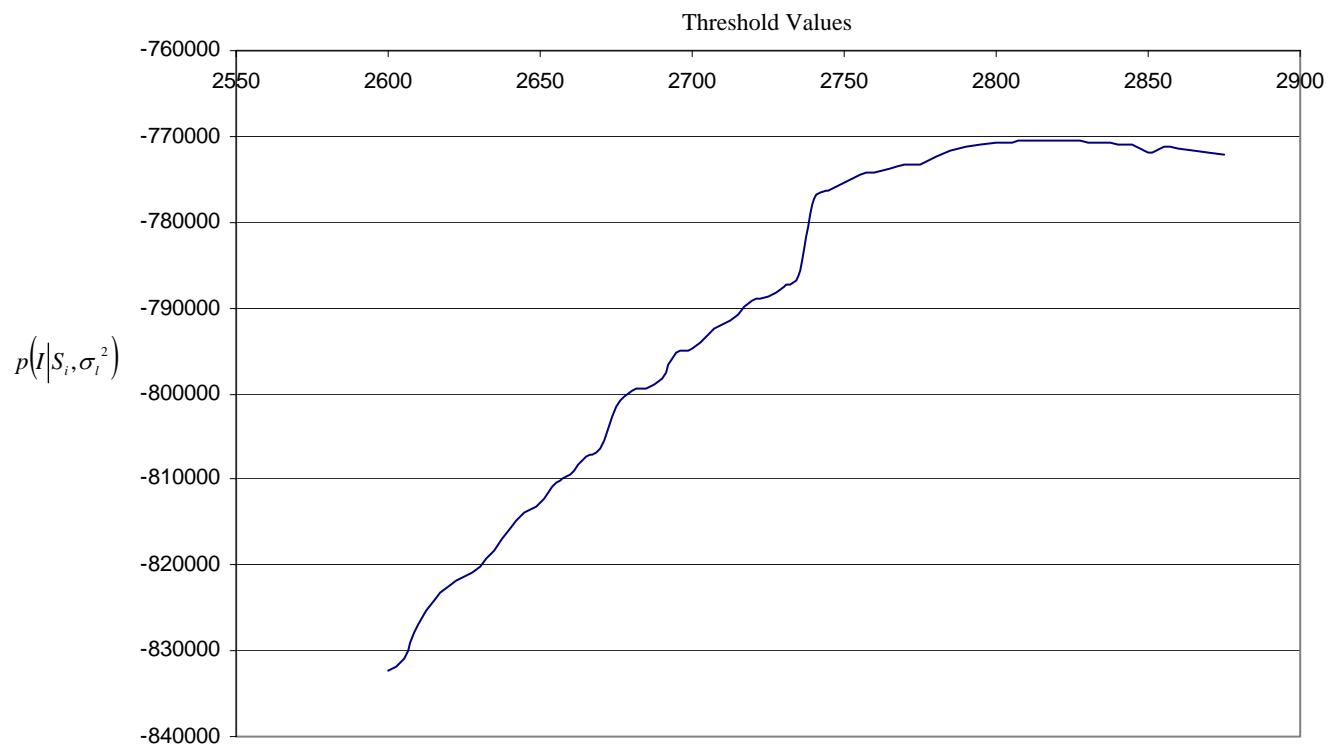
Figure 2 – Plot of the sum of the logarithm values for various image intensities
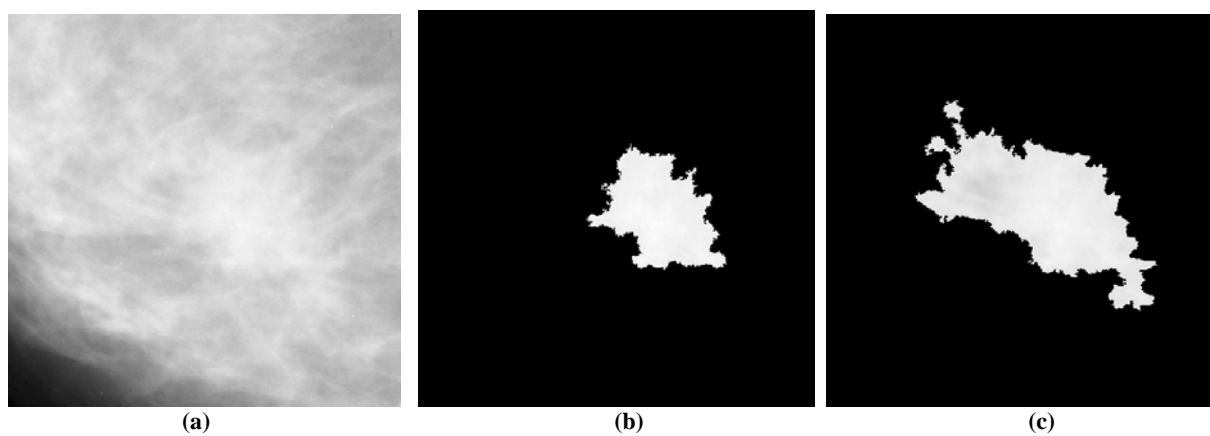

| (a) | (b) | (c) |

Figure 3 – (a) original image, (b) image of tumor body, (c) image of tumor body with extended borders

Instead of using the Gaussian enveloped image for the segmented region, we use the original image for each step of region growing in this study, simply because Gaussian enveloped image distorts the original intensities and boundaries. However, it facilitates the likelihood analysis by fuzzifying the tumor region. We found that this partition effectively segmented the tumor body, but often did not include the borders. We performed a study prior to the one described in this paper on 30 mammograms and discovered that the best segmentation result including the tumor margin occurs at the steepest ascent location on the plot of $p\left(I\middle|S_i,\sigma_l^2\right)$. In this particular study, the maximum value on the plot of $p\left(I\middle|S_i,\sigma_l^2\right)$ corresponded to the tumor body segmentation result (see **Figure 3**). **Figure 2** shows that this sharp increase occurs at intensity 2745, therefore it can be inferred that the best segmentation result is produced when the seed point intensity is approximately 2745. The maximum value on the curve occurs at intensity 2815, therefore, when the tumor body segmentation result was found for this particular intensity value.

We discovered that this method is particularly helpful when the masses have ill-defined borders. In most cases in which the mass boundary is ill-defined, the probability curve increases in a steady fashion, while the cases in which the mass boundary is well-defined, the steep ascent location is very abrupt. In some cases we found that this ascent location to be so abrupt, that it could be compared to a step function.

4. DISCUSSION AND CONCLUSION

We have developed a mass segmentation method that is capable of delineating a mass body, as well as its borders. We believe that it outperforms traditional region growing techniques. Traditional region growing without the use of a quantitative method can introduce a great deal of subjectivity because given a large number of segmentation results, what is perceived to the best one can vary greatly from one researcher to another. By analyzing the likelihood of the segmented regions, it is rational to identify that the maximum likelihood of the segmented regions corresponds to the tumor body and the maximum likelihood change of the segmented regions corresponds to the tumor margin. For the latter, we would like to indicate that when the segmented region significantly increases with the threshold increment, the likelihood value would also significantly change. In most cases, the significant change of the segmented region implies that the tumor margin grows and invades the surrounding tissues because their intensity difference is usually very small.

6. REFERENCES

[1] Brake GM te, Karssemeijer N, Segmentation of suspicious densities in digital mammograms, Medical Physics, 2001, vol. 28, no. 2, pp. 259-266.

[2] Heath M, Bowyer KW, Kopans D et al, "Current status of the Digital Database for Screening Mammography," *Digital Mammography*, Kluwer Academic Publishers, 1998, pp. 457-460.

[3] Kupinski MA, Giger ML, Automated Seeded Lesion Segmentation on Digital Mammograms, IEEE Transactions on Medical Imaging, 1998, vol. 17, no. 4, pp. 510-517.

[4] Gonzalez RC, Woods RE, Digital Image Processing Reading, MA: Addison Wesley, 1992.

[5] Li H, Wang Y, Liu KJR, Lo S-C, Freedman MT, Computerized Radiographic Mass Detection - Part I: Lesion Site Selection by Morphological Enhancement and Contextual Segmentation, IEEE Transactions on Medical Imaging, 2001, vol. 20, no. 4, pp. 289-301.

[6] Li L, Zheng Y, Zhang L, Clark R, False-positive reduction in CAD mass detection using a competitive classification strategy, Medical Physics, 2001, Vol. 28, no. 2, pp. 250-258.

[7] Mendez AJ, Tahoces PG, Lado MJ, Souto M., Vidal JJ, Computer-aided diagnosis: Automatic detection of malignant masses in digitized mammograms, Medical Physics, 1998, vol. 25, no. 6, pp. 957-964.

[8] Petrick N, Chan H-P, Sahiner B, Wei D, An Adaptive Density-Weighted Contrast Enhancement Filter for Mammographic Breast Mass Detection, IEEE Transactions on Medical Imaging, 1996, vol. 15, no. 1, pp. 59-67.

[9] Pohlman S, Powell KA, Obuchowski NA, Chilcote WA, Grundfest-Broniatowski S, "Quantitative classification of breast tumors in digitized mammograms", Medical Physics, 1996, vol. 23, no. 8, pp. 1336-1345.

[10] Sahiner B, Chan HP, Wei D, Petrick N, Helvie MA, Adler DD, Goodsit MM, Image feature selection by a genetic algorithm: Application to classification of mass and normal breast tissue, Medical Physics, 1996, vol. 23, no. 10, pp. 1671-1684.

[11] Sonka M, Hlavac V, Boyle R, "Image Processing, Analysis and Machine Vision".

[12] Tabar L, Dean P. Teaching Atlas of Mammography, Georg Thieme Verlag, Stuttgart, Germany, 1983, 1985.

7. ACKNOWLEDGMENTS

Separation of Malignant and Benign Masses Using Image and Segmentation Features

Lisa Kinnard [a,b], Shih-Chung B. Lo [a], Paul Wang [c], Matthew T. Freedman [a], Mohamed Chouikha [b]

[a]ISIS Center, Dept. of Radiology, Georgetown University Medical Center, Washington, D.C.
[b]Department of Electrical Engineering, Howard University, Washington, D.C.
[c]Biomedical NMR Laboratory, Department of Radiology, Howard University, Washington, D.C.

ABSTRACT

The purpose of this study is to investigate the efficacy of image features versus likelihood features of tumor boundaries for differentiating benign and malignant tumors and to compare the effectiveness of two neural networks in the classification study: (1) circular processing-based neural network and (2) conventional Multilayer Perceptron (MLP). The segmentation method used is an adaptive region growing technique coupled with a fuzzy shadow approach and maximum likelihood analyzer. Intensity, shape, texture, and likelihood features were calculated for the extracted Region of Interest (ROI). We performed these studies: experiment number 1 utilized image features used as inputs and the MLP for classification, experiment number 2 utilized image features used as inputs and the neural net with circular processing for classification, and experiment number 3 used likelihood values as inputs and the MLP for classification. The experiments were validated using an ROC methodology. We have tested these methods on 51 mammograms using a leave-one-case-out experiment (i.e., Jackknife procedure). The A_z values for the four experiments were as follows: 0.66 in experiment number 1, 0.71 in experiment number 2, and 0.84 in experiment number 3.

Keywords: Computer-assisted diagnosis, breast cancer, convolution neural networks, feature extraction

1. INTRODUCTION

Many studies have investigated the efficacy of various features used in Computer-Assisted Diagnostic (CAD_x) systems. Sahiner et al.[13] used texture and morphological features and used a genetic algorithm to select the best image features. In a study used to differentiate dense tissue from fatty tissue, Byng et al.[1] used fractal dimension and regional skewness as features. Qian et al.[12] calculated circularity, normalized deviation of radial length, intensity variation, mean intensity difference, and the mean gradient of region boundary. Wei et al.[16] calculated the following eight texture features from the co-occurrence matrix: correlation, energy, entropy, inertia, inverse difference moment, sum average, sum entropy, and difference entropy. In a later study, Sahiner et al.[15] calculated a Fourier descriptor, convexity, rectangularity, perimeter, Normalized Radial Length (NRL) mean, contrast, NRL entropy, circularity, NRL area ratio, NRL standard deviation, NRL zero crossing count, perimeter-to-area ratio, and area. These and other studies have been successful in finding features that are effective in separating from benign features, however, our study uses traditional features as well as segmentation features as inputs to two different classifiers.

In the United States, breast cancer accounts for one-third of all cancer diagnoses among women and it has the second highest mortality rate of all cancer deaths[4]. In various studies it has been shown that only 13% - 29% of suspicious lesions were determined to be malignant[11, 13, 17] which indicates that there are high false positive rates for biopsied breast lesions. A higher predictive rate is anticipated by combining the mammographer's interpretation and the computer analysis. This could be of great clinical value because a lower amount of false positives in breast biopsies would reduce anxiety among patients and their families. Other studies show that 7.6-14% of the patients have mammograms that produce false negative diagnoses[3, 8]. Alternatively, a CAD_x system can serve as a clinical tool for the radiologist and consequently lower the rate of missed breast cancer.

2. METHODOLOGY

The next several sections will describe the database, as well as provide the theoretical background used to develop the CAD_x experiment.

2.1 Database

The image samples were chosen from several databases compiled by the ISIS Center of the Georgetown University Radiology Department as well as the University of South Florida's (USF) Digital Database for Screening Mammography[4]. Twenty-eight malignant and twenty-three benign tumors were tested during this experiment.

2.2 Maximum Likelihood Segmentation Method

The segmentation method used in this study is an adaptive region growing technique coupled with a fuzzy shadow approach and maximum likelihood analyzer. The region growing technique aggregates surrounding pixels with similar properties, e.g., grayscale level. It is a commonly used method due to its simplicity and accuracy. The intensity threshold is usually used as a similarity criterion. We used the highest intensity as the seed point with multiple intensity threshold values and decreased the gray level in successive steps. This method by itself generated a sequence of contour on the mass; however, the computer did not have the ability to determine the boundaries interfered by other tissues and to choose the proper partition corresponding to the experts' perception. A fuzzy operator and a maximum-likelihood component were therefore added to the region-growing algorithm. The likelihood function is comprised of the likelihood of the composite probabilities for probability density functions (PDF's) inside ($p(S_i|pdf_i)$) and outside ($p(S_i|ROI)$) a given contour (see example contour in **Figure 1**)[2].

$$Log(P_i) = \log(p(S_i|pdf_i)) + \log(p(S_i|ROI)) \tag{1}$$

The subscript i represents the thresholding step, or, intensity value used to produce a given contour. The area inside the contour is the original ROI, which has been multiplied by a fuzzy shadow, whereas the area outside the contour is the original ROI. The likelihood that the contour represents the mass's extended borders is determined by assessing the maximum change of the likelihood function[5,6]:

$$\arg\max \frac{d(\log(P_i))}{di} \tag{2}$$

To summarize, the best contour is determined by locating the steepest jump in likelihood values, i.e., the intensity corresponding to this location will produce the best contour.
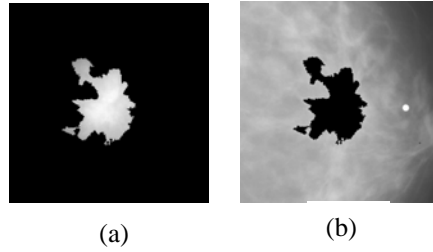
(a)   (b)

Figure 1:   (a) ROI used to calculate $p(S_m/pdf_i)$.   (b) ROI used to calculate $p(S_m/ROI)$ where m is the mth contour corresponding to the maximum value of likelihood function indicated in eq. (2).

2.3 Feature Calculation

The features used to separate the malignant and benign masses were a combination of 18 statistical descriptors along with the likelihood features.   The features have been separated into global features and sector features, where global features are those for which one value per mass is calculated.   Sector features are those features calculated on the 10° ROI as it was divided into 10° sectors in the polar coordinate system (see **Figure 2**); therefore, each mass contained 36 sectors.

Figure 2: Sample map used to calculate sector features

In this study, three sets of features were used.   One set of features is related to the use of the likelihood function curve which will be discussed in section 3.   The other sets of features are as follows:

Global Features: skewness, kurtosis, circularity, compactness, and mass perimeter.
Local Features: mean intensity value, contrast, standard deviation inside the sector, sector area, deviation of the normalized radial length, radial length, roughness, energy, inertia, entropy, inverse difference moment, and difference entropy.

2.4 Classifiers

We used a conventional Multilayer Perceptron (MLP) neural network for two of the three studies described in this paper. The standard backpropagation training method was used for the MLP. It was comprised of an input layer, one hidden layer, and one output. We used a Multiple Circular Path Neural Network[9] (MCPCNN) for the third study described in this paper (see **Figure 3**). It is comprised of 3 input layers, one hidden layer and one output. The first input layer is fully connected, i.e., all inputs connect to all hidden nodes. The second input layer is called a self correlation path, i.e., each node on the layer connects to a single set of the 18 image features for the fan-in and fully connects to the hidden nodes for fan-out. The third input layer is called a neighborhood correlation path, i.e., each node on the layer connects to the input nodes of adjacent sectors for the fan-in and fully connects to the hidden nodes for fan-out. Our study used 18 hidden layer nodes.
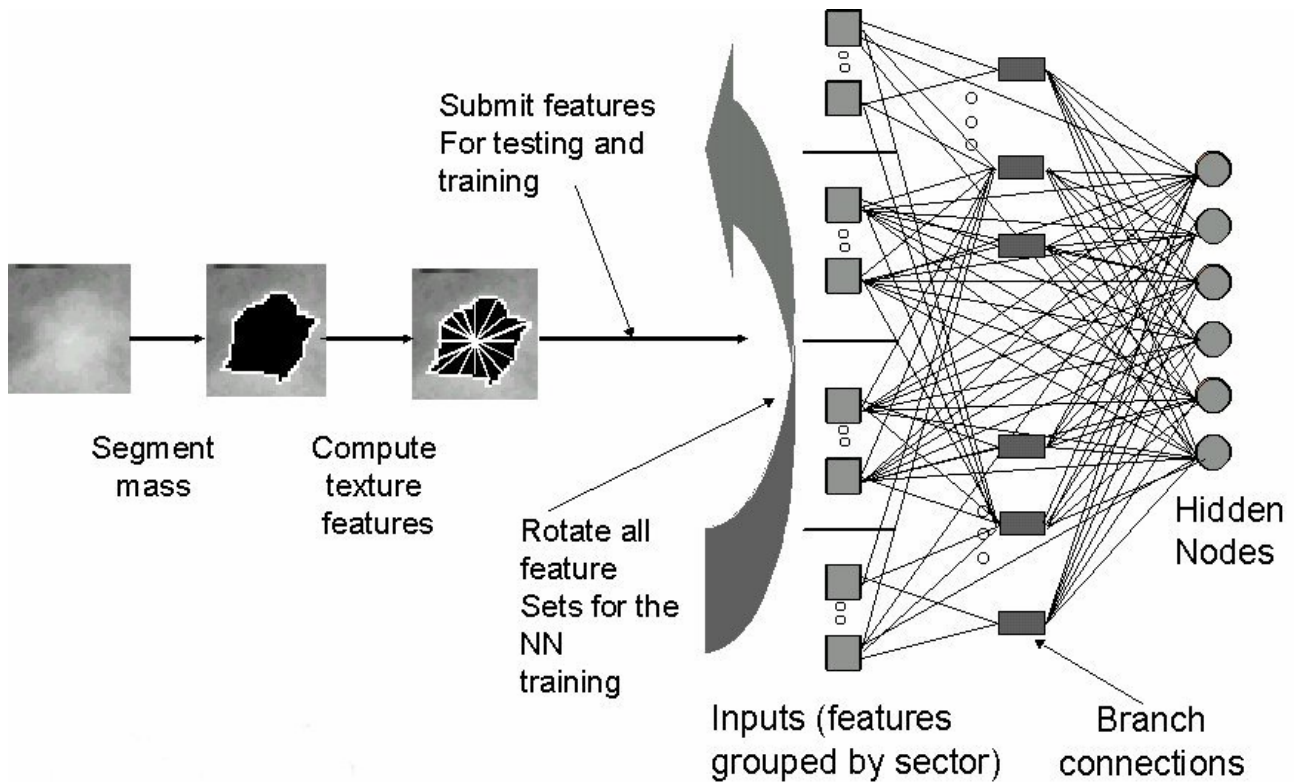

Figure 3: Multiple Circular Path Convolution Neural Network (MCPCNN)

3. EXPERIMENTS

In experiment 1 the input features consisted of 6 global image features combined with 12×36 sector image features to yield a total of 438 features. The classifier used for this experiment was a MLP neural network. It contained 18 hidden nodes and one output. Experiment 2 used the same image input features as those used in experiment 1, yet the classifier used for this experiment was the MCPCNN. The MCPCNN also contained 18 hidden nodes and one output. The neural networks were both tested and trained using the jackknife method. In experiment 3 the input values consisted of likelihood values that were extracted from the segmentation likelihood functions (see **Figures 5, 6**). The classifier used in this experiment was a MLP with 15 hidden nodes and one output. The neural network for this experiment was also tested and trained using the jackknife method. The results were analyzed using the LABROC4 analysis tool[10]. The experiments are summarized in **Table 1**.

4. RESULTS

The following table (**Table 1**) is a summary of the results achieved by the two classifiers used in the experiments described in section 2 of this paper. The corresponding ROC curves are shown in **Figure 4**. Two likelihood functions (features used in Experiment 3) along with their segmentation results (one malignant and one benign) are shown in **Figures 5** and **6**.

Table 1: Summary of Classification Results

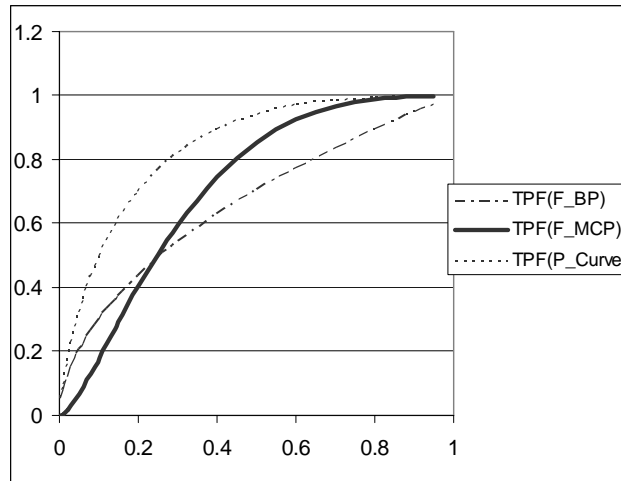| Experiment	Features	Neural Network	A_z values
1	Image Features	MLP	0.66
2	Image Features	MCPCNN	0.71
3	ML-curve as features	MLP	0.84

Figure 4:   ROC Results (TPF: True Positive Fraction, F_BP:Experiment 1, F_MCP: Experiment 2, P_Curve: Experiment 3)

Figure 5: The segmentation results for a malignant tumor. (a) likelihood function with respect to threshold values for all segmentation steps (b) original image, (c) segmentation result

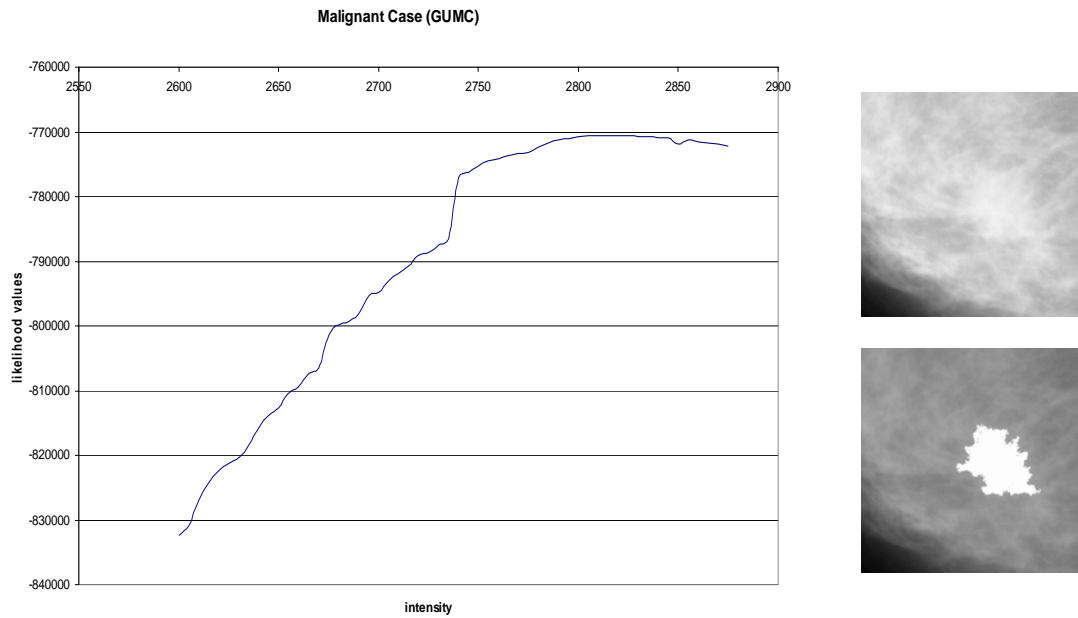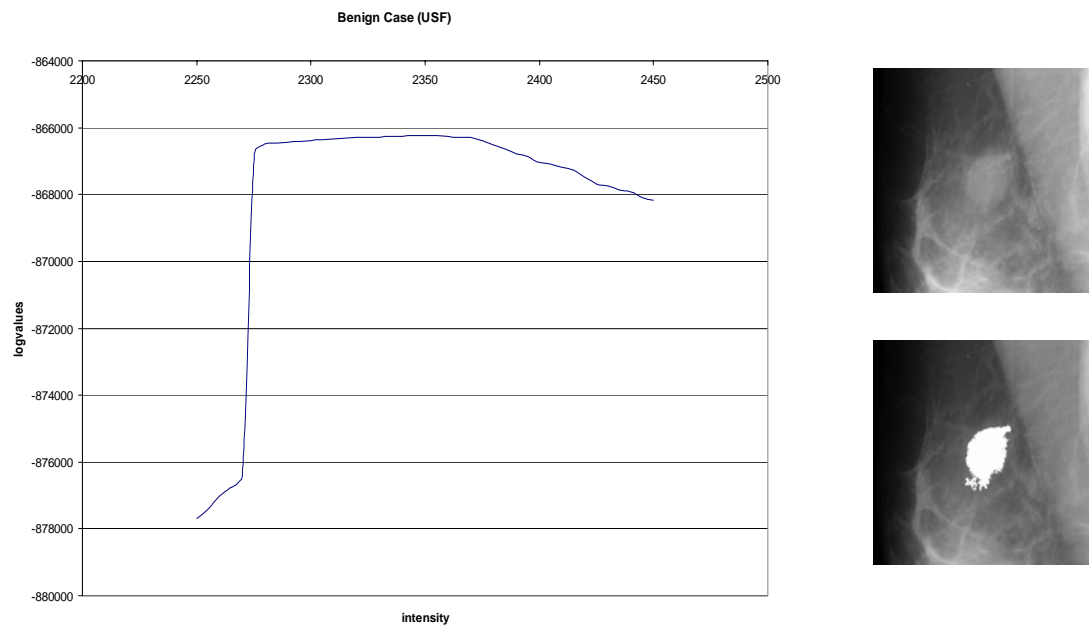**Figure 6:** The segmentation results for a benign tumor. (a) likelihood function with respect to threshold values for all segmentation steps (b) original image, (c) segmentation result

5. DISCUSSION OF RESULTS

In general there is a marked difference between the shape of the likelihood function for benign cases and the likelihood function for malignant cases (see **Figures 5-6**, i.e., the likelihood functions for benign cases experience a sharp drop and the likelihood functions for malignant cases are smoother, overall.   In the image, a sharp drop in likelihood value represents an abrupt change in segmented area.

Overall MCPCNN performed better (see **Figure 4**) than the conventional neural network, where the A_z value for Experiment 1 was 0.66, the A_z value for Experiment 2 was 0.71 and the A_z value for Experiment 3 was 0.84.   The likelihood functions used as features provided the best diagnostic results, with regard to neural network performance.   We believe that this phenomenon occurred because there is a clear difference between the appearance of the benign likelihood functions and the malignant likelihood functions. This may not be the case with regard to image features as some benign masses have malignant characteristics (e.g. - ill-defined borders) and vice versa.   In future work we plan to find likelihood functions for various sectors, because we believe that certain sectors hold more valuable information than others.   If we combine the feature information with likelihood functions found in the various sectors and use the MCPCNN, we could improve the performance in the classification of mammographic masses.

6. CONCLUSION

We found that the maximum likelihood method in conjunction with fuzzy shadow approach is an effective approach for not only segmenting masses, but for also using its results to separate malignant and benign masses.   Our method includes a fully-automated segmentation technique as well as the use of sector features that are designed for the separation of malignant and benign masses.   We have also shown that the Multiple Circular Path Convolution Neural Network is better at separating malignant from benign masses and that the best classifier performance is achieved when the maximum likelihood features are used as inputs.

ACKNOWLEDGMENTS

REFERENCES

1. Byng JW, Boyd NF, Fishell E, Jong RA, Yaffe MJ, Automated analysis of mammographic densities, Physics in Medicine and Biology, 1996, vol. 41, pp. 909-923.
2. Comer ML, Liu S, Delp EJ, Statistical Segmentation of Mammograms, Proceedings of the 3rd International Workshop on Digital Mammography, Chicago, IL, June 9-12, 1996, pp. 475-478.
3. Harvey JA, Fajardo LL, Innis, CA, Previous Mammograms in Patients with Impalpable Breast Carcinoma: Retrospective vs. Blinded Interpretation, American Journal of Roentgenology, 1993, vol. 161, pp. 1167-1172.

4. Heath M, Bowyer KW, Kopans D et al, Current status of the Digital Database for Screening Mammography}, Digital Mammography, Kluwer Academic Publishers, 1998, pp. 457-460.
5. Kinnard L, Lo S-C B, Wang P, Freedman MT, Chouikha M, Separation of Malignant and Benign Masses using a Maximum-Likelihood Analysis and Neural Networks, Proceedings of the SPIE Medical Imaging Conference, February, 2002, vol. 4684, part II, pp. 733-741.
6. Kinnard L, Lo S-C B, Wang P, Freedman MT, Chouikha M, Automatic Segmentation of Mammographic Masses Using Fuzzy Shadow and Maximum-Likelihood Analysis, Proceedings of the International Symposium on Biomedical Imaging (ISBI), July, 2002, pp. 241-244.
7. Lacey JV Jr, Devesa SS, Brinton LA, Recent trends in breast cancer incidence and mortality, 2002, vol. 39, no.2-3, pp. 82-88.
8. Martin JE, Moskowitz M, Milbrath JR, Breast Cancer Missed by Mammography, American Journal of Roengenology, 1979, vol. 132, pp. 737-739.
9. Lo SC, Li H, Wang J, Kinnard L, Freedman MT, A Multiple Circular Path Convolution Neural Network System for Detection of Mammographic Masses, IEEE Transactions on Medical Imaging, 2002, vol. 21, No. 2, pp. 150-158.
10. Metz C, LABROC Program, ftp://radiology.uchicago.edu/roc.
11. Meyer JE, Kopans DB, Stomper PC, Lindfors KK, Occult Breast Abnormalities: Percutaneous Preoperative Needle Localization, Radiology, 1984, vol. 150, no. 2, pp. 335-337.
12. Qian W, Li L, Clarke LP, Image feature extration for mass detection in digital mammography: Influence of wavelet analysis, 1999, Medical Physics, vol. 26, no. 3, pp. 402-408.
13. Rosenberg AL, Schwartz GF, Feig SA, Patchefsky AS, Clinically Occult Breast Lesions: Localization and Significance, Radiology, 1987, vol. 162, no. 1, pp. 167-170.
14. Sahiner B, Chan H-P, Wei D, Petrick N, Helvie MA, Adler DD, Goodsit MM, Image feature selection by a genetic algorithm: Application to classification of mass and normal breast tissue, Medical Physics, 1996, vol. 23, no. 10, pp. 1671-1684.
15. Sahiner B, Chan H-P, Petrick N, Helvie MA, Hadjiiski LM, Improvement of mammographic mass characterization using spiculation measures and morphological features, Medical Physics, 2001, vol.28, no. 7, pp. 1455-1465.
16. Wei D, Chan H-P, Helvie MA, Sahiner B, Petrick N, Adler DD, Goodsitt MM, False-positive reduction technique for detection of masses on digital mammograms: Global and local multiresolution texture analysis, Medical Physics, 1997, vol. 24, no. 6, pp. 903-914.
17. Yankaskas BC, Knelson MH, Abernethy ML, Cuttino JT, Clark RL, Needle Localization Biopsy of Occult Lesions of the Breast, vol. 23, no. 10, pp. 729-733.

LIKELIHOOD FUNCTION ANALYSIS FOR SEGMENTATION OF MAMMOGRAPHIC MASSES FOR VARIOUS MARGIN GROUPS

Lisa Kinnard[a,b,c], Shih-Chung B. Lo[a], Erini Makariou[a], Teresa Osicka[a,d], Paul Wang[c], Matthew T. Freedman[a], Mohamed Chouikha[b]

[a]ISIS Center, Dept. of Radiology, Georgetown University Medical Center, Washington, D.C., USA
[b]Department of Electrical and Computer Engineering, Howard University, Washington, D.C., USA
[c]Biomedical NMR Laboratory, Department of Radiology, Howard University, Washington, D.C., USA
[d]Department of Electrical Engineering and Computer Science, The Catholic University of America, Washington DC, USA

ABSTRACT

The purpose of this work was to develop an automatic boundary detection method for mammographic masses and to observe the method's performance on different four of the five margin groups as defined by the ACR, namely, spiculated, ill-defined, circumscribed, and obscured. The segmentation method utilized a maximum likelihood steep change analysis technique that is capable of delineating ill-defined borders of the masses. Previous investigators have shown that the maximum likelihood function can be utilized to determine the border of the mass body. The method was tested on 122 digitized mammograms selected from the University of South Florida's Digital Database for Screening Mammography (DDSM). The segmentation results were validated using overlap and accuracy statistics, where the gold standards were manual traces provided by two expert radiologists. We have concluded that the intensity threshold that produces the best contour corresponds to a particular steep change location within the likelihood function.

1. INTRODUCTION

In a CAD_x system, segmentation is arguably one of the most important aspects – particularly for masses – because strong diagnostic predictors for masses are shape and margin type [2,9]. The margin of a mass is defined as the interface between the mass and surrounding tissue [2]. Furthermore, breast masses can have unclear borders and are sometimes obscured by glandular tissue in mammograms. A spiculated mass consists of a central mass body surrounded by fibrous projections, hence the resulting stellate shape. For the aforementioned reasons, proper segmentation - to include the body and periphery - is extremely important and is essential for the computer to analyze, and in turn, determine the malignancy of the mass in mammographic CAD_x systems.

Over the years researchers have used many methods to segment masses in mammograms. Petrick [7] et al. developed the Density Weighted Contrast Enhancement (DWCE) method, in which series of filters are applied to the image in an attempt to extract masses. Comer et al. [1] segmented digitized mammograms into homogeneous texture regions by assigning each pixel to one of a set of classes such that the number incorrectly classified pixels was minimized via Maximum Likelihood (ML) analysis. Li [5] developed a method that employs k-means classification to classify pixels as belonging to the region of interest (ROI) or background.

Kupinski and Giger developed a method [4], which uses ML analysis to determine final segmentation. In their method, the likelihood function is formed from likelihood values determined by a set of image contours produced by the region growing method. This method is a highly effective one that was also implemented by Te Brake and Karssemeijer in their comparison between the discrete dynamic contour model and the likelihood method [9]. For this reason we chose to investigate its use as a possible starting point from which a second method could be developed. Consequently in our implementation of this work we discovered an important result, i.e., the maximum likelihood steep change. It appears that in many cases this method produces contour choices that encapsulate important borders such as mass spiculations and ill-defined borders.

2. METHODS

2.1 Initial Contours

As an initial segmentation step, we followed the overall region similarity concept to aggregate the area of interest [1, 4]. Used alone, a sequence of contours representing the mass is generated; however, the computer is not able to choose the contour that is most closely correlated with the experts' delineations. Furthermore, we have devised an ML function steep change analysis method that chooses the best contour that delineates the mass body as well as its extended borders, i.e., extensions into spiculations and areas in which the borders are ill-defined or obscured. This method is an extension of the method developed by Kupinski and Giger [4] that uses ML function analysis to select the contour which best represents the mass, as compared to expert radiologist traces. We have determined that this technique can select the contour that accurately represents the mass body contour for a given set of parameters; however, further analysis of the likelihood function revealed that the computer could

choose a set of three segmentation contour choices from the entire set of contour choices, and then make a final decision from these three choices.

The algorithm can be summarized in several steps. Initially, we use an intensity based thresholding scheme to generate a sequence of grown contours (S_i), where gray value is the similarity criterion. The image is also multiplied by a 2D trapezoidal membership function (2D shadow), whose upper base measures 40 pixels and lower base measures 250 pixels (1 pixel = 50 microns). The image to which the shadow has been applied is henceforth referred to as the "fuzzy" image. The original image and its fuzzy version were used to compute the likelihood of the mass's boundaries. The computation method is comprised of two components for a given boundary: (1) formulation of the composite probability and (2) evaluation of likelihood.

In addition, we chose to aggregate contours using the original image. This accounts for the major difference from that implemented by the previous investigators. Since smoother contours were not used, the likelihood function showed greater variations. In many situations, the greatest variations occurred when there was a sudden increase of the likelihood, and this was strongly correlated with the end of the mass border growth. This phenomenon would be suppressed if the fuzzy image was used to generate the contours. The fuzzy image was used mainly to construct the likelihood function.

2.2 Composite Probability Formation

For a contour (S_i), the composite probability (C_i) is calculated:

$$C_i | S_i = p\big(f_i(x,y)\big|S_i\big) \times p\big(m_i(x,y)\big|S_i\big) \qquad (1)$$

The quantity $f_i(x,y)$ is the area to which the 2D shadow has been multiplied, $p(f_i(x,y)|S_i)$ is the probability density function of the pixels inside S_i where 'i' is the region growing step associated with a given intensity threshold. The quantity $m_i(x,y)$ is the area outside S_i (non-fuzzy), and $p(m_i(x,y)|S_i)$ is the probability density function of the pixels outside S_i. Next we find the logarithm of the composite probability of the two regions, C_i:

$$Log\big(C_i|S_i\big) = \log\big(p\big(f_i(x,y)\big|S_i\big)\big) + \log\big(p\big(m_i(x,y)\big|S_i\big)\big) \quad (2)$$

2.3 Evaluation of Likelihood Function

The likelihood that the contour represents the fibrous portion of the mass, i.e., mass body is determined by assessing the maximum likelihood function:

$$\arg\max\big(Log\big(C_i|S_i\big)\big), S_i, i = 1,...n \qquad (3)$$

Equation (3) intends to find the maximum value of the aforementioned likelihood values as a function of intensity threshold. It has been assessed (also by other investigators [4]) that the intensity value corresponding to this maximum likelihood value is the optimal intensity needed to delineate the mass body contour. However, in our implementation it was discovered that the intensity threshold corresponding to the maximum likelihood value confines the contour to the mass body. In our study many of these contours did not include the extended borders. We, therefore, hypothesize that the contour represents the mass's extended borders may well be determined by assessing the maximum changes of the likelihood function, i.e., locate the steepest likelihood value changes within the function:

$$\frac{d}{di}\big(Log\big(C_i|S_i\big)\big), S_i, i = 1,\ldots,n \qquad (4)$$

Based on this assumption, we have carefully analyzed the behavior of maximum likelihood function. The analysis reveals that we have successfully discovered that the most accurate mass delineation is usually obtained by using the intensity value corresponding to the first or second steep change locations within the likelihood function immediately following the maximum likelihood value on the likelihood function.
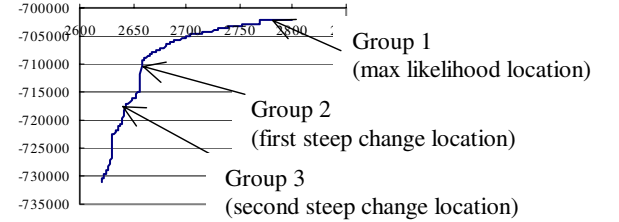

Figure 1: A likelihood function with steep change indicators

2.4 Steep change definition

The term "steep change" is rather subjective and can defined as a location between two or more points in the function where the likelihood values experience a significant change. In some cases the likelihood function increases at a slow rate. The algorithm design accounts for this issue by calculating the difference between likelihood values in steps over several values and comparing the results to two thresholds. The difference equation is given by:

$$h(t) = f(z - wt) - f(z - w(t+1)),\ \ t = 0,\ldots,N \qquad (5)$$

where f is the likelihood function, z is the maximum intensity, w is the width of the interval over which the likelihood differences are calculated (e.g. – for $w=7$ differences are calculated every 7 points), and N is the total number of points in the searchable area divided by w. If the calculation in question yields a value greater than or equal to a given threshold, then the intensity corresponding to this location is considered to be a steep change location. The threshold algorithm occurs as follows:

If $(h(t)_{ML} \geq ML_{T1})$; $t=0,\ldots,m$
Then choice 1 = intensity where that condition is satisfied
If $(h(t)_{ML} \geq ML_{T2})$; $t=m,\ldots,z$
Then choice 2 = intensity where that condition is satisfied

where $h(t)_{ML}$ is the steep change value given by equation (5), ML_{T1} and ML_{T2} are pre-defined threshold values, m is the location in the function where the choice 1 condition is satisfied, and z is the location in the function where the choice 2 condition is satisfied. Once the condition is satisfied for the first threshold value (ML_{T1}) then its corresponding intensity value is used to produce the segmentation contour for the first steep change location. Once the condition is satisfied for ML_{T2} then its corresponding intensity value is used to produce the segmentation contour for the second steep change location.

2.5 Validation

The segmentation method was validated on the basis of overlap and accuracy [8,10]:

$$Overlap = \frac{N_{TP}}{N_{FN} + N_{TP} + N_{FP}} \qquad (6)$$

114

$$Accuracy = \frac{N_{TP} + N_{TN}}{N_{TP} + N_{TN} + N_{FP} + N_{FN}} \quad (7)$$

where N_{TP} is the true positive fraction, N_{TN} true negative fraction, N_{FP} is the false positive fraction, and N_{FN} is the false negative fraction. The gold standards used for the validation study were mass contours, which have been traced by expert radiologists. Our experiments produced contours for the intensity values resulting from three locations within the likelihood functions: (1) The intensity for which a value within the likelihood function is maximum (group 1 contour) (2) The intensity for which the likelihood function experiences its first steep change (group 2 contour) and (3) The intensity for which the likelihood function experiences its second steep change (group 3 contour). We have observed that the intensity for which the likelihood function experiences its first steep change produces the contour trace that is most highly correlated with the gold standard traces, regarding overlap and accuracy.

3. EXPERIMENTS AND RESULTS

Here we describe the database used, describe the experiments, provide visual results obtained by the algorithm, as well as report the results obtained by the ANOVA test.

3.1 Database

For this study, a total of 122 masses were chosen from the University of South Florida's Digital Database for Screening Mammography (DDSM) [3]. The films were digitized at resolutions of 43.5 or 50 μm's using either the Howtek or Lumisys digitizers, respectively. The DDSM cases have been ranked by expert radiologists on a scale from 1 to 5, where 1 represents the most subtle masses and 5 represents the most obvious masses. The images were of varying subtlety ratings. The first set of expert traces was provided by an attending physician of the GUMC, and is hereafter referred to as the Expert A traces. The second set of expert traces was provided by the DDSM, and is hereafter referred to as the Expert B traces.

3.2 Experiments and Results

As mentioned previously, the term "steep change" is very subjective and therefore a set of thresholds needed to be set in an effort to define a particular location within the likelihood function as a "steep change location". For this study the following thresholds were experimentally chosen: ML_{T1}=1800, ML_{T2}=1300, where ML_{T1}= threshold for steep change location 1 for the likelihood function, and ML_{T2} = threshold for steep change location 2 for the likelihood function. We performed a number of experiments in an effort to prove that the intensity for which the likelihood function experiences the first steep change location produces the contour trace, which is most highly correlated with the gold standard traces regarding overlap and accuracy.

First we present segmentation results for two malignant cases followed segmentation results for two benign cases. Each figure contains an original image, traces for Experts A and B, and computer segmentation results for groups 1, 2, and 3. Second, we present data that plots the mean values for various margin groups for both overlap and accuracy measurements. The plots

present data for the spiculated and ill-defined groups of malignant masses, and ill-defined and circumscribed groups of benign masses. Data was not presented for the other categories because there was not a sufficient amount of cases.
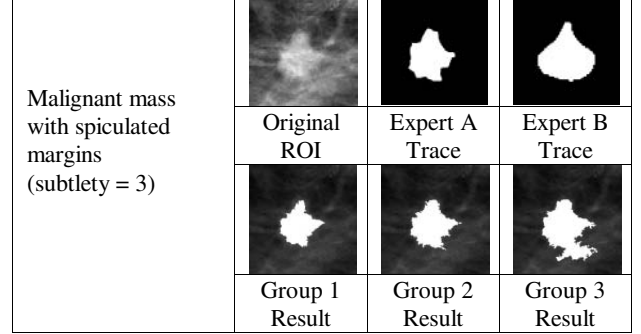
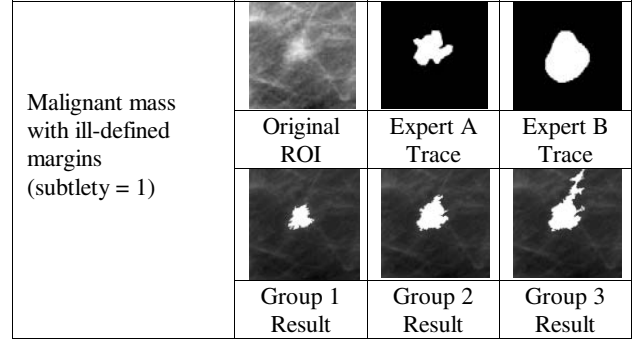Figure 2: Segmentation Results: Spiculated Malignant Mass

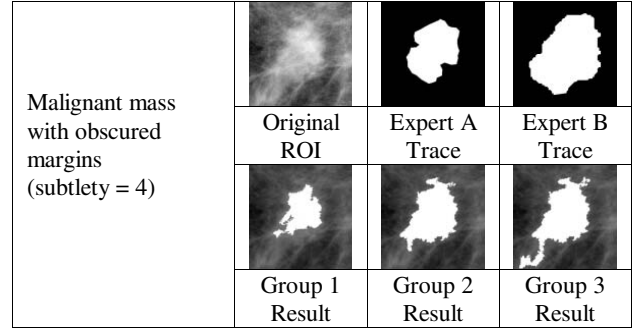Figure 3: Segmentation Results: Ill-defined Malignant Mass

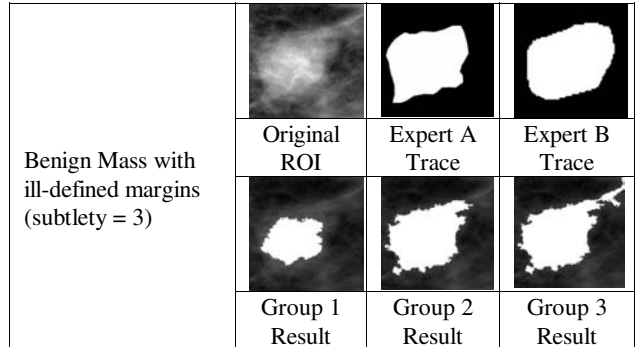Figure 4: Segmentation Results: Obscured Malignant Mass

Figure 5: Segmentation Results: Ill-defined Benign Mass

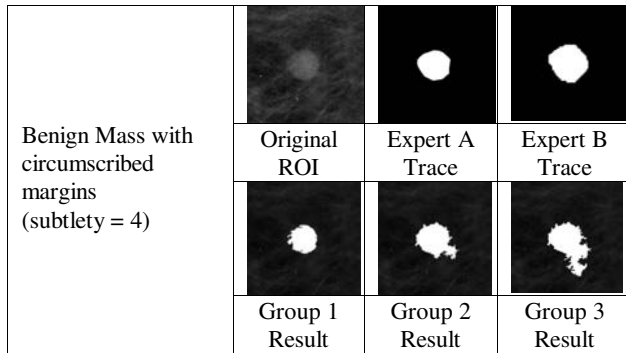| Benign Mass with circumscribed margins (subtlety = 4) | Original ROI | Expert A Trace | Expert B Trace |
| | Group 1 Result | Group 2 Result | Group 3 Result |

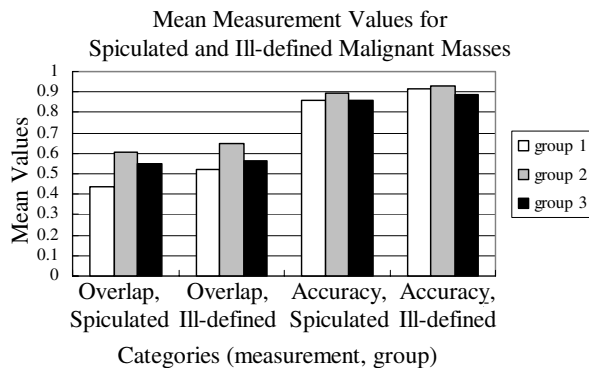Figure 6: Segmentation Results: Circumscribed Benign Mass

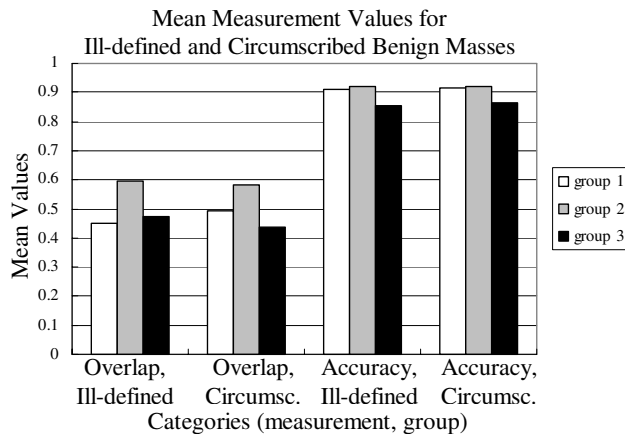Figure 7: Mean Measurement Values (Malignant Masses)

Figure 8: Mean Measurement Values (Benign Masses)

4. DISCUSSION AND CONCLUSION

The visual results (see Figures 2-6) reveal that the group 2 trace appears to delineate the masses better than the group 1 and group 3 contours in most cases. Visually, it appears that the method has performed equally well on all margin groups. This is an encouraging result because some of the more difficult masses to segment are typically those that are spiculated, obscured, and those that have ill-defined borders. The plots shown in Figures 7-8 confirm that the group 2 trace performs better than the other

groups on the basis of overlap and accuracy for all margin groups, therefore supporting our visual observations.

In future work, a worthwhile study would be to test gather more data for all margin groups in an effort to see if the various groups require different parameter values to maximize the algorithm's robustness. Our ultimate goal is to optimize its performance for those masses falling in the ill-defined and obscured margin groups because segmentation of masses falling into those categories is exceedingly difficult.

5. REFERENCES

[1] M.L. Comer, E.J. Delp, "The EM/MPM algorithm for segmentation of textured images: Analysis and further experimental results", *Proceedings of the 1995 IEEE ICIP*, Lausanne, Switzerland, September 16-19, 1996.

[2] J.R. Harris, M.E. Lippman, M. Morrow, S. Hellman, "Diseases of the breast", Lippincott-Raven Publishers, Philadelphia, PA, pp. 80-81, 1996.

[3] M. Heath, K.W. Bowyer, D. Kopans et al., "Current status of the digital database for screening mammography", Digital Mammography, Kluwer Academic Publishers, pp. 457-460 , 1998.

[4] M.A. Kupinski, M.L. Giger, "Automated Seeded Lesion Segmentation on Digital Mammograms", *IEEE Trans. on Med. Imag.*, vol. 17, no. 4, pp. 510-517, 1998.

[5] L. Li, Y. Zheng, L. Zhang, R. Clark, "False-positive reduction in CAD mass detection using a competitive classification strategy", *Med. Phys.*, vol. 28, pp. 250-258, 2001.

[6] J.E. Martin, "Atlas of mammography: histologic and mammographic correlations (second edition)", Williams and Wilkins, Baltimore, MD, p. 87, 1988.

[7] N. Petrick, H-P Chan, B. Sahiner, D. Wei, "An Adaptive Density-Weighted Contrast Enhancement Filter for Mammographic Breast Mass Detection", *IEEE Trans. on Med. Imag.*, vol. 15, no. 1, pp. 59-67, 1996.

[8] J. Suckling, D.R. Dance, E. Moskovic, D.J. Lewis, S.G. Blacker, "Segmentation of mammograms using multiple linked self-organizing neural networks", *Med. Phys.*, vol. 22, pp. 145-152, 1995.

[9] G.M. te Brake, N. Karssemeijer, "Segmentation of suspicious densities in digital mammograms", *Med. Phys.*, vol. 28, no. 2, pp. 259-266, 2001.

[10] B. Van Ginneken, "Automatic segmentation of lung fields in chest radiographs", *Med. Phys.*, 27, pp. 2445-2455, 2000.

ELSEVIER

Changes in biophysical parameters of plasma membranes influence cisplatin resistance of sensitive and resistant epidermal carcinoma cells

Xing-Jie Liang,[a] Jun-Jie Yin,[b] Jien-Wei Zhou,[c] Paul C. Wang,[c] Barbara Taylor,[a] Carol Cardarelli,[a] Michael Kozar,[d] Raynard Forte,[d] Adorjan Aszalos,[a] and Michael M. Gottesman[a],*

[a] Laboratory of Cell Biology, National Cancer Institute, National Institutes of Health, Bethesda, MD 20892-4254, USA
[b] Instrumentation and Biophysics Branch, Center for Food Safety and Applied Nutrition, Food and Drug Administration, College Park, MD 20740-3835, USA
[c] Department of Radiology, Howard University, Washington, DC 20060, USA
[d] Division of Experimental Therapeutics, Walter Reed Army Institute of Research, Silver Spring, MD 20910, USA

Abstract

The mechanism of resistance of cancer cells to the anticancer drug cisplatin is not fully understood. Using cisplatin-sensitive KB-3-1 and -resistant KCP-20 cells, we found that the resistant cells have higher membrane potential, as determined by membrane potential sensing oxonol dye. Electron spin resonance and fluorescence polarization studies revealed that the resistant cells have more "fluid" plasma membranes than the sensitive cells. Because of this observed difference in membrane "fluidity," we attempted modification of the plasma membrane fluidity by the incorporation of heptadecanoic acid into KB-3-1 and KCP-20 cell membranes. We found that such treatment resulted in increased heptadecanoic acid content and increased fluidity in the plasma membranes of both cell types, and also resulted in increased cisplatin resistance in the KCP-20 cells. This finding is in accord with our results, which showed that the cisplatin-resistant KCP-20 cells have more fluid membranes than the cisplatin-sensitive KB-3-1 cells. It remains to be determined whether the observed differences in biophysical status and/or fatty acid composition alone, or the secondary effect of these differences on the structure or function of some transmembrane protein(s), is the reason for increased cisplatin resistance.
© 2003 Elsevier Inc. All rights reserved.

Keywords: Cisplatin resistance; Heptadecanoic acid; Plasma membrane fluidity; Membrane potential; Fluorescence polarization; Human epidermal carcinoma KB cells

Introduction

Cis-diamminodichloroplatinum II (cisplatin) is one of the most useful anticancer drugs. Treatment protocols for solid tumors of the esophagus, bladder, ovary, testes, head, and neck include this drug. As for most antitumor agents, resistance develops in cancer cells, limiting their efficacy. The reason for resistance against cisplatin is not fully understood. Several mechanisms have been suggested, including decreased cisplatin accumulation [1,2], and alter-

ation of apoptotic signaling [3,4]. Reports also indicate that alterations in growth regulating proteins, such as c-Myc [5], inhibition of caspase-9 [6], and reduced inhibition of DNA synthesis [7] are associated with cisplatin resistance. Involvement of plasma membrane lipids in cisplatin resistance has also been implicated [8]. Britz et al. [9] succeeded in decreasing cisplatin resistance by treating monoclonal cells with a free or liposome-encapsulated bile acid derivative.

Our interest was focused on the biophysical status of plasma membranes in relation to cisplatin resistance. We investigated the biophysical differences between cisplatin-resistant and -sensitive cells and the influence of a fatty acid inserted into the plasma membranes on cisplatin sensitivity of human epidermal carcinoma KB cells.

* Corresponding author. Laboratory of Cell Biology, Center for Cancer Research, National Cancer Institute, National Institutes of Health, Room 1A-09, 37 Convent Drive, Bethesda, MD 20892-4254. Fax: +1-301-402-0450.
E-mail address: mgottesman@nih.gov (M.M. Gottesman).

Materials and methods

Cell lines

The KB-3-1 cell line was derived from a single clone of human KB epidermal carcinoma cells (a HeLa subclone), after two subclonings, as described by Akiyama et al. [10]. The cisplatin-resistant subline of KB-3-1 cells was selected by exposure to 0.5 μg/ml cisplatin (KB-CP.5) for 42 days. After that, single clones were picked and propagated in medium containing 0.5 μg/ml cisplatin. One other cisplatin-resistant cell line, KCP-20, was obtained after 6 months' exposure of KB-3-1 cells to increasing concentrations of cisplatin, up to 20 μg/ml [11]. KCP-20 cells were maintained in medium containing 5 μg/ml cisplatin and taken out of cisplatin before making the measurements. All cell lines were grown in Dulbecco's modified Eagle medium (Invitrogen, Grand Island, NY), supplemented with L-glutamine, penicillin, streptomycin (Quality Biological, Gaithersburg, MD), and 10% fetal bovine serum (Whittaker Bioproducts, Walkersville, MD).

Membrane potential measurements

Membrane potential measurements were performed by flow cytometry, using the negatively charged DiBaC4 (3) oxonol dye (Molecular Probes, Eugene, OR), essentially as described earlier [12]. Briefly, a cell suspension of 1×10^6 cells/ml was equilibrated for 1 min in PBS followed by the addition of oxonol dye, 150 M. After exactly 2 min equilibration at room temperature, histograms were collected from 10^4 cells. Reproducibility was determined by measuring membrane potentials of the cells on different days, from separate cultures, and by comparing the relative fluorescence of the oxonol-stained cell types.

Oxonol fluorescence intensity measures membrane potential when the extracellular potassium concentration is changed from 5 to 150 mM, resulting in increased fluorescence intensity of the oxonol-stained cells and thus making the cells depolarized. All measurements were made with a Becton Dickinson FACSCalibur flow cytometer (Becton Dickinson, Mountain View, CA), operated with a 15-mW argon ion laser tuned to 488-nm excitation wavelength. Fluorescence emission was collected at 525 nm. Results are expressed in comparative histograms of representative series.

Polarity of fluorescent membrane probes in live cells

Measurements of steady-state fluorescence polarization were done with a spectrofluorometer LS50B (Perkin Elmer, Norwalk, CT) and the lipid-soluble fluorophore, 1-(4-trimethylammoniumphenyl)-6-phenyl-1,3,5-hexatriene (TMA-DPH) (Molecular Probes). This fluorophore is known to probe plasma membranes of cells at the surface. TMA-DPH was dissolved in tetrahydrofurane at a concentration of 2 mM and was kept in the dark at 4°C. Cells (10^6/ml) were

labeled with TMA-DPH at a concentration of 2 μM in PBS. After 10 min incubation time at 4°C, the cell suspension was centrifuged and washed two times in the centrifuge with PBS. After resuspension in PBS, fluorescence anisotropy was measured at 25°C. The excitation wavelength was 355 nm and the emission was measured at 430 nm with a slit width of 5. Polarization values were calculated according to Collins and Scott [13] by the equation $P = (I_{0,0} - G * I_{0,90}) / (I_{0,0} + G * I_{0,90})$ from the measured fluorescence intensities.

Electron spin resonance (ESR) studies on live cells

ESR studies were conducted with 5-doxyl stearic acid (5-doxyl-SA) and with 2,2,6,6-tetramethyl piperidin-1-oxyl-4-yl-octadecenoate (T-SASL) probes (Molecular Probes). The first probe intercalates to the 5 carbon depth in the outer leaflet of the plasma membrane [14] and T-SASL at the surface of the plasma membranes [15]. Labeling the cells with the spin probes was done as follows: 5-doxyl-SA was dissolved in ethanol, 1 mg/ml, and was kept at 4°C. Then, 1×10^7 cells were mixed with 8×10^{-8} mol spin label in 0.02 ml volume of PBS. After 1 min contact time, the cell suspension was transferred into a 50-μl micropipette capillary tube and sealed at the bottom with Critoseal (Syva Co., Palo Alto, CA). The micropipette with the cells was placed into the cavity of a Varian E-9 Century series spectrometer (Syva Co.). ESR spectra were recorded at X-band, at 9.5 kHz, 100-field modulation, 4-Gous modulation amplitude, 100-Gous sweep range, and at 10 mW microwave power. The temperature of the probe was set to 24°C by the variable temperature accessory using N_2 gas flow. Evaluation of the obtained ESR spectra, when 5-doxyl-SA was used, was by the equation expressing the order parameter S:

$$S = 0.5407 \ (T_{11} - T_1)/a_0, \text{ where } a_0 = (T_{11} + 2T_1)/3$$

and T_{11} and T_1 are the outer and inner tensors obtained from the ESR spectra.

When the T-SASL probe was used, the same instrument parameters were applied, except that the incident microwave power was 20 mW. The spectral parameters, h_0 and h_{-1} are the spectral amplitudes and the ratio h_0/h_{-1} defines the motional freedom of the probe according to Yin et al. [15]. With both spin labels, the ESR spectra show contribution from spin labels of restricted motion with no contribution from the free-moving spin label.

Lipid packing of plasma membranes in live cells

Plasma membrane lipid packing can be studied by inserting the fluorescence probe merocyanine 540 (MRC 540) (Molecular Probes) into cell membranes and assessing the degree of insertion by fluorescence intensity measurement, using flow cytometry [16,17]. The experiment was according to Schlegel et al. [16] with some modifications. Briefly, 1×10^7 cells, suspended in 1 ml of PBS were treated with 10 μl of

a MC540 stock solution of 1 mg/ml, in 60% ethanol, 40% water. After a 10-min incubation at room temperature, cells were pelleted in a centrifuge, washed once in PBS by centrifugation, resuspended in 1 ml PBS, and fluorescence histograms were obtained. A Becton Dickinson FACSCalibur flow cytometer (Becton Dickinson, Franklin Lakes, NJ) was used at 488-nm excitation and 575-nm emission wavelength. Histograms were collected with 10^4 cells. Results are expressed as means of fluorescence of the histograms obtained from duplicate measurements of one typical set of cells.

Preparation of cells for NMR spectrometry

KB-3-1 and KCP-20 cells were grown to 90% confluence, harvested with 0.05% trypsin, 0.53 μM EDTA, centrifuged at 4°C at 730 × g for 10 min, and washed twice with growth medium. To perform a long-term NMR study, the cells were restrained in an agarose thread [18,19]; 0.5 ml of $(9 \times 10^7$ cells) was mixed with an equal volume of liquid agarose in phosphate-buffered saline, and immersed in a bath at 37°C for 5–7 min. The mixture was extruded under low pressure through cooled tubing (0.5 mm ID) into a 10-mm NMR tube containing growth medium. Using 0.5-mm threads ensures that there is no metabolic compromise, and the cells are viable and in stable energetic status for a long period of time, while the threads maintain their mechanical strength. The gel threads, which fill the tube, are concentrated without compression at the bottom of the NMR tube by insertion of a plastic insert with the perfusion fitting. A Teflon inflow tube (0.5 mm ID) was placed near the bottom of the tube. The gel threads were perfused with growth medium at 0.9 ml/min. Cells were continuously perfused for more than 40 h. Accumulation of data was started within 30 min after the harvest.

NMR spectrometry of live cells

The ^{31}P NMR spectra were recorded at 37°C on a Varian XL-400 machine (Varian Associates, Inc., Palo Alto, CA) at 162 MHz using RF pulse corresponding to a 72° flip angle and 2 s repetition time. The flip angle used was the Ernst angle for phosphocreatine (PCr) (T1 relaxation time, 3 s). There were more than 40 spectra obtained. Each spectrum contained 1800 transients and took 1 h. During the entire study, the system was deuterium locked with an external source (99.9% D_2O in a capillary, Sigma, St. Louis, MO) to avoid magnetic field drift.

All the spectra were transformed and viewed separately to confirm that the spectra did not change during the experiment. There were 25,000 data points collected and zero-filled to 8k before Fourier transformation. The spectra were added and 10-Hz line broadening was applied to obtain Fig. 3. The chemical shifts were standardized to β-adenosinetriphosphate (β-ATP) set to −18.70 ppm. Many phosphorus metabolites were identified, including phosphocholine (PC,

3.57 ppm), inorganic phosphate (Pi, 2.59 ppm), glycerophosphoethanolamine (GPE, 0.81 ppm), glycerophosphocholine (GPC, 0.26 ppm), phosphocreatine (PCr, −2.69 ppm), γ-adenosine triphosphate (γ-ATP, −5.12 ppm), α-adenosine triphosphate (α-ATP, −10.19 ppm), and diphosphodiesters (dPdE, −10.86, −12.58 ppm). Chemical shifts of these molecules are also listed in the literature [18,19].

Treatment of cells with heptadecanoic acid and cell proliferation studies

Treatment of KB-3-1 and KCP-20 cells with heptadecanoic acid was carried out in 24-well plates (Corning Inc., Corning, NY), with modification of the method used by Callaghan et al. [20]. After exploratory dose selection studies for cisplatin and heptadecanoic acid, the final conditions were as follows: cells $(10^6$/ml) were incubated in appropriate medium, as described above for both cell types, and after 2–3 days of incubation, the medium was withdrawn and replaced by serum-free medium. Following 6 h incubation at 37°C, 5% CO_2 medium was replaced by serum-free medium containing different concentrations of heptadecanoic acid or nothing. This incubation was followed by replacement of the medium with complete medium containing cisplatin or nothing. KB-3-1 cells were treated with 0.08 μg/ml and KCP-20 cells with 5 μg/ml cisplatin from a stock solution of 500 μg/ml aqueous solution. Cells were harvested after 5–6 days' incubation and treated with heptadecanoic acid alone, with cisplatin alone, heptadecanoic acid plus cisplatin or nothing, and were counted after trypsinization by a Coulter Particle Counter (Coulter Electronics, Luton, UK). Calculation of proliferation was based on cells treated with nothing as 100%. The expected yield was: cell count of cells treated with heptadecanoic acid alone multiplied by cell count of cells treated with cisplatin alone. The cell count of cells treated with both reagents was then related to the previous cell count product and tabulated.

Preparation of plasma membranes for determination of relative fatty acid composition

For the purpose of plasma membrane preparation, 10^7 cells from each cell line were harvested at log phase and washed with ice-cold PBS. Cells were sedimented by centrifugation and then suspended in ice-cold hypotonic solution (0.5 mM KH_2PO_4, 0.1 mM EDTA containing 1% protease inhibitor aprotinin, pH 8.0) for 5 min. Cells were disrupted on ice by a tight Dounce homogenizer with constant 40 strokes. Samples were checked for complete disruption in a phase-contrast microscope. Homogenates were centrifuged at 2000 × g for 10 min at 4°C to discard the nuclei and then the supernatant was centrifuged at 25,000 × g for 25 min to pellet all other organelles. The resulting supernatant was further centrifuged for 55 min at 4°C. The membranes sedimented at the bottom and were stored at −80°C before fatty acid analysis. To determine

that the sediment contained only plasma membranes and no membranes of organelles, markers were used in connection with Western blot analyses. For a positive marker, the anti-integrin antibody anti-2/VLA-2α was used according to Emsley et al. [21].

Conversion of plasma membrane lipids to methyl esters and fatty acid analysis

Fats were extracted into organic phase by vortexing the membrane preparations obtained as described above, with minor modification of the methods of Kozar et al. [22]. In brief, 2 ml of HPLC-grade water (Fisher Scientific, Pittsburgh, PA) was added to the membranes together with 3.75 ml of 2:1 (v/v) methanol/chloroform (Fisher Scientific) and the suspension was vortexed for 15 min. Then, after addition of 1 ml chloroform and 1 min vortexing, the suspension was centrifuged for 10 min at 2000 rpm. The separated organic phase was dried in an N_2 stream and heated in 1 ml 2 M methanolic HCl [11 ml methanol with dropwise addition of 2.5 ml acetyl chloride (Sigma)] at 85°C for 18 h in a screw-capped tube. The fatty acid methyl esters which formed were then extracted into heptane for GC-MS analysis. Samples were analyzed on a Hewlett-Packard 6890 plus GC equipped with 7683 auto-injector. The injection port was held at constant 280°C with 2 μl injected in the spitless mode onto a DB-5 ms capillary column with 30 m × 0.25 mm ID × 0.25 μm film thickness (J&W Scientific, Folsom, CA). Initial oven temperature was 80°C with a ramp of 40°C/min to a final temperature of 290°C and hold for 0.75 min. Helium was used as the carrier gas at a constant velocity of 41 cm/s. Electron impact ionization at 70 eV was performed using standard autotune conditions. The source temperature was maintained at 230°C while the quadrupoles were maintained at 150°C. FAMEs were analyzed in full scan mode for qualitative identification as well as in selected ion monitoring mode for ratio determination. Location of the analyzed two fatty acids in the obtained chromatograms was ascertained by standards of hexa- and heptadecanoic acid methyl esters (Sigma). The ratio of heptadecanoic acid to hexadecanoic acid methyl esters was determined since heptadecanoic acid was used to treat the cells and the hexadecanoic acid content of cells was assumed to be constant. This ratio is defined as the area under the peak for hexadecanoic acid/area under the peak for heptadecanoic acid methyl esters.

Visualization of distribution of K^+ channels in cells by immunofluorescence microscopy

For visualization of distribution of K^+ channels in cells, cells were grown on 189-mm glass coverslips in petri dishes. Cells were fixed with 3.5% formaldehyde in PBS for 10 min, followed by 0.1% Triton X-100 treatment for 5 min for permeabilization. After washing, cells were treated with 3% BSA in PBS for 30 min and subsequently treated with the primary antibody (Ab) for 1 h. The Ab was TW1K-

2 (P-19) goat polyclonal Ab (Santa Cruz Biotechnology, Santa Cruz, CA). After five washings, cells were incubated with Cy^{TM}3-conjugated affinity pure donkey anti-goat, secondary Ab (1:100 dilution) (Jackson Immuno-research Laboratory). Cells were washed extensively after the secondary Ab treatment. The slides with the treated cells were mounted on microscope slides with fluorescence mounting medium (Dako, Carpinteria, CA). Background fluorescence was determined from cells treated only with the secondary Ab, but otherwise treated the same way as described with the primary Ab. Fluorescent images were collected with a Bio-Rad 1024 confocal scan head mounted on a Nikon Optiphot microscope with a 60× planapochromat lens. Excitation at 568 nm was provided by a krypton–argon gas laser. An emission filter of 598/40 was used for collecting red fluorescence in channel one and phase contrast images of the same cell were collected in another channel using a transmitted light detector.

Results

Membrane potential of cisplatin-sensitive and -resistant cells

Membrane potential was measured using several series of independently grown cell cultures. For each measurement at different times and with the different cell lines, we observed the same pattern of membrane potentials. Fig. 1 shows one typical result of several measurements with the series of the cells. The KCP-20 cells, which are highly resistant to cisplatin, had lower fluorescence intensities and thus are hyperpolarized as compared to cisplatin sensitive and single-step, low-level resistant cells (KB-CP.5). Oxonol is a negatively charged membrane potential sensing dye and therefore less dye diffuses into membranes of cells which are more negative, and thus are hyperpolarized.
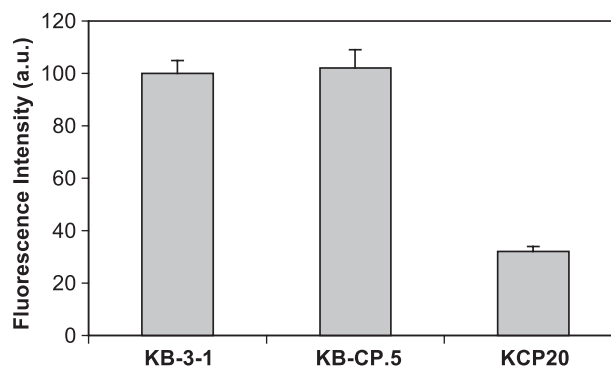
Fig. 1. Relative membrane potential of cisplatin-sensitive KB-3-1 and -resistant cells is indicated by the fluorescence of oxonol (150 mM)-stained cells. Oxonol is a negatively charged membrane potential sensing dye and was used as detailed in Materials and methods. One typical series of measurement of cells were grown simultaneously in culture ($n = 2-3$). $P < 0.05$ between KB-3-1 and KCP-20 cells. No statistical difference exists between KB-3-1 and KB-CP.5 cells.

Polarity of the fluorescent TMA-DPH molecule in the plasma membrane of live cells

The TMA-DPH fluorescence probe was used to measure the fluidity of plasma membranes because it has been shown that this probe does not penetrate into the cells and probes at the upper leaflet of the membrane [13]. Table 1 shows the results obtained with sensitive KB-3-1 and resistant KB-20 cells treated or not treated with heptadecanoic acid. Cisplatin-resistant KCP-20 cells were found to have membranes which were more fluid; the calculated polarization number, P, was of lower value. These results parallel those obtained with ESR measurements (see below). Also, polarization numbers obtained with the TMA-DPH probe indicate that heptadecanoic acid treatment of the cells results in lower polarization numbers. Therefore, the plasma membranes become more fluid. These results also parallel those obtained by ESR measurements (see below).

ESR studies on the motional freedom of ESR probes, 5-doxyl-SA and T-SASL, in the plasma membranes of cells

Two ESR probes were used to measure membrane fluidity in cisplatin-sensitive KB-3-1 and -resistant KCP-20 cells. 5-doxyl-SA probes at 5 carbon depth in the outer leaflet, while the T-SASL probes at the surface of the plasma membrane [14,15]. Table 2 shows both results. The calculated order parameters, S, for the 5-doxyl-SA yielded lower numbers for the cisplatin-resistant KCP-20 cells, indicating more ''fluid'' membranes of these cells at 24°C. The calculated h_0/h_{-1} parameters also indicate a more fluid membrane for the cisplatin-resistant KCP-20 cells. These results are in line with those of the polarization experiments.

To measure membrane fluidity changes of heptadecanoic acid treated KB-3-1 and KCP-20 cells, we employed the 5-doxyl-SA ESR probe. Fig. 2 shows the results and indicates that both types of cells became more fluid (had lower S values) after heptadecanoic acid treatment. The heptadecanoic acid-treated KCP-20 cells were shown to be more resistant than the nontreated KCP-20 cells. This result is consistent with the fact that the cisplatin-resistant KCP-20

Table 1
Polarity[a] of TMA-DPH fluorescence probe, inserted into plasma membranes of heptadecanoic acid[b]-treated and untreated cisplatin-sensitive (KB-3-1) and -resistant (KCP-20) cells

Cells/treatment	Polarity	±SD
KB-3-1 untreated	0.3668	0.0018
KB-3-1 treated	0.3590	0.0013
KCP-20 untreated	0.3612	0.0018
KCP-20 treated	0.3556	0.0016

[a] Mean polarization numbers are calculated from six independent measurements.
[b] Heptadecanoic acid treatment is detailed in Materials and methods. Heptadecanoic acid (40 μM) was used in each experiment. $P < 0.05$ between treated and untreated cells as well as between KB-3-1 and KCP-20 cells.

Table 2
Motional freedom[a] of 5-doxyl-SA and T-SASL ESR probes inserted into the plasma membranes of cisplatin-sensitive and -resistant cells

Cells	Temp, °C	5-doxyl-SA, order parameter, S		T-SASL, h_0/h_{-1}	
		S	±SD	h_0/h_{-1}	±SD
KB-3-1	24	0.6443	0.0038	2.423	0.093
KCP-20	24	0.6208	0.0111	1.820	0.147

[a] Order parameter, S, and h_0/h_{-1} were calculated as described in Materials and methods. Experiments were done with several cultures ($n = 2-4$), and ESR measurements were in triplicate; $P < 0.05$.

cells were found to have more fluid plasma membranes than the sensitive KB-3-1 cells by both ESR and polarization techniques (Tables 1 and 2). Contrary to this, the cisplatin-sensitive KB-3-1 cells became even more sensitive after heptadecanoic acid treatment, despite the fact that their plasma membranes became more fluid after this treatment (data not shown).

Membrane packing as determined by fluorescence intensity of merocyanine 540-stained cells

Merocyanine (MRC) 540 staining was found to be indicative of the lipid packing density of cell plasma membranes [16]. We applied this measurement to cisplatin-sensitive KB-3-1 and -resistant KCP-20 cells as detailed in Materials and methods, and found that cisplatin resistant cells had lower fluorescence intensity than the sensitive KB-3-1 cells. The fluorescence intensity of merocyanine540-stained KB-3-1 cells was 95 ± 10 while that of the resistant KCP-20 cells was 58 ± 12 in a typical cell preparation ($n = 3$). We interpret these results to mean that in KB-3-1 cell membrane lipids are more tightly packed and intercalate MRC 540 more tightly than in KCP-20 cells. These results parallel those of membrane fluidity measurements by the polarization and ESR methods (Tables 1 and 2).

Fig. 2. Membrane ''fluidity'' as expressed by the order parameter, S, of cisplatin-sensitive KB-3-1 and -resistant KCP-20 cells, treated or not treated with heptadecanoic acid. Order parameters, S, were calculated from ESR spectra obtained as described in Materials and methods. Heptadecanoic acid treatment is also described in Materials and methods. Average of three to four measurements are shown with SDs. There is a statistically significant difference between S values of heptadecanoic acid treated and untreated cells for both types of cells ($P < 0.05$).

Assessment of phospholipids in cisplatin-sensitive KB-3-1 and -resistant KCP-20 cells by ^{31}P NMR spectrometry

Spectra obtained by 400-MHz NMR spectrometry were compared to detect any difference in phospholipid composition between cisplatin-sensitive KB-3-1 and -resistant KCP-20 cells. The two cell line types were grown in the same media, harvested before confluence, and spectra were obtained as described in Materials and methods. Similar experiments have been performed for the detection of such differences between P-glycoprotein expressing and nonexpressing cells [23,24]. Spectra from both cells detected phospho-ethanolamine, 4.11 ppm; -choline, 3.6 ppm; -creatine, −2.69 ppm; glycerophospoethanolamine, 0.7 ppm, and choline, 0.1 ppm, besides inorganic phosphate and different adenosintriphosphates (Fig. 3). No significant differences could be detected between the two cell lines in the above listed phospholipid signals with the applied NMR technique.

Cell proliferation of heptadecanoic acid-treated and untreated cells

Cell proliferation studies were done as described in Materials and methods. Relative cell counts are shown in Table 3. Results indicate that heptadecanoic acid treatment increased resistance of the KCP-20 cells to cisplatin, since
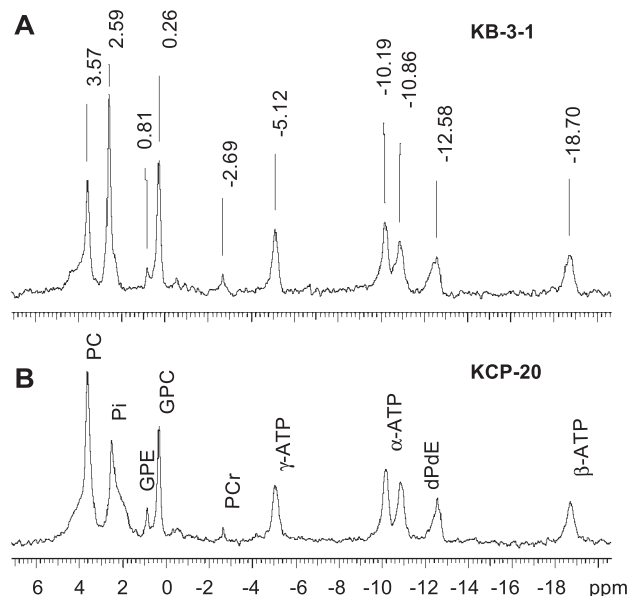

Fig. 3. ^{31}P NMR spectra (400 MHz) of cisplatin-sensitive KB-3-l (A) and -resistant KCP-20 (B) cells. Cells (9 × 10^7) from each culture were embedded in agarose and packed in 10-mm NMR tubes. Many water-soluble phosphates were identified, including phosphocholine (PC, 3.57 ppm), inorganic phosphate (Pi, 2.59 ppm), glycerophosphoethanolamine (GPE, 0.81 ppm), glycerophosphocholine (GPC, 0.26 ppm), phosphocreatine (PCr, −2.69 ppm), γ-adenosine triphosphate (γ-ATP, −5.12 ppm), α-adenosine triphosphate (α-ATP, −10.19 ppm), diphosphodiesters (dPdE, −10.86 ppm, −12.58 ppm), and β-adenosinetriphosphate (β-ATP, −18.70 ppm).

Table 3
Cell proliferation as expressed in percentage ± SD cell growth relative to nontreated KB-3-1 and KCP-20 cells in the presence and absence of treatment with heptadecanoic acid or cisplatin or the combination of both

Cells	Treatment	% Proliferation	
		Expected	Found
KB-3-1	[a] cisplatin (0.8 μg/ml)	–	85 ± 6
	[b] HAD^a (20 μM)	–	97 ± 3
	[c] HDA (40 μM)	–	94 ± 4
	[a] × [b]	82 ± 8	49 ± 15
	[a] × [c]	80 ± 10	68 ± 12
KCP-20^b	[d] cisplatin (5 μg/ml)	–	67 ± 10
	[e] HDA (40 μM)	–	68 ± 5
	[f] HDA (50 μM)	–	41 ± 11
	[d] × [e]	45 ± 14	62 ± 6
	[d] × [f]	27 ± 20	46 ± 5
	[g] cisplatin (6 μg/ml)	–	51 ± 8
	[h] HDA (40 μM)	–	68 ± 13
	[i] HDA (50 μM)	–	41 ± 7
	[g] × [h]	34 ± 21	47 ± 5
	[g] × [i]	19 ± 19	23 ± 7

^{a} HDA: heptadecanoic acid.
^{b} KCP-20 cells: Each measurement of cell growth was done in triplicate wells and each dose was used in multiple experiments with separately grown cell cultures ($n = 3–5$). $P < 0.05$ for the difference between expected growth and actual growth for all experiments, except for KCP20 cells treated with cisplatin, 6 μg/ml and 50 μM HDA.

the cells grew better in the combination of cisplatin and heptadecanoic acid than would have been mediated from the growth of these cells in either agent alone. In contrast, heptadecanoic acid treatment of the sensitive KB-3-1 cells increased their sensitivity to cisplatin.

Fatty acid analysis in heptadecanoic acid-treated and nontreated plasma membranes

Results of the fatty acid analysis are shown in Table 4. Two sets of membrane preparations were made from

Table 4
Area^a and ratios of area of hexadecanoic and heptadecanoic acids as measured by GC-MS in the membranes of heptadecanoic acid-treated and untreated KB-3-1 and KCP-20 cells

Cells/treatment	Area at m/z 270 heptadecanoic acid^a	Area at m/z 284 m/z 270/m/z 284	Ratio of hexadecanoic acid
KB-3-1	5,243,334	65,763	79.73
KB-3-1 + treatment	14,684,547	1,998,304	7.35
KB-3-1	13,859,715	260,720	53.16
KB-3-1 + treatment	15,527,957	1,789,737	8.68
KCP-20	17,554,572	321,183	54.66
KCP-20 + treatment	11,695,325	2,260,349	5.17
KCP-20	6,596,479	122,458	53.87
KCP-20 + treatment	7,656,383	1,332,033	5.75

^{a} Area under peaks obtained by GCMS represents fatty acid methyl esters analyzed in full scan mode with the instrument software.

treated and untreated sensitive and resistant cells. For each preparation, Western blot analyses indicated that only plasma membranes were collected (not shown). Results indicated that heptadecanoic acid treatment increased this fatty acid relative concentration to hexadecanoic acid in both cell lines. The hexadecanoic acid content of cell membranes was used to normalize the relative concentration of heptadecanoic acid.

Fluorescence visualization of K^+ channels in human epidermal carcinoma KB cells

Fig. 4 shows fluorescence images of the KB-3-1 and KCP-20 cells stained with the $Cy^{MB}3$-conjugated affinity pure donkey anti-goat Ab after incubation of the cells with the primary TW1K-2 (P-19) goat polyclonal Ab. The red fluorescence intensities indicate that there are substantially more K^+ channels on the plasma membranes of KCP-20 cells than of KB-3-1 cells.
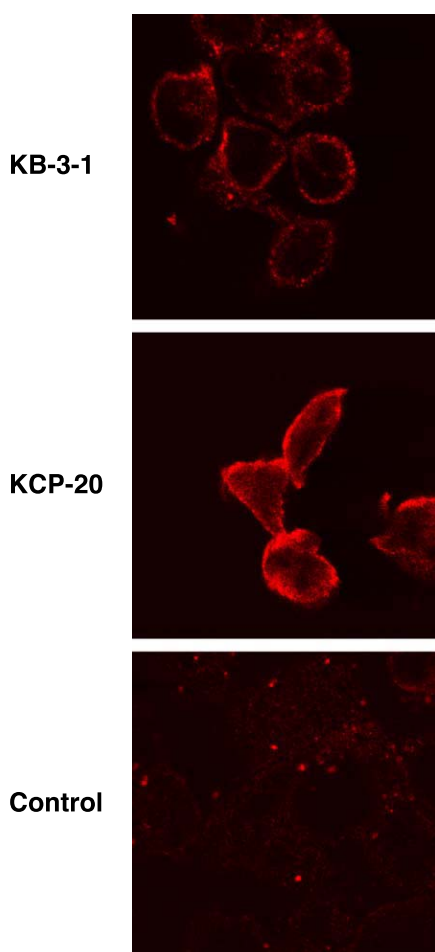

Fig. 4. Confocal visualization of K^+ channels as detected by TW1K-2 primary and $Cy^{TM}3$-conjugated donkey anti-goat secondary Ab. Ab treatment and confocal microscopy are detailed in Materials and methods. Several fields of cells were captured and one representative field of each is shown ($n = 5–8$). Control: KCP-20 cells treated only with secondary Ab.

Discussion

We used five different methods to study biophysical differences in the plasma membranes of cisplatin-sensitive KB-3-1 adenocarcinoma cells and their cisplatin-resistant counterparts. We also influenced these biophysical differences in the plasma membranes of KB cells by inserting heptadecanoic acid into the cell membranes. The alteration of lipid composition by addition of heptadecanoic acid resulted in changes in some biophysical parameters of the membranes along with changes in the cells' resistance to cisplatin.

First, we showed that the highly resistant KCP-20 cells have higher membrane potential, and are therefore more hyperpolarized than the sensitive, parental KB-3-1 cells and the low level resistant KCP.5 cells (Fig. 1). We have attributed this increased membrane potential of KCP-20 cells to the increased expression of K^+ channels on their plasma membranes (Fig. 4). Our results are in line with the observation of Thomson et al. [25] that cisplatin treatment of cells influences K^+ channel activity and that of Mahaswari et al. [26] that cisplatin can change ion conductivity in bilayer lipid membranes. Efflux of K^+ from cells can elevate membrane potential. Second, polarization studied with the TMA-DPH fluorescence probe, which probes at the outer leaflet of plasma membranes, indicates that the resistant KCP-20 cells have lower polarization values, and thus have more fluid plasma membranes than the sensitive KB-3-1 cells (Table 1). Third, similar conclusions could be drawn from the ESR studies, performed with two types of ESR probes. Results indicate that the order parameter, S, and parameters of the measurements with the second probe, h_0/h_{-1}, are lower for the resistant cells, indicating more fluid membranes for these cells as compared to the sensitive cells (Table 2).

Fourth, more MRC 540 fluorescent dye is packed into the plasma membranes of the sensitive KB-3-1 cells than into the plasma membranes of the resistant KCP-20 cells (see Results). We have interpreted this difference by assuming that more "rigid" membranes can bind more of this dye tightly than the more loosely packed membranes. Both cells are equal in size, so more dye incorporation into a cell cannot be interpreted from different cell sizes. Our interpretation, based on our polarization and ESR measurements done with the same cells with which we performed our MRC 540 lipid packing experiment, is seemingly contrary to the interpretation of Schlegel et al. [16] and Stillwell et al. [17]. However, Schlegel's experiments with lymphocytes could not be interpreted in terms of the ability of MRC 540 to distinguish between loosely or tightly packed membranes. Stillwell found that more MRC 540 dye intercalates into loosely packed membranes of phospholipid vesicles, but he made no such comparison with live cells. His experiments with the T27A leukemia cells demonstrated only that MRC 540 intercalates into docosahexanoic acid modified cells differently than into the nonmodified cells and no interpre-

tation was given for the relationship between membrane fluidity and dye packing. In a previous study [27], MRC 540 intercalated into cisplatin-sensitive and -resistant lung adenocarcinoma cells with the same relative dye ratio as in our study. Unfortunately, no correlation was made between dye packing and membrane fluidity in that study.

We have not detected any significant difference between the 400 MHz ^{31}P NMR spectra of KB-3-1 and KCP-20 cells (Fig. 3), suggesting that there are no major differences in measured water-soluble phosphates, including phospholipid precursors in the cisplatin-sensitive and -resistant cell lines. Our results reflect relative peak intensities of individual phosphates which depend on their T1 relaxation times and the repetition time (2 s) of the applied NMR technique. Spellman [8] found that phosphatidylserine binds cisplatin in vitro, but formation of a phosphatidylserine–cisplatin complex could not be found when experiments were conducted with intact cells [28]. Kaplan et al. [23] found that there are differences in the glycerophosphocholine and glycerophosphoethanolamine ratio in some MCF-7 wild type and P-glycoprotein expressing cell lines by their ^{31}P NMR studies. However, these differences proved not consistently present in all such cell lines.

We found differences in biophysical parameters between the KB-3-1-sensitive and the KB-20-resistant cells, as described above. Therefore, our next experiment focused on the introduction of biophysical changes to the plasma membrane of the sensitive and the resistant KB cells and determining the cisplatin sensitivity of the altered cells. In a previous study, Callaghan et al. [20] found that the incorporation of heptadecanoic acid into plasma membranes can hinder the function of a transmembrane protein, P-glycoprotein, possibly by altering the biophysical milieu of this transmembrane protein. Therefore, we incorporated this fatty acid into the plasma membrane of KB-3-1 and KCP-20 cells. We demonstrated that during a short treatment period of the cells with this fatty acid, other components of the plasma membrane, such as the cholesterol content, did not change significantly.

After heptadecanoic acid treatment of our cells, we determined changes in membrane biophysical status, relative heptadecanoic acid content, and sensitivity of the treated cells to cisplatin. We found that heptadecanoic acid treatment of the cells increases the relative content of this fatty acid in cell membranes (Table 4). Simultaneously, this treatment increased the fluidity of plasma membranes of both KB-3-1 and KCP-20 cells as measured by polarization (Table 1) and by ESR (Fig. 2). We also measured the influence of heptadecanoic acid treatment on cell proliferation (Table 3). After heptadecanoic acid treatment of KCP-20 cells, their resistance to cisplatin increased (Table 3) and their plasma membrane fluidity increased (Fig. 2). This finding is in accord with our results that the resistant KCP-20 cells have more fluid plasma membranes than the sensitive KB-3-1 cells, as discussed above. That a bile acid derivative increased sensitivity of monoclonal cells to cis-

platin, as reported by Briz et al. [9], is not a direct contradiction to our findings. First, it was not shown by Briz et al. whether the bile acid derivative was incorporated into plasma membranes, and second, no determination was made on the biophysical status of the membranes of the cells before and after the treatment.

Contrary to the results with the KCP-20 cells, KB-3-1 cells became more sensitive to cisplatin after heptadecanoic acid treatment (Table 3). In this case, increasing the fluidity of the plasma membrane did not result in higher resistance to cisplatin, as it did with the KCP-20 cells. Nevertheless, cisplatin sensitivity was altered by heptadecanoic acid treatment in these cells also. Further experiments with cell lines of different plasma membrane fluidity and sensitivity to cisplatin may explain these results. Results detailed above, that incorporation of heptadecanoic acid into plasma membranes of KB-3-1 and KCP-20 cells resulted in opposite sensitivity to cisplatin, indicate that this fatty acid per se is not involved in cisplatin binding. Somewhat different results were obtained by Timmer-Bosscha et al. [29] who found that incorporation of docosahexaenonoic acid into the membranes of a human small cell lung carcinoma line, GLC4 and its resistant subline, GLC4-CP, decreased resistance of the resistant cells but had no influence on the parent cell line. However, their experimental results suggested that DNA-related effects, and not alteration in the plasma membrane, are the reasons for changes in resistance. Interestingly, these authors also found that their treatment does not cause the same change in cisplatin resistance in the parental as in the resistant cells. Our results parallel this different effect on sensitive and resistant cells. In both cases, this difference suggests that increased fluidity per se may not be responsible for cisplatin resistance, but may facilitate a mechanism of resistance found only in the selected cell line.

Recent physiological studies on the mechanism of resistance of KCP-20 cells to cisplatin (and cross-resistance to other compounds such as methotrexate) have revealed the following phenotype: (1) decreased drug accumulation for many drugs associated with decreased expression on the cell membrane of many different transporters, carriers, and channels [11]; (2) neutralization of the usual acidic pH of lysosomes and endosomes [30]; (3) hypermethylation of genes whose expression is decreased in KCP-20 cells (Shen, D.-W., Liang, X.-J., Pai-Panandiker, A., and Gottesman, M.M., unpublished data); and (4) mislocalization of membrane proteins with accumulation of certain transporters in the cytoplasm [31]. Although a single molecular defect is unlikely to account for all of these changes in cells selected in multiple steps, alteration of the biophysical properties of plasma membranes in cisplatin-resistant cells could facilitate defects in membrane protein trafficking which might underlie cisplatin resistance due to decreased accumulation. If increased membrane fluidity amplifies the effect of another defect in KB-CP20 cell membranes, rather than independently causing resistance to cisplatin, this could explain why

measured membrane fluidity in the KB-3-1 parental, drug-sensitive cells does not result in resistance.

To summarize, we have determined that there are differences in biophysical parameters, membrane potential, motional freedom of polarization and ESR probes, and MRC 540 dye packing between cisplatin-sensitive and -resistant human epidermal carcinoma cells in vitro. ^{31}P NMR studies indicated no essential differences in water-soluble phosphates. Modification of the plasma membrane fluidity of these cells by incorporation of heptadecanoic acid resulted in changes in their sensitivity to cisplatin. Whether changes in membrane fluidity transmitted to some membrane molecules in sensitive and resistant cells cause alterations in cisplatin sensitivity remains to be determined.

References

[1] Z.S. Chen, M. Mutoh, T. Sumizawa, T. Furukawa, M. Haraguchi, A. Tani, N. Saijo, T. Kondo, S.I. Akiyama, An active efflux system for heavy metals in cisplatin-resistant human KB carcinoma cells, Exp. Cell Res. 240 (1998) 312–320.

[2] M. Bungo, Y. Fujiwara, K. Kasahara, K. Nakagawara, Y. Ohe, Y. Sasaki, S. Irino, N. Saijo, Decreased accumulation as a mechanism of resistance to cis-diamminodichloro platinum (II) in human non-small cell lung cancer cell lines: relation to DNA damage and repair, Cancer Res. 50 (1990) 2549–2553.

[3] H. Burger, K. Nooter, A.W. Boersma, C.J. Kortland, G. Stoter, Expression of p53, Bcl-2 and Bax in cisplatin-induced apoptosis in testicular germ cell tumor cell lines, Br. J. Cancer 77 (1998) 1562–1567.

[4] J. Kigawa, S. Sato, M. Shimada, M. Takahasi, H. Itamochi, Y. Kanamori, N. Terakwa, p53 gene status and chemosensitivity in ovarian cancer, Hum. Cell 14 (2001) 165–171.

[5] S. Adachi, A.J. Obaya, Z. Han, N. Ramos-Desimone, J.H. Wyche, J.M. Sedivy, c-Myc is necessary for DNA damage-induced apoptosis in the G phase of cell cycle, Mol. Cell. Biol. 21 (2001) 4929–4937.

[6] D. Kuwahara, K. Tsutsumi, T. Kobayashi, M. Hyoudou, I. Koizuka, Inhibition of caspase-9 activity in cisplatin-resistant head and neck squamous cell carcinoma, Nippon Jibi Inkoka Gakkai Kaiho 105 (2002) 152–157.

[7] S. Lin-Chao, C.C. Chao, Reduced inhibition of DNA synthesis and G(2) arrest during the cell cycle of resistant HeLa cells in response to cis-diamminedichloroplatinum, J. Biomed. Sci. 1 (1994) 131–138.

[8] G. Spellman, R.W. Staffhorst, K. Versluis, J. Reedijk, B. de Kruijff, Cisplatin complexes with phosphatidylserine in membranes, Biochemistry 36 (1997) 10545–10550.

[9] O. Briz, M.A. Serrano, R.I.R. Macias, J.J.G. Marin, Overcoming cisplatin resistance in vitro by a free and liposome-encapsulated bile acid derivative: Bamet-R2, Int. J. Cancer 88 (2000) 287–292.

[10] S. Akiyama, A. Fojo, J.A. Hanover, I. Pastan, M.M. Gottesman, Isolation and genetic characterization of human KB cell lines resistant to multiple drugs, Somatic Cell Mol. Genet. 11 (1985) 117–126.

[11] D.-W. Shen, S. Akiyama, P. Schoenlein, I. Pastan, M.M. Gottesman, Characterization of high-level cisplatin-resistant cell lines established from a human hepatoma cell line and human KB adenocarcinoma cells: cross-resistance and protein changes, Br. J. Cancer 71 (1995) 676–683.

[12] P. Csermely, E. Balint, P.M. Grimley, A. Aszalos, Protein kinase C is involved in the early signal of interferon-α but not of interferon-γ in U937 cells, J. Interferon Res. 10 (1990) 605–611.

[13] I.M. Collins, R.B. Scott, Plasma membrane fluidity gradients of human peripheral blood leukocytes, J. Cell. Physiol. 144 (1990) 42–51.

[14] A. Aszalos, G.C. Yang, M.M. Gottesman, Depolymerization of microtubules increases the motional freedom of molecular probes in cellular plasma membranes, J. Cell Biol. 100 (1985) 1357–1363.

[15] J.J. Yin, M.J. Smith, R.M. Epply, A.L. Troy, S.W. Page, J.A. Sphon, Effects of furnorisin B1 and (hydrolyzed) fumonisin backbone API on membranes: a spin-label study, Arch. Biochem. Biophys. 335 (1996) 13–22.

[16] R.A. Schlegel, M. Stevens, K. Lurnley-Sapanski, P. Williamson, Altered lipid packing identifies apoptotic thymocytes, Immunol. Lett. 36 (1993) 283–288.

[17] W. Stillwell, S.R. Wassall, A.C. Dumaual, W.D. Ehringer, C.D. Browning, L.G. Jeskin, Use of merocyanine (MC540) in quantifying lipid domains and packing in phospholipid vesicles and tumor cells, Biochim. Biophys. Acta 1146 (1993) 136–144.

[18] D.L. Foxall, J.S. Cohen, J.B. Mitchell, Continuous perfusion of mammalian cells embedded in agarose gel threads, Exp. Cell Res. 154 (1984) 521–529.

[19] D.L. Foxall, J.S. Cohen, NMR studies of perfused cells, J. Magn. Reson. 52 (1983) 346–349.

[20] R. Callaghan, A. Stafford, R.M. Epand, Increased accumulation of drugs in multidrug resistant cells by alteration of membrane biophysical properties, Biochim. Biophys. Acta 1175 (1993) 277–282.

[21] J. Emsley, S.L. King, J.M. Bergelson, R.C. Liddington, Crystal structure of the I domain from integrin alpha2beta1, J. Biol. Chem. 272 (1997) 28512–28517.

[22] M.P. Kozar, M.T. Krahmer, A. Fox, L. Larsson, J.H. Allton, Lunar dust: a negative control for biomarker analyses of extra-terrestrial samples? Geochim. Cosmochim. Acta 65 (2001) 3307–3317.

[23] O. Kaplan, J.W. Jaroszewski, R. Clarke, C.R. Fairchild, P. Schoenlein, S. Goldenberg, M.M. Gottesman, J.S. Cohen, The multidrug resistance phenotype: 31p nuclear magnetic resonance characterization and 2-deoxyglucose toxicity, Cancer Res. 51 (1991) 1638–1644.

[24] O. Kaplan, P.C.M. van Zijl, J.S. Cohen, NMR studies of metabolism of cells and perfused organs, NMR Basic Principles and Progress, vol. 28, Springer, Berlin, 1992, pp. 3–52.

[25] S.W. Thomson, L.E. Davis, M. Kornfeld, R.D. Hilgers, J.C. Standefer, Cisplatin neuropathy, clinical, electrophysiologic, morphology, and toxicologic studies, Cancer 54 (1984) 1269–1275.

[26] K.U. Mahaswari, T. Ramachandran, D. Rajaji, Interaction of cisplatin with planar model membranes—Dose dependent change in electrical characteristics, Biochim. Biophys. Acta 1463 (2000) 230–240.

[27] X.-J. Liang, Y.G. Huang, Physical state changes of membrane lipids in human lung adenocarcinoma A$_{549}$ cells and their resistance to cisplatin, Int. J. Biochem. Cell Biol. 34 (2002) 1248–1255.

[28] K.N.J. Burger, W.H.M. Rutger, M. Staffhorst, B.D. Kruijff, Interaction of the anti-cancer drug cisplatin with phosphadidylserine in intact and semi intact cells, Biochim. Biophys. Acta 1419 (1999) 43–54.

[29] H. Timmer-Bosscha, G.A. Hospers, C. Meijer, N.H. Mulder, F.A. Muskiet, I.A. Martini, D.R. Uges, E.G. de Vries, Influence of docosahexaenoic acid on cisplatin resistance in a human small cell lung carcinoma cell line, J. Natl. Cancer Inst. 81 (1989) 1069–1075.

[30] S.S. Chauhan, X.-J. Liang, A.W. Su, A. Pai-Panandiker, D.-W. Shen, J.A. Hanover, M.M. Gottesman, Reduced endocytosis and altered lysosome function in cisplatin resistant cell lines, Br. J. Cancer 88 (2003) 1327–1334.

[31] X.-J. Liang, D.-W. Shen, S. Garfield, M.M. Gottesman, Mislocalization of membrane proteins associated with multidrug resistance in cisplatin-resistant cancer cell lines, Cancer Res. 63 (2003) 5909–5916.

Steepest changes of a probability-based cost function for delineation of mammographic masses: A validation study

Lisa Kinnard
ISIS Center, Georgetown University Medical Center, Washington, DC 20057-1479,
Department of Electrical and Computer Engineering, Howard University, Washington, DC,
and Biomedical NMR Laboratory, Department of Radiology, Howard University, Washington, DC

Shih-Chung B. Lo[a]
ISIS Center, Georgetown University Medical Center, Washington, DC 20057-1479

Erini Makariou
ISIS Center, Georgetown University Medical Center, Washington, DC 20057-1479

Teresa Osicka
ISIS Center, Georgetown University Medical Center, Washington, DC 20057-1479
and Department of Electrical Engineering and Computer Science, The Catholic University of America,
Washington, DC

Paul Wang
Biomedical NMR Laboratory, Department of Radiology, Howard University, Washington, DC

Mohamed F. Chouikha
Department of Electrical and Computer Engineering, Howard University, Washington, DC

Matthew T. Freedman
ISIS Center, Georgetown University Medical Center, Washington, DC 20057-1479

Our purpose in this work was to develop an automatic boundary detection method for mammographic masses and to rigorously test this method via statistical analysis. The segmentation method utilized a steepest change analysis technique for determining the mass boundaries based on a composed probability density cost function. Previous investigators have shown that this function can be utilized to determine the border of the mass body. We have further analyzed this method and have discovered that the steepest changes in this function can produce mass delineations that include extended projections. The method was tested on 124 digitized mammograms selected from the University of South Florida's Digital Database for Screening Mammography (DDSM). The segmentation results were validated using overlap, accuracy, sensitivity, and specificity statistics, where the gold standards were manual traces provided by two expert radiologists. We have concluded that the best intensity threshold corresponds to a particular steepest change location within the composed probability density function. We also found that our results are more closely correlated with one expert than with the second expert. These findings were verified *via* Analysis of Variance (ANOVA) testing. The ANOVA tests obtained *p*-values ranging from $1.03 \times 10^{-2} - 7.51 \times 10^{-17}$ for the single observer studies and $2.03 \times 10^{-2} - 9.43 \times 10^{-4}$ for the two observer studies. Results were categorized using three significance levels, i.e., $p < 0.001$ (extremely significant), $p < 0.01$ (very significant), and $p < 0.05$ (significant), respectively. © *2004 American Association of Physicists in Medicine.* [DOI: 10.1118/1.1781551]

Key words: mass boundary detection, mammography, probability-based cost function

I. INTRODUCTION

In the United States, breast cancer accounts for one-third of all cancer diagnoses among women and it has the second highest mortality rate of all cancer deaths in women.[1] Breast cancer studies are therefore essential for its ultimate eradication. Several studies show that only 13%–29% of suspicious masses are determined to be malignant,[2–4] indicating that there are high false positive rates for biopsied breast masses. A higher predictive rate is anticipated by combining the mammographer's interpretation and the computer analysis.

Other studies show that 7.6%–14% of the patients have mammograms that produce false negative diagnoses.[5,6] Alternatively, a Computer Assisted Diagnosis (CAD_x) system can serve as a clinical tool for the radiologist and consequently lower the rate of missed breast cancer.

Generally, CAD_x systems consist of three major stages, namely, segmentation, feature calculation, and classification. Segmentation is arguably one of the most important aspects of CAD_x—particularly for masses—because a strong diagnostic predictor for masses is shape. Specifically, many ma-

lignant masses have ill-defined, and/or spiculated borders and many benign masses have well-defined, rounded borders. Furthermore, breast masses can have unclear borders and are sometimes obscured by glandular tissue in mammograms. During the search for suspicious areas masses of this type may be overlooked by radiologists. When a specific area is deemed to be suspicious, the radiologist analyzes the overall mass, including its shape and margin characteristics. The margin of a mass is defined as the interface between the mass and surrounding tissue, and is regarded by some as one of the most important factors in determining its significance.[7] Specifically, a spiculated mass consists of a central mass body surrounded by fibrous extensions, hence the resulting stellate shape. In this context, ''extension'' refers to those portions of the mass containing ill-defined borders, spiculations, fibrous borders, and projections. Although the diameters of these cancers are measured across the central portion of the mass, microscopic analysis of the extensions also reveals associated cancer cells, in other words, the extended projections may contain active mass growth.[7,8] In addition, the features of the extended projections and ill-defined borders are highly useful for identifying masses. Hence, proper segmentation—including the body and periphery—is essential for the computer to analyze, and in turn, determine the malignancy of the mass in mammographic CAD_x systems.

Te Brake and Karssemeijer[9] implemented a discrete dynamic contour model, a method similar to snakes, which begins as a set of vertices connected by edges (initial contour) and grows subject to internal and external forces. Li[10] developed a method that employs *k*-means classification to categorize pixels as belonging to the region of interest (ROI) or background. Petrick *et al.*[11] developed the Density Weighted Contrast Enhancement (DWCE) method, in which series of filters are applied to the image in an attempt to extract masses. Pohlman *et al.*[12] developed an adaptive region growing method whose similarity criterion is determined from calculations made in 5×5 windows surrounding the pixel of interest. Mendez *et al.*[13] developed a method, which combined bilateral image subtraction and region growing.

Several studies have also used probability-based analysis to segment digitized mammograms. Li *et al.*[14] developed a segmentation method that first models the histogram of mammograms using a finite generalized Gaussian mixture (FGGM) and then uses a contextual Bayesian relaxation labeling (CBRL) technique to find suspected masses. Furthermore, this method uses the Expectation-Maximization (EM) technique in developing the FGGM model. Comer *et al.*[15] utilized an EM technique to segment digitized mammograms into homogeneous texture regions by assigning each pixel to one of a set of classes such that the number of incorrectly classified pixels was minimized. Kupinski and Giger[16] developed a method, which combines region growing with probability analysis to determine final segmentation. In their method, the probability-based function is formed from a specific composed probability density function, determined by a set of image contours produced by the region growing method. This method is a highly effective one and it was implemented by Te Brake and Karssemeijer in their work[9] that compared the results of a model of the discrete dynamic contour model with those of the probability-based method. For this reason, we chose to investigate its use as a possible starting point from which a second method could be developed. Consequently for our implementation of this work we discovered an important result, i.e., the steepest changes of a cost function composed from two probability density functions of the regions. It appears that in many cases this result produces contour choices that encapsulate important borders such as mass spiculations and ill-defined borders.

Several CAD_x classification techniques have been developed. They are described here to underscore the importance of accurate segmentation in CAD_x studies. Lo *et al.*[17] developed an effective analysis method using the circular path neural network technique that was specifically designed to classify the segmented objects, and it can certainly be extended for the applications related to mass classification. Polakowski *et al.*[18] used a multilayer perceptron (MLP) neural network to distinguish malignant and benign masses. Both Sahiner *et al.*[19] and Rangayyan *et al.*[20] used linear discriminant analysis to distinguish benign masses from malignant masses. While many CAD_x systems have been developed, the development of fully-automated image segmentation algorithms for breast masses has proven to be a daunting task.

II. METHODS

A. Segmentation method—Maximum change of cost function as a continuation of probability-based function analysis

As a point of clarification, the function used to find optimal region growing contours in the Kupinski and Giger study[16] is referred to as the probability-based function and our function is referred to as the cost function. The two functions are similar, however they differ in terms of the images used in their formation. As an initial segmentation step, the region growing is used to aggregate the area of interest,[12,13,21] where grayscale intensity is the similarity criterion. This phase of the algorithm starts with a seed point whose intensity is high, and nearby pixels with values greater than or equal to this value are included in the region of interest. As the intensity threshold decreases, the region increases in size, therefore there is an inverse relationship between intensity value and contour size. In many cases the region growing method is extremely effective in producing contours that are excellent delineations of mammographic masses. However, the computer is not able to choose the contour that is most highly correlated with the experts' delineations, specifically, those masses that contain ill-defined margins or margins that extend into surrounding fibroglandular tissue. Furthermore, the task of asking a radiologist to visually choose the best contour would be both time intensive and extremely subjective from one radiologist to another.

The segmentation technique described in this work attempts to solve and automate this process by adding a two-dimensional (2-D) shadow and probability-based compo-

nents to the segmentation algorithm. Furthermore, we have devised a steepest descent change analysis method that chooses the best contour which delineates the mass body contour as well as its extended borders, i.e., extensions into spiculations and areas in which the borders are ill-defined or obscured. It has been discovered that the probability-based function is capable of extracting the central portion of the mass density as demonstrated by the previous investigators,[16] and in this work the method has been advanced further such that it can include the extensions of the masses. The enhanced method can produce contours, which closely match expert radiologist traces. Specifically, it has been observed that this technique can select the contour that accurately represents the mass body contour for a given set of parameters. However, a further analysis of the cost function composed from the probability density functions inside and outside of a given contour revealed that the computer could choose a set of three segmentation contour choices from the entire set of contour choices, and later make a final decision from these three choices.

1. Region growing and preprocessing

Initially, a 512×512 pixel area surrounding the mass was cropped. The region growing technique[12,13,21] to aggregate the region of interest was employed, where the similarity criterion for our region growing algorithm is grayscale intensity. To start the growth of the first region, a seed point was placed at the center of the 512×512 ROI. The region growing process continues by decreasing the intensity value until we have grown a sufficiently large set of contours.

Next, the image is multiplied by a 2-D trapezoidal membership function with rounded corners whose upper base measures 40 pixels and lower base measures 250 pixels (1 pixel$=50$ microns). This function was chosen because it is a good model of the mammographic mass' intensity distribution. Since the ROI's have been cropped such that the mass' center was located at the center of the 512 pixel $\times 512$ pixel area, shadow multiplication emphasizes pixel values at the center of the ROI and suppresses background pixels. The image to which the shadow has been applied is henceforth referred to as the ''processed'' image. The original image and its processed version were used to compute the highest possibility of its boundaries. The computation method is comprised of two components for a given boundary: (1) formulation of the composed probability as a cost function and (2) evaluation of the cost function.

The contours were grown using the original image as opposed to the processed image, and this choice accounts for a major difference between the current implementation and that of the previous investigators.[16] By using contours generated from the original image, a cost function composed from the probability density functions inside and outside of the contours was produced. In many situations, the greatest changes in contour shape and size occur at sudden decreases within the function. In analyzing these steep changes it was observed that the intensity values corresponding to the steep changes typically produced contours that encapsulated both
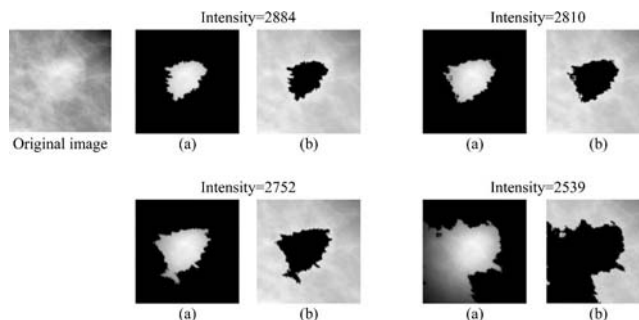

FIG. 1. Four grown contours used to construct the cost function: starts from high intensity thresholds and moves towards low intensity thresholds. Each contour separates the ROI into two parts: (a) Segmented image (based on processed image) used to compute density function $p(f_i(x,y)|S_i)$ and (b) masked image (based on the nonprocessed original image) used to compute density function $p(m_i(x,y)|S_i)$ for four intensity threshold values.

the mass body as well as its spiculated projections or ill-defined margins. This phenomenon would be suppressed if the processed image was used to generate the contour. A more detailed discussion of steep changes within the cost function is forthcoming in Sec. II A 2 C.

The processed image was mainly used to construct the cost function. A common technique used in mass segmentation studies is to pre-process the images using some type of filtering mechanism[11,16] in an effort to separate the mass from surrounding fibroglandular tissue. This method could be particularly beneficial to the region growing process because it would aid in preventing the regions from growing into surrounding tissue. Alternatively, the filtering process could impede our goal of attempting to encapsulate a mass's extended borders as well as borders that are ill-defined due to the filtering process's a tendency to create rounded edges on margins that are actually jagged or spiculated. This phenomenon could potentially defeat the goal of extracting mass borders. For these reasons, we have chosen to aggregate the contours using the original ROI rather its processed version.

2. Formulation of the composed probability as a cost function

In the context of this work, the composed probability is defined as the probability density functions of the pixels inside and outside a contour using a processed and nonprocessed version of an image. Specifically, for a contour (S_i), the composed probability (C_i) is calculated:

$$C_i|S_i = \prod_{j=0}^{h} p(f,(x,y)|S_i) \times \prod_{j=0}^{h} p(m_i(x,y)|S_i). \quad (1)$$

The quantity $f_i(x,y)$ is the set of pixels, which lie inside the contour S_i [see Fig. 1(a)], and this area contained processed pixel values. The quantity $p(f_i(x,y)|S_i)$ is the probability density function of the pixels inside S_i $(f_i(x,y))$, where ''i'' is the intensity threshold used to produce the contours given by the region growing step, and ''h'' is the maximum intensity value. The quantity $m_i(x,y)$ is the set of pixels, which lie outside the contour S_i [see Fig. 1(b)], and this area contained nonprocessed pixels. The quantity $p(m_i(x,y)|S_i)$ is
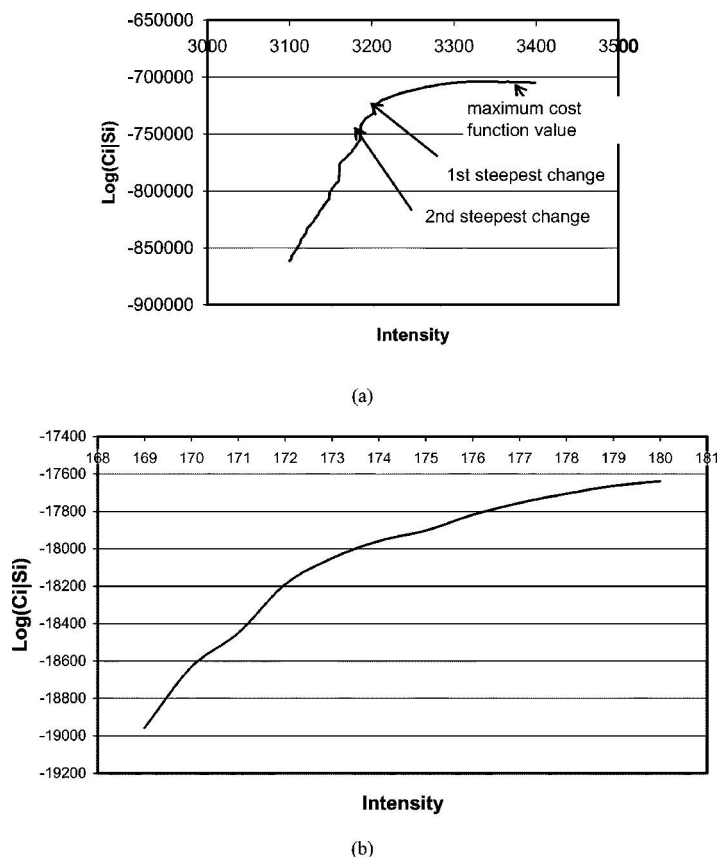
(a)

(b)

FIG. 2. (a) Example of cost function with steepest change location indicators. (b) Example of a probability-based function without an obvious steepest change location.

the probability density function of the pixels outside S_i, where "i" is the intensity threshold used to produce the contours given by the region growing step, and "h" is the maximum intensity value. For implementation purposes, the logarithm of the composed probability of the two regions, C_i was used:

$$\text{Log}(C_i|S_i) = \log\left(\prod_{j=0}^{h} p(f_i(x,y)|S_i)\right)$$
$$+ \log\left(\prod_{j=0}^{h} p(m_i(x,y)|S_i)\right). \quad (2)$$

3. The cost function based on the composed probability density functions

To select the contour that represents the fibrous portion of the mass, it is appropriate to examine the maximum value of the cost function:

$$\arg\max(\text{Log}(C_i|S_i); S_i, i=1,...,n). \quad (3)$$

It has been assessed (also by other investigators[9,16]) that the intensity value corresponding to this maximum value is the optimal intensity needed to delineate the mass body contour. However, in the current implementation it was discovered that the intensity threshold corresponding to the maximum value confines the contour to the fibrous portion of the mass, or, the mass body. In this study many of these contours did not include the extended borders. It is therefore hypothesized that the contour representing the mass extended borders may

well be determined by assessing the greatest changes of the cost function, or locating the steepest value changes within the function

$$\frac{d}{di}(\text{Log}(C_i|S_i); S_i, i=1,...,n). \quad (4)$$

Based on this assumption, cost functions associated with masses were analyzed. The analysis reveals that the most likely boundaries of masses associated with expert radiologist traces are usually produced by the intensity value corresponding to the first or second steepest change of value immediately following the maximum value on the cost function [see Fig. 2(a)]. The description of this discovery is given below. It is followed by a validation study described in Sec. II B and by results shown in Sec. III. The overarching goal of the steep descent method is to determine whether a certain contour is the best contour, and whether it represents the mass and its extended borders.

4. The definition of steepest change

The term "steepest change" is rather subjective. In this work we define it as a location between two or more points in the cost function where the values experience a significant change. When the values are plotted as a function of intensity, these significant changes are often visible in the function. In some cases the cost function increases at a slow rate, therefore a potential steepest change location could be missed. The algorithm design compensates for this issue by

calculating the difference between values in steps over several values and comparing the results to two threshold values. The difference equation is given by

$$d(t) = f(z - wt) - f(z - w(t+1)), \quad t = 0, m, \quad (5)$$

where f is the cost function, z is the maximum intensity, w is the width of the interval over which the cost function differences are calculated (e.g.—for $w = 5$ differences are calculated every 5 points), and m is the total number of points in the searchable area divided by w. Note that "wt" is associated with a specific contour "i" described earlier. If the value of $d(t)$ yields a value greater than or equal to a given threshold, then the intensity corresponding to this location is determined to be a steepest change location. The threshold algorithm occurs as follows:

If $(d(t) \geq TV_1); \quad t = 0, ..., m$

    Then choice 1 = intensity where that condition is satisfied.

If $(d(t) \geq TV_2); \quad t = m, ..., z$

    Then choice 2 = intensity where that condition is satisfied.

where TV_1 and TV_2 are pre-defined threshold values, m is the location in the function where the choice 1 condition is satisfied, and z is the location in the function where the choice 2 condition is satisfied. During the examination of the contour growth with respect to the cost function, the first steepest change $[d(t)_{MC1}$ as choice 1] is determined by TV_1 immediately after the location of the maximum cost function value (corresponding to the mass body discussed earlier). The second the steepest change $[d(t)_{MC2}$ as choice 2] is determined by TV_2 after the first steepest change has been established.

Figure 1(a) illustrates how the algorithm is carried out. In this figure, the maximum value on the cost function occurs for a grayscale intensity value of approximately 3330. The searching process begins from this maximum point and it is discovered that the first steepest change $[d(t)_{MC1}$ as choice 1] occurs for a grayscale intensity value approximately equal to 3200. From this point the searching process continues and it is discovered that the second steepest change $[d(t)_{MC2}$ as choice 2] occurs for a grayscale intensity value approximately equal to 3175. In summary, intensity values of 3330, 3200, and 3175 can be used to grow 3 potential mass delineation candidates, and the large set of intensity choices has been narrowed to 3 choices. The following scenarios occurred when the three contour choices produced by the (1) maximum intensity value on the cost function (2) the intensity corresponding to the first steepest change on the cost function, and (3) the intensity corresponding to the second steepest change on the cost function.

(1) Intensity corresponding to the maximum value on the cost function: The central body of the mass was encapsulated.

(2) Intensity corresponding to the first steepest change on the cost function: The central body of the mass + some of its extended borders (i.e., projections and spiculations) was encapsulated.

(3) Intensity corresponding to the second steepest change on the cost function: The central body of the mass + more extended borders + surrounding fibroglandular tissue was encapsulated.

The intensity corresponding to the first steepest change provides the best choice, and an examination of this observation is shown and discussed in Secs. III and IV of this work.

As stated previously, the steep changes within the cost function would be suppressed if the processed image was used to generate the contour; therefore, the function would be relatively smooth. Figure 2(b), which shows a probability-based function produced by contours that were grown using a processed ROI, demonstrates this issue.

B. Validation method

In several segmentation studies the results were validated using the overlap statistic alone, however, it was necessary to analyze the performance of the steepest change algorithm on the basis of four statistics to verify that the algorithm is indeed capable of categorizing mass and background pixels correctly. This type of analysis provides helpful information regarding necessary changes for the algorithm's design and can possibly aid in its optimization.

The segmentation method was validated on the basis of overlap, accuracy, sensitivity, and specificity.[22,23] These statistics are calculated as follows:

$$\text{Overlap} = \frac{N_{TP}}{N_{FN} + N_{TP} + N_{FP}}, \quad (6)$$

$$\text{Accuracy} = \frac{N_{TP} + N_{TN}}{N_{TP} + N_{TN} + N_{FP} + N_{FN}}, \quad (7)$$

$$\text{Sensitivity} = \frac{N_{TP}}{N_{TP} + N_{FN}}, \quad (8)$$

$$\text{Specificity} = \frac{N_{TN}}{N_{TN} + N_{FP}}, \quad (9)$$

where N_{TP} is the true positive fraction (part of the image correctly classified as mass), N_{TN} true negative fraction (part of the image correctly classified as surrounding tissue), N_{FP}

TABLE I. Distribution of DDSM masses studied according to their subtlety ratings.

Subtlety category	Cancer	Benign
Number of masses with a rating = 1	5	3
Number of masses with a rating = 2	12	12
Number of masses with a rating = 3	18	17
Number of masses with a rating = 4	9	23
Number of masses with a rating = 5	15	10

Fig. 3. (a) Segmentation results for a malignant mass with spiculated margins (subtlety = 2) (b) the corresponding cost function.
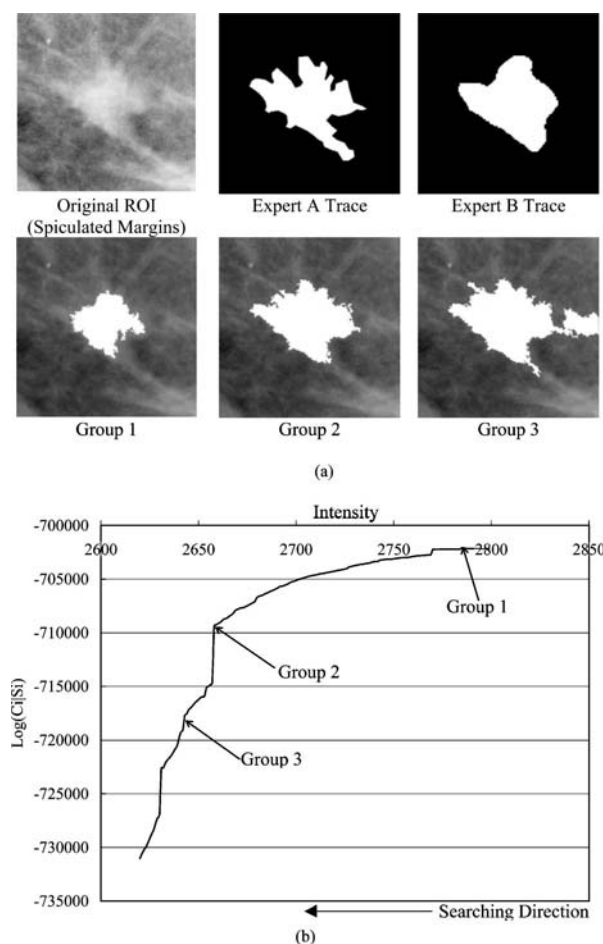

Fig. 4. (a) Segmentation results for a malignant mass with ill-defined margins (subtlety = 3); (b) the corresponding cost function.

is the false positive fraction (part of the image incorrectly classified as mass), and N_{FN} is the false negative fraction (part of the image incorrectly classified as surrounding tissue). This method requires a gold standard, or, a contour to which the segmentation results can be compared. The gold standards for the experiments performed in this work were mass contours, which have been traced by expert radiologists.

The experiments produced contours for the intensity values resulting from three locations within the cost functions: (1) The intensity of the maximum value within the cost function; (2) the intensity for which the cost function experiences its first steepest change; and (3) the intensity for which the cost function experiences its second steepest change. It has been observed that the intensity for which the cost function experiences its first steepest change produces the contour trace that is most highly correlated with the gold standard traces, regarding overlap and accuracy. In cases for which better results occur at the second steepest change location, there is no significant difference between these results and the results calculated for the first steepest change location. Second, it has been observed that the results are more closely correlated with one expert than with the second expert. The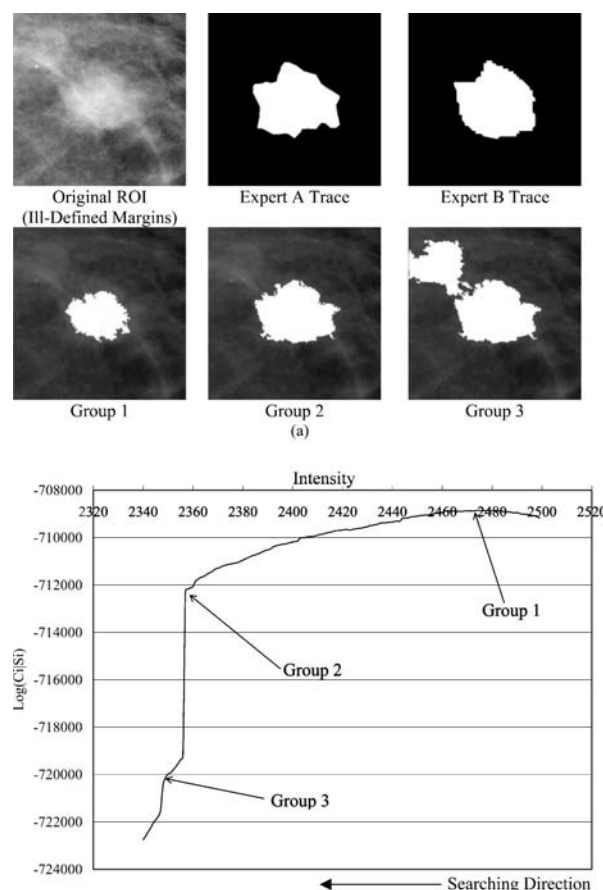se hypotheses were tested using the one-way Analysis of Variance (ANOVA) test.[24,25] In this study, three significance levels (i.e., $p < 0.001$, $p < 0.01$, and $p < 0.05$) were used to categorize the ANOVA results as described in the next section.

III. EXPERIMENTS AND RESULTS

The following sections describe the database and experiments, and provide segmentation results and ANOVA test results.

A. Database

For this study, a total of 124 masses were chosen from the University of South Florida's Digital Database for Screening Mammography (DDSM).[26] The DDSM films were digitized at 43.5 or 50 μm's using either the Howtek or Lumisys digitizers, respectively. The DDSM cases have been ranked by expert radiologists on a scale from 1 to 5, where 1 represents the most subtle masses and 5 represents the most obvious masses. Table I lists the distribution of the masses studied according to their subtlety ratings. The images were of varying contrasts and the masses were of varying sizes.
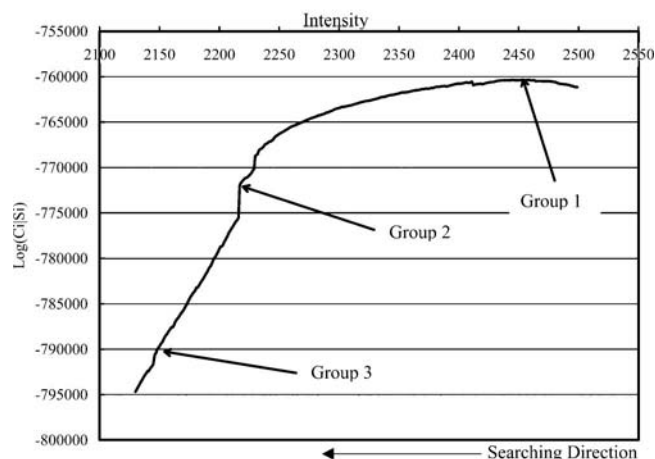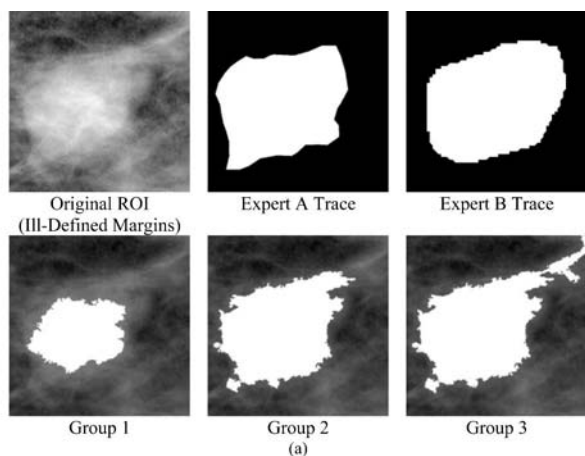
FIG. 5. (a) Segmentation results for a benign mass with ill-defined margins (subtlety=3); (b) the corresponding cost function.

FIG. 6. (a) Segmentation results for a benign mass with circumscribed margins (subtlety=4); (b) the corresponding cost function.

The first set of expert traces was provided by an attending physician at Georgetown University Medical Center (GUMC), and is hereafter referred to as the Expert A traces. The second set of expert traces was provided by the DDSM, and is hereafter referred to as the Expert B traces.

B. Experiments

As mentioned previously, the term "steepest change" is very subjective. Therefore, a set of thresholds needed to be set in an effort to define a particular location within the cost function as a "steepest change location." For this study the following thresholds were experimentally chosen: $TV_1 = 1800$, $TV_2 = 1300$, where TV_1 equals the threshold for steepest change location 1 for the cost function, and TV_2 equals the threshold for steepest change location 2 for the cost function. A number of experiments were performed in an effort to prove that (1) the intensity for which the cost function experiences the first steepest change location produces the contour trace, which is most highly correlated with the gold standard traces with regard to overlap and accuracy. In cases for which the second steepest change location achieves better results, there are no significant differences between the values obtained from the first steepest change
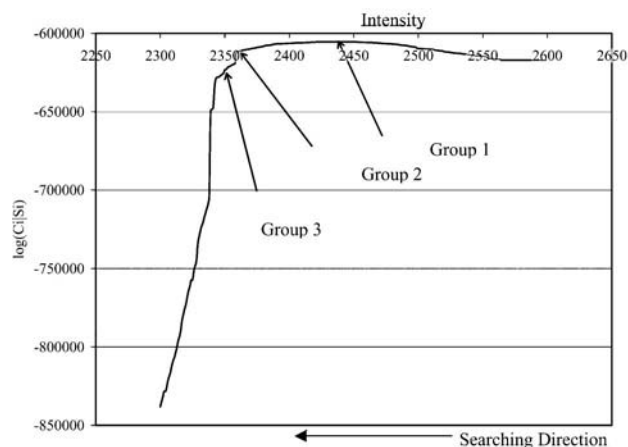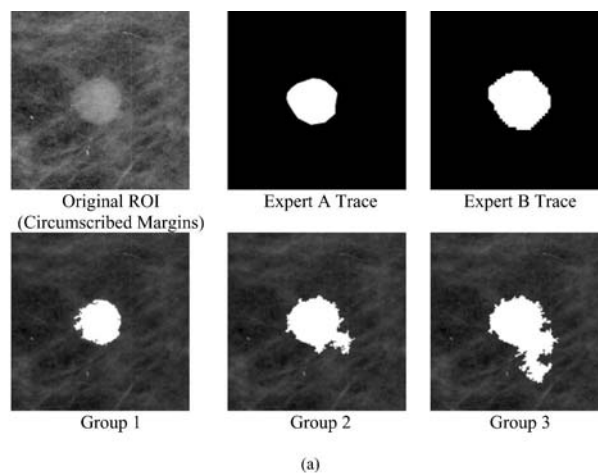
location and the second steepest change location. The experiments linked with these hypotheses comprise the studies for a single observer. We have also set out to prove that (2) our results are more closely correlated with one expert than with the second expert. The experiments linked with this hypothesis comprise the studies between two observers. First segmentation results for two malignant cases are presented, followed by segmentation results for two benign cases. Second, the ANOVA results for a set of hypotheses are presented. The contours produced by the maximum value as well as by the steepest change locations within the cost functions are labeled as follows: (1) group 1: The intensity for which a value within the cost function is maximum; (2) group 2: The intensity for which the cost function experiences its first steepest change; (3) group 3: The intensity for which the cost function experiences its second steepest change.

C. Results

Figures 3–6 display the results for two malignant cases accompanied by their cost functions as well as results for two be--nign cases accompanied by their cost functions. The ANOVA results appear in a set of tables (Secs. II–IV), where each table lists the hypothesis tested along with *p*-values and their corresponding categorizations. The *p*-values are catego-

rized in the following way: not significant (NS for $p > 0.05$), significant (S for $p < 0.05$), very significant (VS for $p < 0.01$), and extremely significant (ES for $p < 0.001$). Each p-value table is followed by a second table, which contains the mean values of overlap, accuracy, sensitivity, and specificity for each group. Sections II and III are identical regarding the experiments, however, the pathologies of the masses are different (Sec. II—malignant masses, Sec. III—benign masses). Although the experiments are identical they have been separated for clarity purposes.

A larger set of segmentation results has been placed in an image gallery containing 7 malignant mass results (Fig. 7) and 7) benign mass results (Fig. 8). These figures are located in the Appendix.

1. Segmentation results

2. ANOVA test results for comparison of contour groups with single observer: Malignant cases

TABLE II. Single observer results (expert A gold standard, malignant masses).

ANOVA test	P-value (group 1 vs group 2)	P-value (group 2 vs group 3)	P-value (group 1 vs group 3)
Difference between groups (overlap)	1.78×10^{-4} (ES)	2.91×10^{-2} (S)	NS
Difference between groups (accuracy)	NS	3.14×10^{-2} (S)	NS
Difference between groups (sensitivity)	1.88×10^{-9} (ES)	NS	1.85×10^{-13} (ES)
Difference between groups (specificity)	5.12×10^{-4} (ES)	2.40×10^{-3} (VS)	2.71×10^{-9} (ES)

TABLE III. Mean values for overlap, accuracy, sensitivity, and specificity (expert A gold standard, malignant masses).

Measurement	Mean value (group 1)	Mean value (group 2)	Mean value (group 3)
Overlap	0.47	0.60	0.53
Accuracy	0.88	0.90	0.87
Sensitivity	0.49	0.75	0.81
Specificity	0.99	0.94	0.88

TABLE IV. Single observer results (expert B gold standard, malignant masses).

ANOVA test	P-value (group 1 vs group 2)	P-value (group 2 vs group 3)	P-value (group 1 vs group 3)
Difference between groups (overlap)	3.96×10^{-6} (ES)	NS	1.58×10^{-4}
Difference between groups (accuracy)	NS	NS	NS
Difference between groups (sensitivity)	4.88×10^{-8} (ES)	4.31×10^{-2} (S)	4.25×10^{-12} (ES)
Difference between groups (specificity)	2.70×10^{-4} (ES)	4.36×10^{-4} (ES)	1.44×10^{-7} (ES)

TABLE V. Mean values for overlap, accuracy, sensitivity, and specificity (expert B gold standard, malignant masses).

Measurement	Mean value (group 1)	Mean value (group 2)	Mean value (group 3)
Overlap	0.38	0.54	0.51
Accuracy	0.83	0.86	0.84
Sensitivity	0.38	0.56	0.60
Specificity	1.00	0.98	0.94

3. ANOVA test results for comparison of contour groups with single observer: Benign cases

TABLE VI. Single observer results (expert A gold standard, benign masses).

ANOVA test	P-value (group 1 vs group 2)	P-value (group 2 vs group 3)	P-value (group 1 vs group 3)
Difference between groups (overlap)	3.19×10^{-4} (ES)	8.38×10^{-4} (ES)	NS
Difference between groups (accuracy)	NS	4.73×10^{-3} (VS)	2.51×10^{-3} (VS)
Difference between groups (sensitivity)	1.14×10^{-9} (ES)	1.89×10^{-2} (S)	7.51×10^{-17} (ES)
Difference between groups (specificity)	8.93×10^{-3} (VS)	1.24×10^{-3} (VS)	3.32×10^{-10} (ES)

TABLE VII. Mean values for overlap, accuracy, sensitivity, and specificity (expert A gold standard, benign masses).

Measurement	Mean value (group 1)	Mean value (group 2)	Mean value (group 3)
Overlap	0.46	0.58	0.45
Accuracy	0.90	0.91	0.85
Sensitivity	0.49	0.73	0.82
Specificity	0.99	0.94	0.86

TABLE VIII. Single observer results (expert B gold standard, benign masses).

ANOVA test	P-value (group 1 vs group 2)	P-value (group 2 vs group 3)	P-value (group 1 vs group 3)
Difference between groups (overlap)	8.82×10^{-5} (ES)	NS	1.62×10^{-2} (S)
Difference between groups (accuracy)	NS	2.62×10^{-2} (S)	2.48×10^{-2} (S)
Difference between groups (sensitivity)	1.61×10^{-7} (ES)	NS	3.14×10^{-12} (ES)
Difference between groups (specificity)	1.18×10^{-2} (S)	1.27×10^{-2} (S)	1.25×10^{-7} (ES)

TABLE IX. Mean values for overlap, accuracy, sensitivity, and specificity (expert B gold standard, benign masses).

Measurement	Mean value (group 1)	Mean value (group 2)	Mean value (group 3)
Overlap	0.36	0.51	0.44
Accuracy	0.88	0.89	0.83
Sensitivity	0.36	0.61	0.69
Specificity	0.99	0.94	0.86

4. ANOVA test results for comparison of contour groups between two observers

TABLE X. Two observer results: expert A vs expert B, malignant masses.

ANOVA test	P-value (group 1 vs group 2)	P-value (group 2 vs group 3)	P-value (group 1 vs group 3)
Expert A vs expert B (overlap)	3.12×10^{-3} (VS)	3.32×10^{-2} (S)	NS
Expert A vs expert B (accuracy)	1.20×10^{-2} (S)	4.46×10^{-2} (S)	NS
Expert A vs expert B (sensitivity)	9.43×10^{-4} (ES)	3.38×10^{-4} (ES)	3.67×10^{-4} (ES)
Expert A vs expert B (specificity)	NS	NS	NS

TABLE XI. Mean values for overlap, accuracy, sensitivity, and specificity (expert A vs expert B, malignant masses).

Measurement	Mean value, expert A (group 1)	Mean value, expert B (group 1)	Mean value, expert A (group 2)	Mean value, expert B (group 2)	Mean value, expert A (group 3)	Mean value, expert B (group 3)
Overlap	0.49	0.38	0.62	0.55	0.55	0.51
Accuracy	0.89	0.83	0.91	0.87	0.87	0.84
Sensitivity	0.52	0.38	0.75	0.60	0.82	0.68
Specificity	0.99	1.00	0.95	0.97	0.89	0.91

TABLE XII. Two observer results: expert A vs expert B, benign masses.

ANOVA test	P-value (group 1 vs group 2)	P-value (group 2 vs group 3)	P-value (group 1 vs group 3)
Expert A vs expert B (overlap)	NS	NS	NS
Expert A vs expert B (accuracy)	NS	NS	NS
Expert A vs expert B (sensitivity)	3.56×10^{-2} (S)	4.90×10^{-2} (S)	2.03×10^{-2} (S)
Expert A vs expert B (specificity)	NS	NS	NS

TABLE XIII. Mean values for overlap, accuracy, sensitivity, and specificity: expert A vs expert B, benign masses.

Measurement	Mean value, expert A (group 1)	Mean value, expert B (group 1)	Mean value, expert A (group 2)	Mean value, expert B (group 2)	Mean value, expert A (group 3)	Mean value, expert B (group 3)
Overlap	0.42	0.35	0.57	0.50	0.48	0.44
Accuracy	0.90	0.88	0.91	0.89	0.85	0.83
Sensitivity	0.44	0.36	0.71	0.61	0.79	0.69
Specificity	0.99	0.99	0.94	0.94	0.86	0.86

IV. DISCUSSION

A. Segmentation results

The ROI's shown in Figs. 3 and 4 demonstrate that the intensity produced by the maximum value is capable of accurately delineating the mass body contour, and in some cases this intensity corresponding to the maximum value produces a contour, which falls inside the mass body contour. This situation can be problematic because low segmentation sensitivities can produce large errors during the feature calculation and classification phases of CAD_x. Of the three available segmentation choices for each mass, it appears that the first steepest change location produces the contours with the strongest correlation in comparison to both gold standards. These contours appear to cover both the mass body contour as well as the extended borders. In some instances the region grows into some areas that are not declared as mass areas by the gold standards—we call this flooding—and fails to grow into other areas that have been declared as mass areas. Finally, the second steepest change location produces contours that also cover both the mass body contour as well as the extended borders, and, these contours tend to also include surrounding fibroglandular tissue; hence, the flooding phenomenon is a common occurrence. In the cases shown, it is clear that steepest change location 1 produces the best contours, in comparison to the gold standards, however, the ANOVA test results allow us to make such a claim. The following discussion is divided into five sections: single observer malignant results, single observer benign results, and two observer results (malignant and benign), algorithm performance, and an additional discussion on methods.

B. Malignant cases with single observer

For both the expert A and expert B gold standards, Tables II–V show a statistically significant difference between groups 1 and 2 on the basis of overlap and sensitivity, where the mean values of group 2 were higher than the mean values of group 1 for these statistics. These results are expected because as shown in the figures, the group 2 contours consistently covered more of the mass area (and correctly covered this mass area) as compared to the group 1 contours, according to both experts. There was a statistically significant difference in sensitivity between group 1 and group 3, where the mean of group 3 was higher than the mean of group 1. This difference is an expected result because out of all the groups, group 3 contours consistently covered the most mass area. For the expert B gold standard there was a statistically significant difference in overlap between group 1 and group 3, where the mean of group 3 was higher than the mean of group 1. This difference is also an expected result because, out of all the groups, the group 3 contours covered the most mass area correctly.

C. Benign cases with single observer

For the expert A traces there were statistically significant differences between the group 2 and group 3 traces on the basis of overlap, accuracy, and sensitivity, where the group 2 mean values for overlap and accuracy were higher than those of group 3 (see Tables VI–IX). This difference is an expected result because it is likely that many of the group 3 contours contained flooded areas, which cause both of these values to be lower than those values of contours without flooded areas. The overlap and sensitivity values for group 2 were significantly higher than those of group 1. This difference is also an expected result because the group 2 contours not only covered more mass area but also covered this area correctly. Finally, the group 3 accuracy and sensitivity values were significantly higher than those for group 1. Again this difference is an expected result because the group 3 contours not only covered more mass area but they also covered this area correctly.

For the expert B gold standard there were statistically significant differences between the group 2 and group 3 traces on the basis of accuracy and sensitivity, where the group 2 mean values for overlap and accuracy were higher than those of group 3. This difference is an expected result because it is likely that many of the group 3 contours contained flooded areas, which cause both of these values to be lower than contours without flooded areas. There were statistically significant differences between group 1 and group 2 on the basis of overlap and sensitivity, where the mean values for group 2 were higher than the mean values for group 1. This is an expected result because the group 2 contours not only covered more mass area but they also covered this area correctly. There were statistically significant differences between group 3 and group 1 on the basis of overlap and sensitivity, where the mean values for group 3 were higher than those of group 1. Again this difference is an expected result because the group 3 contours not only covered more mass area but they covered this area correctly.

In nearly all cases for the single observer studies, it was expected that the specificity values for group 1 would always be higher than those for groups 2 and 3 because this contour always covered the smallest mass area; consequently its background was always highly correlated with the background areas dictated by the gold standards. Moreover, in some cases the group 2 and group 3 contours grew into areas that were not regarded as mass, but rather were regarded as background; therefore, their specificity values had a lower correlation with the gold standard as compared to the group 1 contours.

D. Malignant and benign cases with two observers

For the two observer studies, comparisons were made between experts A and B on a group-by-group basis in an effort to prove that there were significant differences between the two radiologists on the basis of overlap, accuracy, sensitivity, and specificity (see Tables X–XIII). For the malignant masses, there were statistically significant differences between the two experts on the basis of overlap, accuracy, and sensitivity. There was a statistically significant difference between the two experts for group 3 on the basis of sensitivity. For the benign masses, there were statistically significant differences between the two experts for all three groups on the

basis of sensitivity. For all cases, expert A's values were consistently higher than those of expert B. These statistically significant differences between the experts were expected due to their differences in opinion. The fact that expert A's mean values were higher than those for expert B, however, does not warrant the conclusion that expert A is a more reliable expert; however, it does warrant the conclusion that there is stronger agreement between the computer's results and expert A's traces. Furthermore, there were less statistically significant differences for the benign cases than for the malignant cases. This result is expected because, in general, benign masses have better defined borders, and thus the two experts were more likely to agree.

E. Algorithm performance

Apparently the chosen thresholds produce first steepest change location intensities that generate contours closely correlated with the expert traces. In some instances the second steepest change location is extremely far from the first steepest change location, which implies that the function in question increases very slowly; moreover, many of the second steepest change location intensities produce contours with flooded areas. For the majority of the cases in which the second steepest change location contour achieves a higher sensitivity value, but not a significantly higher sensitivity value, we can still choose the first steepest change location contour because the difference between the two contours is likely to be negligible.

In analyzing the probability-based cost functions, we found that those functions with very steep changes are typically associated with masses that have well-defined borders while those functions that increase slowly are associated with masses that have ill-defined borders. This phenomenon may make it necessary to develop an adaptive threshold process for the steepest change evaluation such that the functions are grouped into various categories (e.g., smooth versus steep), because a threshold value that is optimal for a steep function may not be optimal for a smooth function.

F. Additional discussion on methods used

In this study the steepest descent method appears to have the advantage of locating ill-defined margins as well as extensions such as malignant spiculations and projections for mammographic masses. If solely the human eye is used, it can be difficult to separate the mass from the surrounding fibroglandular tissue. Therefore, this method has the potential to complement the process of reading mammographic films. One of the downfalls of the method is its dependence upon the assumption that masses are generally light in color. This assumption impedes the region growing process because masses that contain darker areas and are surrounded on one or more sides by bright tissue can cause contours to flood into areas that are not actual mass tissue. Typically, this situation occurs for the mass located on the border of the breast region on a mammogram.

All of the segmentation methods surveyed in the introduction of this paper are excellent solutions for the problems their authors set out to solve, however, in some cases it is difficult to make comparisons between different methods without the availability of a set of several visual results. In some studies, the focus was either to detect masses or to distinguish malignant from benign masses. Thus, the validation process did not take the form of a comparison with expert radiologist manual traces; but rather, features were calculated on the potential mass candidates and they were later classified as being mass tissue or normal tissue.[10–13] The purpose of Li's study[14] was to distinguish between normal and abnormal tissue; thus the authors did not provide any statistics such as overlap or accuracy. Nevertheless, the study contains a figure of 60 masses that contain both computer and radiologist annotations to give the reader an idea of the computer algorithm's performance. Te Brake and Karssemeijer's study[9] used the overlap statistic to test the efficacy of their method. They indicated that the central mass area was delineated by the radiologist and their computer results were compared to these annotations. The Kupinski and Giger study[16] also used the overlap statistic to test the efficacy of their method and set a threshold for which the mass was considered to be successfully segmented. For example, masses whose overlap values are greater than 0.7 imply that there was successful segmentation.

The technical method presented herein shows that the results obtained from the maximization of the composed probability density function (i.e., the cost function) are equivalent to those obtained from previous methods presented by previous investigators. However, the steepest change of the composed probability density function is the closest to radiologists' determinations.

V. CONCLUSION

We have shown that our fully automatic boundary detection method for malignant and benign masses can effectively delineate these masses using intensities, that correspond to the first steepest change location within their cost functions. Additionally, the method appears to be more highly correlated with one set of expert traces than with a second set of expert traces, regarding the accuracy and overlap statistics. This result shows that inter-observer variability can be an important factor in segmentation algorithm design, and it has motivated us to seek the opinions of more expert radiologists to test the robustness of our algorithm. The second steepest change location intensity will always yield contours with higher sensitivity values, however, it behooves us to choose the first steepest change location intensity because it avoids the risk of choosing contours that contain substantial flooding. In future work, a worthwhile study would run the experiments for different threshold values in an effort to discover the possibility of deriving an optimal threshold procedure. We believe that such a procedure would improve the method of choosing optimal contours.

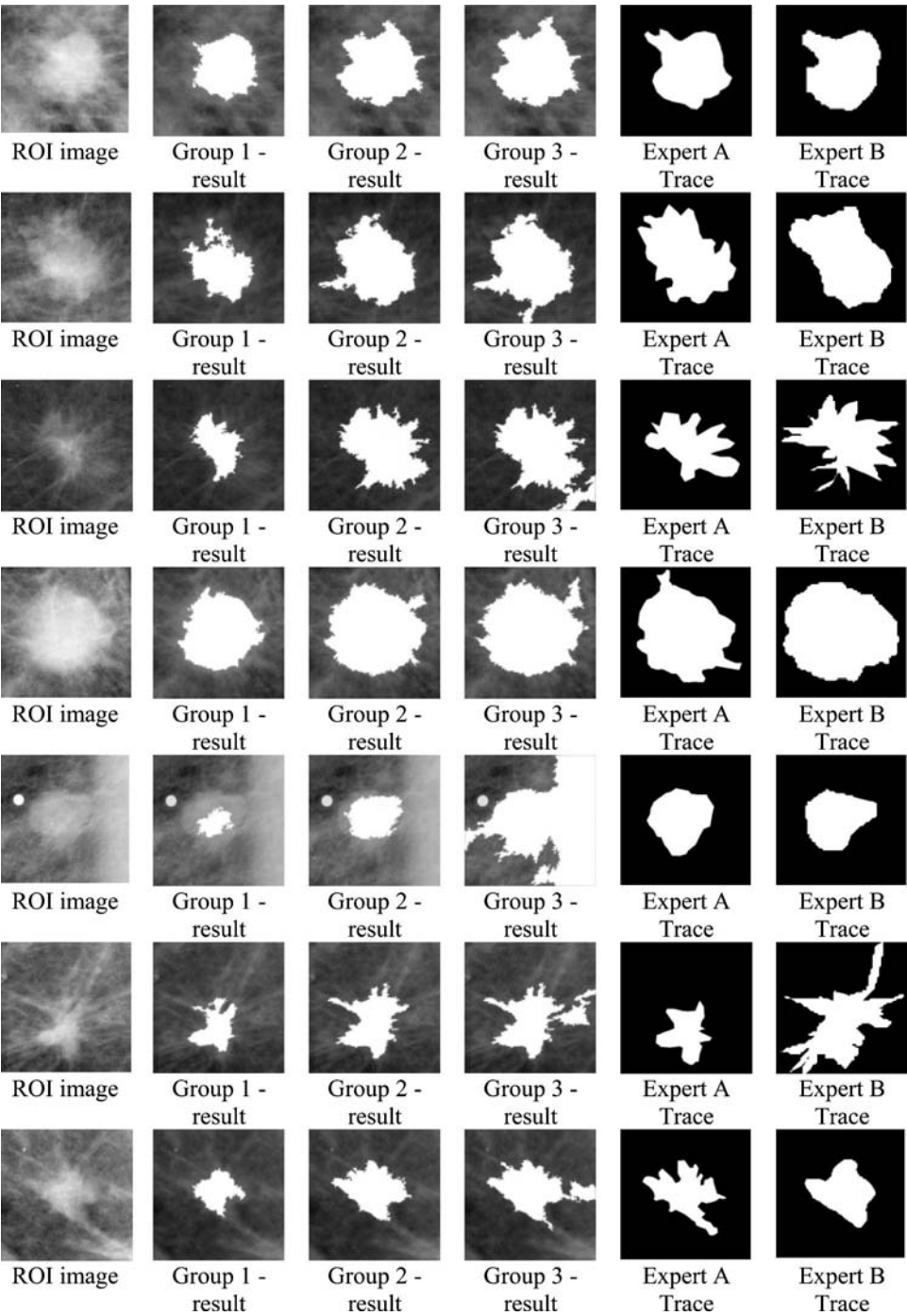## ACKNOWLEDGMENTS

APPENDIX A—GALLERY OF SEGMENTATION RESULTS

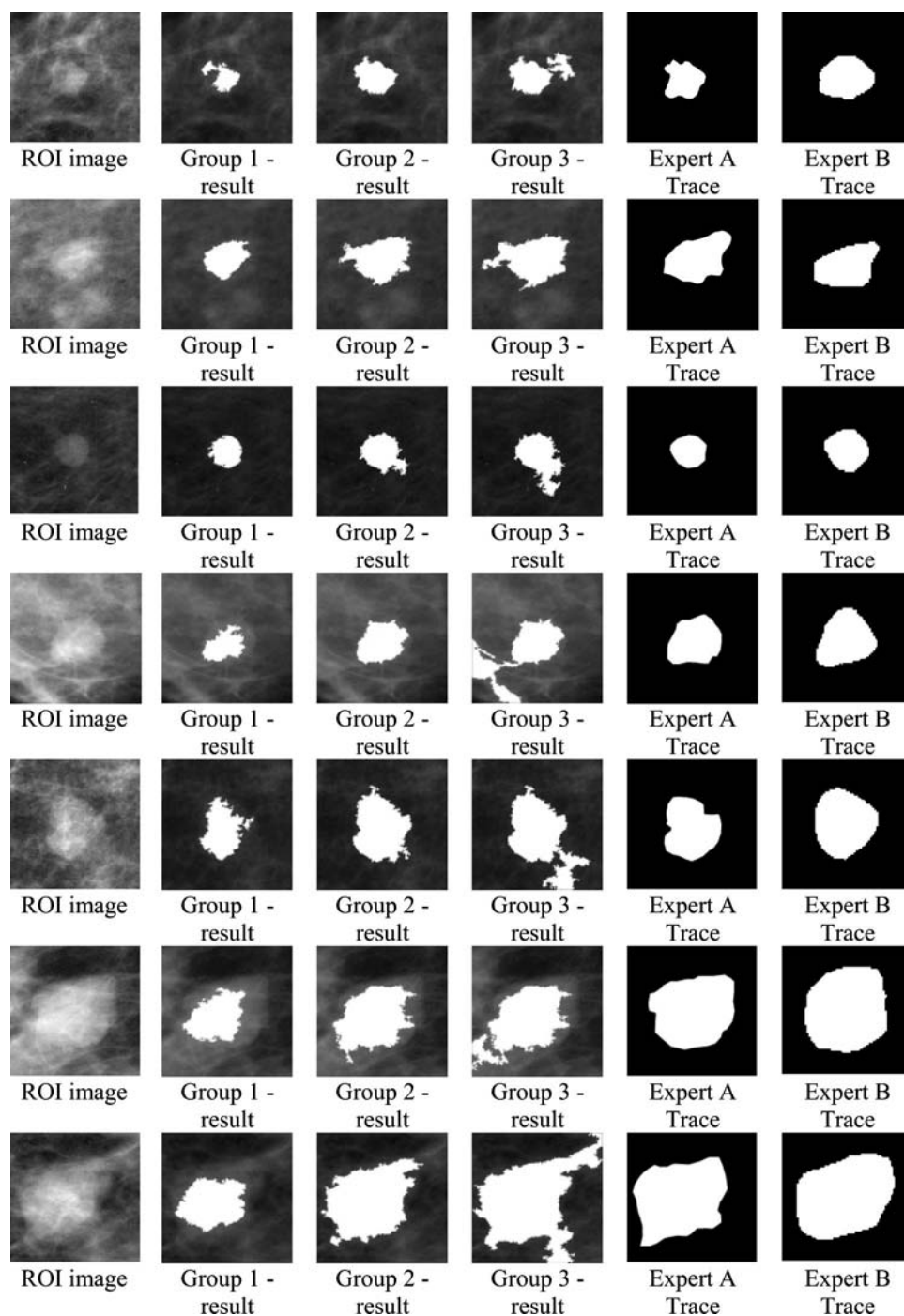
FIG. 7. Segmentation results for a set of malignant masses.

FIG. 8. Segmentation results for a set of benign masses.

a)Author to whom correspondence should be addressed. Dr. Shih-Chung B. Lo, ISIS Center, Department of Radiology, Georgetown University, Box 571479, Washington, DC 20057-1479. Electronic mail: lo@isis.imac.georgetown.edu

[1] J. V. Lacey, Jr., S. S. Devesa, and L. A. Brinton, "Recent trends in breast cancer incidence and mortality," Environ. Mol. Mutagen. **39**, 82–88 (2002).

[2] J. E. Meyer, D. B. Kopans, P. C. Stomper, and K. K. Lindfors, "Occult breast abnormalities: percutaneous preoperative needle localization," Radiology **150**, 335–337 (1984).

[3] A. L. Rosenberg, G. F. Schwartz, S. A. Feig, and A. S. Patchefsky, "Clinically occult breast lesions: localization and significance," Radiology **162**, 167–170 (1987).

[4] B. C. Yankaskas, M. H. Knelson, M. L. Abernethy, J. T. Cuttino, and R. L. Clark, "Needle localization biopsy of occult lesions of the breast," Radiology **23**, 729–733 (1988).

[5] J. A. Harvey, L. L. Fajardo, and C. A. Innis, "Previous mammograms in patients with impalpable breast carcinoma: retrospective vs. blinded interpretation," Am. J. Roentgenol., Radium Ther. Nucl. Med. **161**, 1167–1172 (1993).

[6] J. E. Martin, M. Moskowitz, and J. R. Milbrath, "Breast cancer missed by mammography," Am. J. Roentgenol., Radium Ther. Nucl. Med. **132**, 737–739 (1979).

[7] J. R. Harris, M. E. Lippman, M. Morrow, and S. Hellman, *Diseases of the Breast* (Lippincott-Raven Publishers, Philadelphia, 1996), pp. 80–81.

[8] J. E. Martin, *Atlas of Mammography: Histologic and Mammographic Correlations*, 2nd ed. (Williams and Wilkins, Baltimore, 1988), p. 87.

[9] G. M. te Brake and N. Karssemeijer, "Segmentation of suspicious den-

sities in digital mammograms,'' Med. Phys. **28**, 259–266 (2001).

[10] L. Li, Y. Zheng, L. Zhang, and R. Clark, "False-positive reduction in CAD mass detection using a competitive classification strategy," Med. Phys. **28**, 250–258 (2001).

[11] N. Petrick, H.-P. Chan, B. Sahiner, and D. Wei, "An adaptive density-weighted contrast enhancement filter for mammographic breast mass detection," IEEE Trans. Med. Imaging **15**, 59–67 (1996).

[12] S. Pohlman, K. A. Powell, N. A. Obuchowski, W. A. Chilcote, and S. Grundfest-Broniatowski, "Quantitative classification of breast tumors in digitized mammograms," Med. Phys. **23**, 1337–1345 (1996).

[13] A. J. Méndez, P. G. Tahoces, M. J. Lado, M. Souto, and J. J. Vidal, "Computer-aided diagnosis: Automatic detection of malignant masses in digitized mammograms," Med. Phys. **25**, 957–964 (1998).

[14] H. Li, Y. Wang, K. J. R. Liu, S.-C. B. Lo, and M. T. Freedman, "Computerized radiographic mass detection—part I: lesion site selection by morphological enhancement and contextual segmentation," IEEE Trans. Med. Imaging **20**, 289–301 (2001).

[15] M. L. Comer, S. Liu, and E. J. Delp, "Statistical segmentation of mammograms," *Digital Mammography '96*: proceedings of the 3rd international workshop on digital mammography, Chicago, IL, pp. 475–478, 9–12 June 1996.

[16] M. A. Kupinski and M. L. Giger, "Automated seeded lesion segmentation on digital mammograms," IEEE Trans. Med. Imaging **17**, 510–517 (1998).

[17] S.-C. B. Lo, H. Li, Y. Wang, L. Kinnard, and M. T. Freedman, "A multiple circular path convolution neural network system for detection of mammographic masses," IEEE Trans. Med. Imaging **21**, 150–158 (2002).

[18] W. E. Polakowski, D. A. Cournoyer, S. K. Rogers, M. P. DeSimio, D. W. Ruck, J. W. Hoffmeister, and R. A. Raines, "Computer-aided breast cancer detection and diagnosis of masses using difference of Gaussians and derivative-based feature saliency," IEEE Trans. Med. Imaging **16**, 811–819 (1997).

[19] B. Sahiner, H.-P. Chan, N. Petrick, M. A. Helvie, and L. M. Hadjiiski, "Improvement of mammographic mass characterization using spiculation measures and morphological features," Med. Phys. **28**, 1455–1465 (2001).

[20] R. M. Rangayyan, N. M. El-Faramawy, J. E. Leo Desautels, and O. A. Alim, "Measures of acutance and shape for classification of breast tumors," IEEE Trans. Med. Imaging **16**, 799–810 (1997).

[21] B. Sahiner, H.-P. Chan, D. Wei, N. Petrick, M. A. Helvie, D. D. Adler, and M. M. Goodsit, "Image feature selection by a genetic algorithm: Application to classification of mass and normal breast tissue," Med. Phys. **23**, 1671–1684 (1996).

[22] J. Suckling, D. R. Dance, E. Moskovic, D. J. Lewis, and S. G. Blacker, "Segmentation of mammograms using multiple linked self-organizing neural networks," Med. Phys. **22**, 145–152 (1995).

[23] B. Van Ginneken, "Automatic segmentation of lung fields in chest radiographs," Med. Phys. **27**, 2445–2455 (2000).

[24] D. Downing and J. Clark, *Statistics the Easy Way*, 2nd ed. (Barron's Educational Series, Hauppauge, 1989), pp. 184–206.

[25] W. Hopkins, *A New View of Statistics: P Values and Statistical Significance*; available online at www.sportsci.org/resource/stats/pvalues.html.

[26] M. Heath *et al.*, "Current status of the digital database for screening mammography," *Digital Mammography* (Kluwer Academic, New York, 1998), pp. 457–460.

A Tumor-Targeted Nanodelivery System to Improve Early MRI Detection of Cancer

Kathleen F. Pirollo[1], John Dagata[2], Paul Wang[3], Matthew Freedman[1], Andras Vladar[2], Stanley Fricke[1], Lilia Ileva[1], Qi Zhou[1], and Esther H. Chang[1]

[1]Georgetown University Medical Center, [2]National Institute of Standards and Technology, and [3]Howard University

Abstract

The development of improvements in magnetic resonance imaging (MRI) that would enhance sensitivity, leading to earlier detection of cancer and visualization of metastatic disease, is an area of intense exploration. We have devised a tumor-targeting, liposomal nanodelivery platform for use in gene medicine. This systemically administered nanocomplex has been shown to specifically and efficiently deliver both genes and oligonucleotides to primary and metastatic tumor cells, resulting in significant tumor growth inhibition and even tumor regression. Here we examine the effect on MRI of incorporating conventional MRI contrast agent Magnevist® into our anti-transferrin receptor single-chain antibody (TfRscFv) liposomal complex. Both in vitro and in an in vivo orthotopic mouse model of pancreatic cancer, we show increased resolution and image intensity with the complexed Magnevist®. Using advanced microscopy techniques (scanning electron microscopy and scanning probe microscopy), we also established that the Magnevist® is in fact encapsulated by the liposome in the complex and that the complex still retains its nanodimensional size. These results demonstrate that this TfRscFv–liposome–Magnevist® nanocomplex has the potential to become a useful tool in early cancer detection. *Mol Imaging* (2006) **5**, 41–52.

Keywords: Nanocomplex, tumor targeting, Magnevist®, MRI, early detection.

Introduction

The ability to detect cancer, both primary and metastatic disease, at an early stage would be a major step toward the goal of ending the pain and suffering from the disease. The development of tumor-targeted delivery systems for gene therapy has opened the potential for delivery of imaging agents more effectively than is currently achievable. Magnetic resonance imaging (MRI) can acquire 3-D anatomical images of organs. Coupling these with paramagnetic images results in the accurate localization of tumors as well as longitudinal and quantitative monitoring of tumor growth and angiogenesis [1,2].

One of the most common paramagnetic imaging agents used in cancer diagnostics is Magnevist® (gadopentetate dimeglumine). Gadolinium is a rare earth element. It shows paramagnetic properties because its ion (Gd^{2+}) has seven unpaired electrons. The contrast enhancement observed in MRI scans is due to the strong effect of Gd^{2+} primarily on the hydrogen-proton spin–lattice relaxation time (T1). Whereas free gadolinium is highly toxic and thus unsuitable for clinical use, chelation with diethylenetriamine pentacetic acid generates a well-tolerated, stable, strongly paramagnetic complex. This metal chelate is metabolically inert. However, after intravenous (iv) injection of gadopentetate dimeglumine, the meglumine ion dissociates from the hydrophobic gadopentetate, which is distributed only in the extracellular water. It cannot cross an intact blood–brain barrier and therefore does not accumulate in normal brain tissue, cysts, postoperative scars, etc, and it is rapidly excreted in the urine. It has a mean half-life of about 1.6 hr. Approximately 80% of the dose is excreted in the urine within 6 hr.

A systemically administered tumor-targeting delivery system has been developed in our laboratory for use in gene medicine [3–8]. This nanosized complex is composed of a cationic liposome encapsulating the nucleic acid payload, which can be either genes [3–6] or oligonucleotides [7,8]. Decorating the surface of the liposome is a targeting molecule that can be a ligand, such as folate or transferrin, or an antibody or an antibody fragment directed against a cell surface receptor. The presence of the ligand/antibody on the liposome facilitates the entry of the complex into the cells through binding of the targeting molecule by its receptor followed by internalization of the bound complex via receptor-mediated endocytosis, a highly efficient

internalization pathway [9,10]. This modification of the liposomes results in their being able to not only selectively deliver their payload to tumor cells, but also increases the transfection efficacy of the liposome. Transferrin receptor (TfR) levels are elevated in various types of cancer including oral, prostate, breast, and pancreas [11–16]. Moreover, the TfR recycles during internalization in rapidly developing cells such as cancer cells [16], thus contributing to the uptake of these transferrin-targeted nanocomplexes even in cancer cells where TfR levels are not elevated. The nanocomplex used in the studies described here uses an anti-transferrin receptor single-chain antibody fragment (TfRscFv) as the targeting moiety [17,18]. TfRscFv contains the complete antibody-binding site for the epitope of the TfR recognized by the monoclonal antibody 5E9 [18]. TfRscFv has advantages over the transferrin molecule itself, or an entire monoclonal antibody, in targeting liposomes to cancer cells with elevated TfR levels: (1) The size of the scFv (28 kDa) is much smaller than that of the transferrin molecule (80 kDa) or the parental monoclonal antibody (155 kDa). The scFv liposome–DNA complex may thus exhibit better penetration into small capillaries characteristic of solid tumors. (2) The smaller scFv has a practical advantage related to the scaled-up production necessary for the clinical trials. (3) The scFv is a recombinant molecule and not a blood product like transferrin and thus presents no danger of a potential contamination by blood-borne pathogens. (4) Without the Fc region of the monoclonal antibody, the issue of non-antigen-specific binding through Fc receptors is eliminated [19]. Most importantly, we have already shown that such an anti-TfR single-chain antibody molecule can target an intravenously administered cationic liposome–DNA nanocomplex preferentially to tumors [5,6]. Encapsulating Magnevist® within such a tumor-targeted nanocomplex offers potential advantages for enhanced sensitivity, detection of metastases, and diagnosis of cancer.

In this article, using a mouse xenograft model of human pancreatic cancer, we explore the use of this nanocomplex for systemic delivery of the imaging agent Magnevist® to tumors. In addition, we used scanning electron microscopy (SEM) and scanning probe microscopy (SPM) [20–25] to examine the physical structure and size of these Magnevist®-carrying nanocomplexes. Because gadolinium is a high-atomic-number element and possesses a large magnetic moment, these properties can be exploited in a variety of ways to enhance contrast in both SEM and SPM. The findings presented below demonstrate that our ligand–liposome nanocomplex does indeed encapsulate Magnevist® and that iv administration of this complex results in enhanced tumor imaging.

Materials and Methods

Cell Lines

Human lymphoblastic leukemia cell line K562 was obtained from the Lombardi Comprehensive Cancer Center Tissue Culture core facility (Washington, DC). These suspension cells were maintained in RPMI 1640 supplemented with 10% heat-inactivated fetal bovine serum (FBS) plus 2 mM L-glutamine, and 50 μg/mL each of penicillin, streptomycin, and neomycin. Human pancreatic cancer cell line CaPan-1 (obtained from ATCC, Manassas, VA) was derived from a metastatic adenocarcinoma of the pancreas. It was maintained in Iscove's modified Dulbecco's medium containing 4 mM L-glutamine and sodium bicarbonate, supplemented with 20% non-heat-inactivated FBS, 2 mM L-glutamine, and 50 μg/mL each of penicillin, streptomycin, and neomycin. Human prostate cancer cell line DU145 (ATCC) was originally derived from a lesion in the brain of a patient with widespread metastatic carcinoma of the prostate. It was maintained in minimum essential medium with Earle's salts supplemented with 10% heat-inactivated FBS plus L-glutamine and antibiotics as above.

Nanocomplex Formation

Cationic liposome (DOTAP:DOPE) was prepared by the ethanol injection method as previously described [6]. When delivering plasmid DNA, the full complex was formed in a manner identical to that previously described [26]. To encapsulate the imaging agent, the TfRscFv was mixed with the liposome at a specific ratio (identical to that used with DNA) and incubated at room temperature for 10 min. Magnevist® was added to this solution, mixed, and again incubated at room temperature for 10 min. When stored at 2–8°C the complex is stable for at least 8 days, as determined by size measurements using a Malvern Zetasizer 3000H (Malvern, UK). The average of the cumulants (Z average) measurements over this time frame is 112.3 ± 4.67 (SE), whereas the polydispersity (representing the reproducibility of the values during repeat scans) is 0.445 ± 0.03. For in vitro transfection, 2 mL of serum-free medium was added to the complex before transfection. When prepared for in vivo use, dextrose was added to a final concentration of 5%. For both in vitro and in vivo complex formation, the ratio of Magnevist® to liposome was 1:7 (vol/vol).

In Vitro Transfection

To transfect suspension cells K562, 15×10^6 cells in a total volume of 4.0 mL of medium with all supplements except serum (serum-free medium) were placed into a 100-mm^2 tissue-culture dish. Two milliliters of the transfection solution from above, containing varying amounts of Magnevist®, was added to the cell suspension. The plate was incubated at 37°C with gentle rocking for the length of time given in the Results section (up to 90 min), after which the cells were gently pelleted ($600 \times g$ for 7 min) at 4°C in 0.5 mL microcentrifuge tubes and washed three times with 10 mL of serum free medium to remove any excess transfection solution and placed on wet ice until imaged.

In Vivo Tumor Targeting

To assess the tumor-selective targeting of the TfRscFv–liposome (TfRscFv–Lip) nanocomplex to primary and metastatic tumors, an orthotopic metastasis model using human pancreatic cancer cell line CaPan-1 was used. Subcutaneous xenograft tumors of CaPan-1 were induced in female athymic nude mice by injection of 1×10^7 CaPan-1 cells suspended in Matrigel collagen basement membrane matrix (BD Biosciences, San Jose, CA). Approximately 8 weeks later, the tumors were harvested and a single-cell suspension of the tumor was prepared. Cells ($1.2–1.5 \times 10^7$), also suspended in Matrigel were injected into the surgically exposed pancreas of female athymic nude mice as previously described [27]. Five weeks post surgery, the complex carrying the *LacZ* gene was iv injected $3\times$ over 24 hrs (at 40 μg DNA per injection). Sixty hours later, the animals were sacrificed and examined for the presence of metastases and organs stained for β-galactosidase expression using a previously described procedure [3].

Magnetic Resonance Imaging

For in vitro MRI, the cell pellets in microcentrifuge tubes were positioned at the center of the magnet. The MRI was performed at Howard University using a 4.7-T horizontal bore NMR machine (Varian Inc, Palo Alto, CA). The imaging protocols consist of a multislice T1-weighted spin–echo imaging sequence and a saturation–recovery sequence. For the T1-weighted imaging technique, the repetition time (TR) was 1000 msec and the echo time (TE) was 13 msec. The T1-weighted spin–echo imaging technique was applied to verify the positive image enhancement. The saturation–recovery MR sequence with variable echo times was used for the T1 measurement. The slice thickness of images was 0.5 mm. The radiofrequency (RF) coil used was a 30-mm single-

loop coil. The RF coil serves as an RF transmitter and receiver. The RF pulse was a selective 5-msec sinc pulse. The number of phase-encoding steps was 256. The field of view was 15×15 mm. The image area chosen in the study was at the center of the RF coil for RF homogeneity. The MR images were taken in the cross-section direction of the microcentrifuge tube. The height of the cell pellet was 12 mm. The range of the multislice images covers the whole pellet. The center slice images, which were not influenced by the image distortion due to the susceptibility effect from the air–pellet boundary, were used for the studies. The image intensity was measured using the Varian Image Browser software. The signal is taken from a region of interest that is big enough to cover two thirds of the image from each microcentrifuge tube. The relative image intensities of the pellets from these tubes were applied for contrast enhancement evaluation and the T1 measurements.

For the in vivo studies, mice bearing CaPan-1 orthotopic tumors or DU145 subcutaneous xenograft tumors were used. The CaPan-1 tumors were induced as described above. DU145 tumors were induced by the subcutaneous inoculation of 7×10^6 cells in Matrigel. These studies were performed at Georgetown University. Animals to be imaged were anesthetized and placed in a proprietary, in-house designed, animal management system. This system incorporates a warm-water heating system that maintains the temperature at 37°C, as well as a four-channel, thermal optical monitoring system used to monitor animals' skin temperature, ambient temperature, and wall temperature of the device. For imaging, anesthesia was induced using isoflurane at 4%, with the remaining gas composed of a 66% oxygen and 30% nitrous oxide mixture. Maintenance of anesthesia was achieved with 1.5% isoflurane under similar gaseous conditions of oxygen and nitrous oxide as noted. The anesthetized animal was positioned inside a cylindrical, variable RF resonant antenna (birdcage resonator volume coil) and tuned to a center frequency of approximately 300 MHz (the resonant frequency of water molecules when subject to a field strength of 7 T). The imaging protocol used was T1-weighted Turbo-RARE (rapid acquisition with rapid enhancement) 3-D imaging sequences performed on a 7T Bruker BioSpin (Billerica, MA) imaging console. The imaging parameters used were as follows: T1-weighted Turbo-RARE 3-D, TE 13.3 msec, TR 229.5 sec, flipback on, four echoes with a field of view of 8.0/3.5/3.5 cm and a $256 \times 256 \times 256$ matrix. After a baseline image was acquired, the animal was kept immobilized in the animal holder and the Magnevist® only [diluted to 400 μL with 1× phosphate-

buffered saline (pH = 7.4)] or the TfRscFv–Lip–Mag complex (total volume 400 µL) was systemically administered using a 27 G needle by iv injection into the tail vein of the animal and the 3-D imaging sequence was immediately initiated. The imaging with the two solutions were performed on sequential days.

Scanning Electron Microscopy

Sample solutions of liposome-encapsulated Magnevist contrast agent and complete nanocomplex consisting of a tumor-targeting single-chain transferrin receptor protein coating the liposome-encapsulated complex, TfRscFv–Lip–Mag, were prepared at Georgetown University Medical Center (GUMC), delivered to National Institute of Standards and Technology (NIST) and were stored under dark and refrigeration. For each imaging session, a fresh dilution 1:3 by volume with deionized water was prepared and a 5-µL droplet was micropipetted onto a standard 200-mesh transmission electron microscopy grid consisting of 30–60 nm formvar and 15–20 nm carbon. The droplet was allowed to dry on the grid in air for 5 min before being loaded into the vacuum chamber of the microscope. Imaging was performed using a Hitachi S-4800 field-emission microscope at NIST. Of particular interest to applications of SEM to nanocomplex imaging is a comparison of upper and lower secondary electron detectors [SE9(U) and SE(L)]—using the SEM in its usual mode—to the addition of a transmitted electron (TE) detector, transforming the instrument into a low-voltage STEM.

Scanning Probe Microscopy

Sample solutions of liposome-encapsulated Magnevist contrast agent and complete nanocomplex were prepared at GUMC, delivered to NIST, and were stored under dark and refrigeration. For each imaging session, a fresh dilution 1:3 by volume with deionized water was prepared and a 5-µL droplet was micropipetted onto an untrasonically cleaned silicon substrate used with native oxide or with a poly-L-lysine coating. SPM imaging were obtained using a Veeco (Santa Barbara, CA) MultiMode microscope with a Nanoscope IV controller. Topography by tapping mode with Z control [Veeco RTESP cantilevers, of approximately 320–360 kHz and k approximately 20–60 N/m], phase imaging, and magnetic force microscopy using magnetic-coated tips (Veeco MESP 68 kHz] were performed in life mode. Dynamic imaging of dewetting and surface energy "phase separation" as the solution evaporates to expose isolated nanoparticles and aggregates were used to understand the consequences of solvent drying on the stability of the particles

and its effect on the various SPM contrast mechanisms available with the SPM system.

Results

Tumor-Specific Targeting by the Ligand–Liposome Nanocomplex Carrying a Reporter Gene

To assess selective targeting of the TfRscFv–LipA nanocomplex to primary tumor and metastases, an orthotopic metastasis model, a closer approximation of the clinical situation, using human PanCa cell line CaPan-1 was used. Surgical orthotopic implantations of CaPan-1 xenograft tumor sections into nude mice have been shown to produce, within 56 days, metastases in liver and spleen [27]. Orthotopic tumors of CaPan-1 were induced in female athymic nude mice as described in Materials and Methods. Approximately 5 weeks later, the animals were euthanized and necropsied to look for tumor in the pancreas and other organs. As shown in Figure 1A, extensive tumor growth is evident throughout the pancreas. Metastases were present in various organs in four of five mice including the spleen, liver, lung, adrenal gland and even within the diaphragm. This experiment was repeated with similar results.

To establish selective targeting tumor and metastasis, before sacrificing the mice, the TfRscFv–LipA complex carrying pSVb (LacZ) plasmid DNA for β-galactosidase expression was iv injected into the mice three times over a 24-hr period (40 µg of plasmid DNA per injection). All five mice were sacrificed 60 hr after injection and various organs, including the liver, lung, spleen, pancreas and
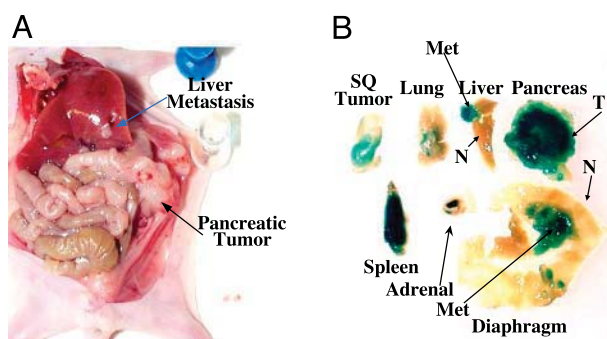

Figure 1. *Tumor-specific targeting of a CaPan-1 orthotopic metastasis model by the TfRscFv–Lip–DNA nanocomplex. Subcutaneous CaPan-1 xenograft tumors were induced in female athymic nude mice as described in Materials and Methods. The tumors were harvested and a single-cell suspension in Matrigel was injected into the surgically exposed pancreas. Five weeks post injection, the TfRscFv–Lip complex carrying the LacZ gene for β-galactosidase expression (40 µg) was iv injected 3× over 24 hr. Sixty hours later, the animals were sacrificed and examined for the presence of metastases and the organs stained for β-galactosidase expression. The same tumor nodule in the liver indicated by an arrow in A exhibits intense β-galactosidase expression in B. (A) Gross necropsy; (B) tissues after staining for β-galactosidase.*

diaphragm, were harvested and examined for the presence of metastasis and tumor-specific staining. Fresh samples, sliced at 1-mm thickness, were stained with X-gal to produce a blue color where the gene is expressed. The tumor-targeting ability and high transfection efficiency of the complex is demonstrated by the presence of the reporter gene in the various organs from this animal (Figure 1B). In the liver, lung, adrenal gland, and diaphragm, it is clearly shown that the reporter gene is highly expressed only in the metastases, whereas in the adjacent normal tissue, no blue color is evident. The metastasis visible in the liver in Figure 1A (arrow) is the same tumor nodule strongly expressing β-galactosidase in Figure 1B (arrow) confirming the tumor-specific nature of this nanocomplex. In some of the mice, growth of the tumor in pancreas also resulted in extrusion of tumor through the original incision site used for implantation. In Figure 1B, this strongly blue stained subcutaneous tumor, surrounded by normal nonstained skin, is also shown, again showing tumor cell specificity. Similar results were observed in the rest of the mice and in the repeat experiment. Thus, this systemically administrated nanocomplex will target tumor cells, both primary and metastatic, wherever they occur in the body, and efficiently deliver plasmid DNA. We wished to expand the potential of this delivery system to include contrast agents. The ability to do so could result in improved imaging and cancer detection.

In Vitro Studies Using TfRscFv–Lip Complex to Deliver Magnevist®

As Magnevist® is one of the most frequently used contrast agents in the clinic, it was chosen for use in these studies. In our initial experiments, we examined whether the complex could be prepared with Magnevist® and if doing so would enhance the MRI signal. Because trypsinization could lead to membrane damage and leakage of contrast agent from the cells, adherent cells were not used in these studies. Instead, a human lymphoblastic leukemia cell line, K562, which grows as a suspension culture was used. Moreover, gentle pelleting and washing of the cells would remove any excess Magnevist® or complex before imaging, allowing only cell-associated signal to be detected.

Time-Dependent Image Enhancement by the TfRscFv–Lip–Mag Nanocomplex

We examined the optimal time for transfection of the TfRscFv–Lip–Mag nanocomplex. The suggested clinical dose of Magnevist is 0.1 mmol/kg. In these initial studies, we used a dose of 0.3 mmol/kg (corrected for the smaller weight and blood volume of mouse vs. man)

in the complex per 250 µL of transfection solution. K562 cells were transfected for times ranging from 20 to 90 min. Twenty minutes showed very low transfection activity based on the image intensity (data not shown). However, as shown in Figure 2A, by 60 min the cells transfected with the complex showed a large increase in intensity as compared to the untreated cells. The intensity of the untreated cells (202 ± 48) was not significantly different from that of an empty marker tube (194 ± 43), indicating that the cells themselves do not contribute to the signal detected. More importantly, the transfection efficiency plateaus at approximately 60 min because the relative intensity of the cells transfected for 60 and 90 min were identical (317 ± 46 and 317 ± 47, respectively).

Magnevist® Dose-Dependent Image Enhancement

Using 60 min as the transfection time, we then assessed the effect of increasing amounts of Magnevist® on the TfRscFv–Lip–Mag complex image enhancement. The doses tested were 0.05, 0.3, and 0.9 mmol/kg. Corrected for size and blood volume of the mouse, the volumes of Magnevist® used in the complex per 250 µL of transfection solution were 0.25, 1.5, and 4.5 µL. As shown in Figure 2B and Table 1, the image intensity increases and the T1 relaxation time shortens as a function of the amount of contrast agent included in the complex.

Image Enhancement by TfRscFv–Lip–Mag as Compared to Free Magnevist®

Based on the above experiments it appears that the TfRscFv–Lip can complex with Magnevist® and deliver it to the cells for image enhancement. To assess the level of enhancement of the complexed contrast agent as compared to the agent alone and demonstrate that the signal obtained is not due to the presence of unincorporated Magnevist®, we treated K562 cells with either free Magnevist® or the TfRscFv–Lip–Mag nanocomplex. The identical amount of contrast agent (0.3 mmole/kg or 1.5 µL/250 µL transfection volume) and transfection time (60 min) was used for both solutions. Whereas free Magnevist® showed enhanced contrast relative to the untreated cells as expected, the cells treated with the TfRscv–Lip–Magnevist complex demonstrated a much greater increase in image intensity and shortened T1 relaxation time compared to both untreated and free-Magnevist®-treated cells (Figure 2C, Table 2). These results not only demonstrate the increased efficiency of contrast agent uptake by means of the targeted nanocomplex, but also indicate that the observed signal is
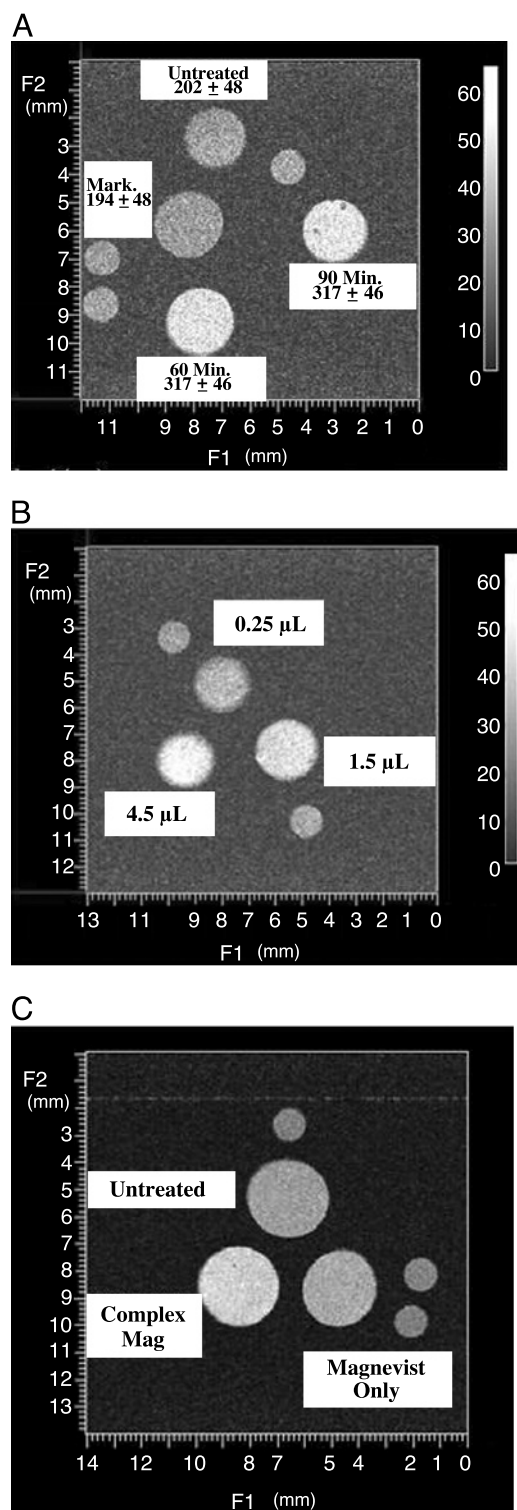
A

B

C

Figure 2. *In vitro MRI of K564 cells after transfection with the TfRscFv–Lip–Mag nanocomplex. After transfection with either free Magnevist® or the noncomplex encapsulating Magnevist® the cells were pelleted and washed with serum-free medium, and MRI performed using a 4.7T Varian NMR. The imaging protocol consisted of T1-weighted spin–echo imaging sequences (TR/TE, 1000/13 msec) to verify the image enhancement and a saturation–recovery MR sequence with variable echo times for the T1 measurement. (A) Time-dependent transfection. The values given are relative intensities. (B) Variation in relative intensity with the amount of Magnevist® included in the complex (in microliters). (C) Comparison of relative intensity of the TfRscFv–Lip–Mag complex versus free Magnevist®. The small circles in all images are markers for sample orientation.*

Table 1. Relative Intensity and T1 Relaxation Time as a Function of Magnevist® in the Complex

Dose of Contrast Agent (mM/kg)	Relative Intensity	T1 (sec)
0.05 (0.25 μL)	293 ± 50	1.43 ± 0.007
0.3 (1.5 μL)	379 ± 43	1.16 ± 0.004
0.9 (4.5 μL)	454 ± 51	1.01 ± 0.004

likely not due to uncomplexed Magnevist®. Further evidence of Magnevist® encapsulation is given below.

In Vivo Image Enhancement with TfRscFv–Lip–Mag

The above studies established that the nanocomplex could more efficiently image tumor cells in vitro than Magnevist® alone. However, to have potential for clinical use, the complex must exhibit a similar effect in vivo. We used the same human pancreatic cancer orthotopic mouse model (CaPan-1) for these studies as was used above to demonstrate tumor-specific targeting of the complex carrying a reporter gene. In addition, a second tumor model, a subcutaneous prostate xenograft mouse model (DU145) was also used. Mice bearing CaPan-1 or DU145 tumors were imaged on a 7T Bruker NMR as described in Materials and Methods. Once positioned in the coil, a baseline image was obtained using a T1-weighted Turbo-RARE 3-D imaging sequence. To facilitate image alignment, after baseline acquisition the animal was maintained in the animal holder while the imaging solution was administered via iv injection. Signal acquisition was begun within 3 min of the injection. The amount of Magnevist® administered to the mouse, either free (as is performed in the clinic) or included in the complex, was 10 μL. This amount is equivalent to 0.2 mmole/kg or twice that used in humans. This amount was selected because the standard human dose of 0.1 mmole/kg Magnevist® alone gave a very poor signal in the mice. The imaging with free Magnevist® and the TfRscFv–Lip–Mag complex were performed on two consecutive days. A baseline scan was also performed before administration of nanocomplex to confirm that all of the Magnevist® from the previous day had been washed out. MR technique and windows were consistent between the two sets of images with the windows

Table 2. Comparison of the Relative Intensity and T1 Relaxation Time between Free and Complexed Magnevist®

Treatment	Relative Intensity	T1 (sec)
Untreated	455 ± 47	1.80 ± 0.009
Free Magnevist®	538 ± 50	1.51 ± 0.007
Complexed Magnevist®	662 ± 52	1.40 ± 0.004

adjusted to correct for an automatic windowing feature of the scanner.

Images of the Magnevist® and nanocomplex–Magnevist in three separate mice are show in Figure 3. In Figure 3A, 4 months after surgical implantation of the CaPan-1 tumor cells, the animal is carrying a large orthotopic tumor. The increased resolution and signal intensity, as compared to the contrast agent alone is quite evident. Similar results are observed in the second mouse with a CaPan-1 tumor shown in Figure 3B. This animal, only 2 months postsurgery, has a visible subcutaneous tumor growing through the site of the incision. A small abdominal mass was also detected by palpation. Not only is the signal in the subcutaneous tumor more enhanced after administration of the complexed Magnevist®, but what appears to be the small orthotopic tumor (arrow) is evident in this scan and not in the one in which the animal received the free Magnevist®. Similarly, increased definition and contrast are evident in the subcutaneous DU145 tumor (Figure 3C) after

injection with the TfRscFv–Lip–Mag complex as compared to the free Magnevist®. Reconstruction and quantitation was performed on the images in Figure 3B and C, representing the two different tumor models, pancreatic cancer (CaPan-1) and prostate cancer (DU145). In both instances, there is an increased intensity (pixels) by the free Magnevist® over the baseline, as expected (Table 3). However, delivery of the imaging agent by the tumor-targeting nanocomplex results in an almost three-fold further increase in signal intensity in both of these tumor models. These studies thus demonstrate that when Magnevist® is incorporated within the TfRscFv–Lip complex there is an improved tumor visualization in an in vivo situation, and they suggest the potential benefit of further developing this means of tumor detection for clinical use.

Physical Characterization Studies

Whereas the in vitro studies offered circumstantial evidence that complexed Magnevist® is encapsulated

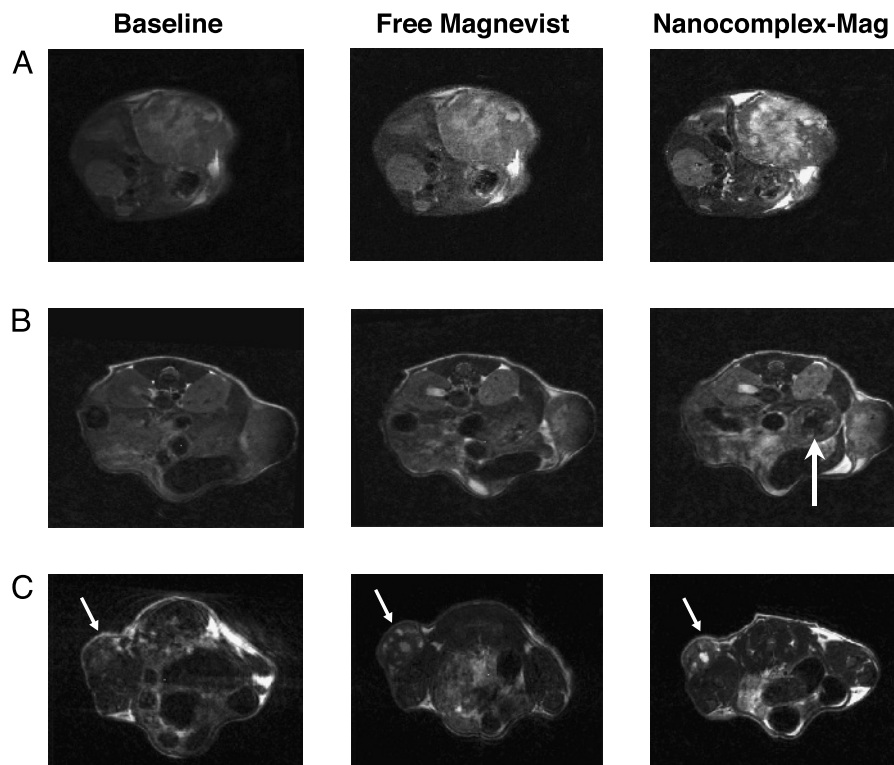| Baseline | Free Magnevist | Nanocomplex-Mag |

Figure 3. *Improved MRI in two different models of cancer using the ligand–liposome–Mag nanocomplex. Human pancreatic cancer cells (CaPan-1) were surgically implanted into the body of the pancreas, and human prostate cancer cells (DU145) were subcutaneously injected on the lower back of female athymic nude mice. Free Magnevist® or the TfRscFv–Lip nanocomplex containing the same dose of Magnevist® was iv injected (via the tail vein) into each of the three mice on two consecutive days. This amount of Magnevist® is equivalent to twice the dose that would be administered to a human patient. The total volume of solution administered in all cases was 400 µL. A baseline scan was performed just before administration of the nanocomplex to confirm that all of the Magnevist® from the previous day had been washed out. MR technique and windows were constant between the three sets of images, with the windows adjusted to correct for an automatic windowing feature of the scanner. (A) Differences in MRI signal in a large pancreatic orthotopic tumor (arrow) (4 months after surgical implantation of the tumor) between the iv-administered free contrast agent and the TfRscFv–Lip–Mag complex. (B) Similar effect in a second mouse with a subcutaneous pancreatic tumor and a much smaller abdominal pancreatic tumor (arrows). (C) Images of a third animal with a subcutaneous prostate tumor (arrow) in which the same effect is evident.*

Table 3. Intensity Increase over Baseline by Free and Complexed Magnevist®

	CaPan-1	DU145
	% Increase over Baseline	
Complexed Magnevist®	99	215
Free Magnevist®	34.5	70

within the liposome, we have used sophisticated microscopy techniques (SEM and SPM) to confirm this fact and further characterize (e.g., complex size) the TfRscFv–Lip–Mag complex.

Imaging of Liposomes without Magnevist. High-resolution imaging implies narrow depth of focus and so requires relatively thin and flat samples. How thin varies with technique, but surface and substrate effects—surface energy and symmetry lowering—often dominate the structural forces typical of biomaterials. This is particularly true for liposomes given their tenuous nature [28]. So an understanding of reliable methods for preparing and characterizing the dimensional and mechanical stability of isolated liposomes is an essential step. The goal of our present characterization efforts is to perform direct sensing of the mechanical stiffness and magnetic properties of nanoparticles to establish that the contrast agent is indeed contained within the nanoparticle and not simply associated externally with the liposomes.

The SPM images surface topography in tapping mode by oscillating the tip and cantilever to which it is attached close to the cantilever resonance frequency. A feedback circuit maintains the oscillation of the cantilever at constant amplitude. This constant amplitude is given by a set point that is somewhat smaller than that of the freely oscillating cantilever. Because the SPM tip interacts with the surface through various small forces, there is a phase shift between the cantilever excitation and its response at a given point on the surface. For an inhomogeneous surface, the tip–surface interactions will vary according to surface charge, steep topographical changes, and mechanical stiffness variations, for example. By changing the set point and observing how certain features respond to softer or harder tapping, we can correlate this with the response expected for a specific structure such as a liposome. (The free oscillation amplitude signal is approximately 1.78 V.) A sequence of SPM phase images of a pair of isolated liposomes without payload is shown in Figure 4. Figure 4A was imaged at a set point of 1.68 V and the corresponding negative phase difference between the substrate and liposome indicates that the tip–sample

interaction is attractive for the liposome, given by a phase value of −3.5°. In the case of an attractive interaction and negative phase, the phase image of the liposome appears dark, except for a topographically keyed ring at the liposome edge. Figure 4B demonstrates the effect of reducing the set point to 1.45 V: The liposome now appears bright because the tip–sample interaction becomes repulsive, and here the phase difference between the liposome and substrate is +8°. Finally, Figure 4C shows that the phase difference recorded at a set point of 1.35 V increases further, becoming +35°.

Imaging of Liposome-Encapsulated Magnevist. Figure 5 presents SPM and SEM images of isolated lipo-
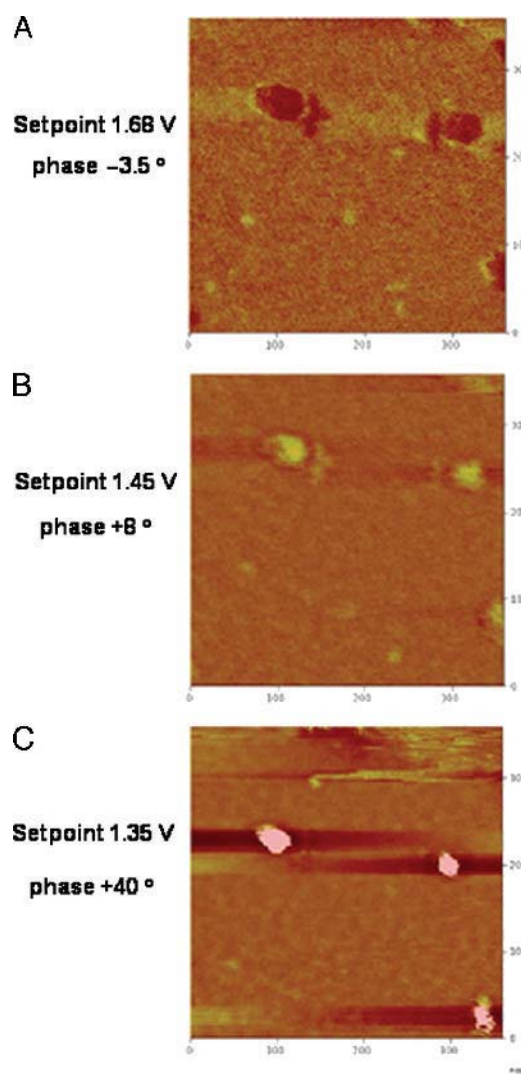

Figure 4. *SPM phase images of liposomes without Magnevist®. The images appearing in A, B, and C were obtained at set points of 1.68, 1.45, and 1.35 V, respectively. The corresponding phase differences between the noncompliant substrate and the mechanically compliant liposome are −3.5°, +8°, and +40°. The interaction of the SPM tip and liposome changes from attractive to repulsive as the set point is decreased.*
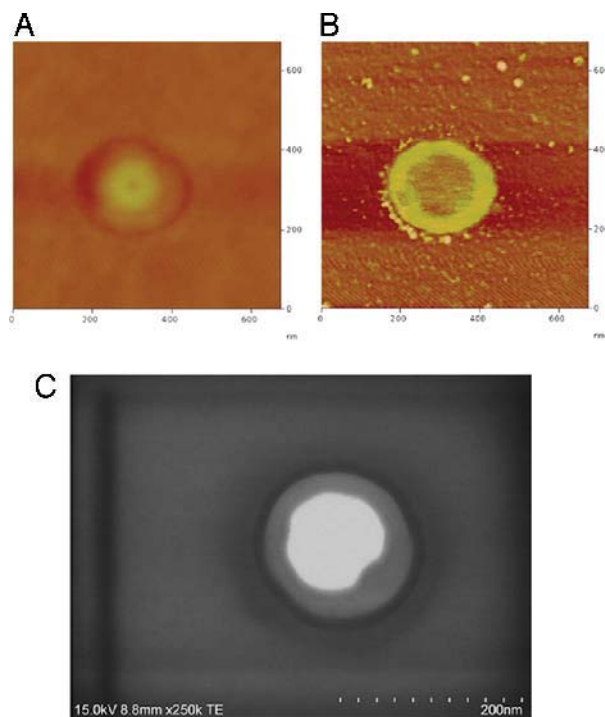
Figure 5. *SPM and SEM images of liposome-encapsulated Magnevist®
(Lip+Mag). (A) Atomic force microscopy topographical image of the lip-
osome-encapsulated Magenvist® particle. The SPM phase image (set point =
1.6) (B) and 15 keV SEM (TE) (transmission-mode electron detector) image (C)
possess similar contrast, although generated by entirely distinct complemen-
tary physical mechanisms.*

some-encapsulated Magnevist (Lip+Mag) nanoparticles.
The size distribution of single (Lip+Mag) particles is in
the diameter range of 100–200 nm and scales according
to optical measurements that indicate that payload-
encapsulating liposomes are approximately 50% larger
than liposomes alone in their spherical state.

The SPM topograph in Figure 5A indicates that lipo-
somes containing Magnevist have a bimodal surface
shape after drying that is more complex than that of
the simple elliptical surface of a liposome containing
no payload (not shown). The SPM phase behavior dif-
fers markedly from that of payloadless liposomes, the
outer ring is repulsive relative to the center, and a corre-
sponding SPM phase image is shown in Figure 5B.
Regions of both attractive and repulsive tip–sample
interaction appear at moderate set point values. A
correlation between the SPM phase image obtained at
a set point of 1.6 and the SEM image in TE mode is
evident in Figure 5B and C. Liposomes appear uniformly
bright across the entire particle in SEM images (not
shown), similar to the uniform phase images we obtain
by SPM. Tips and cantilevers change with time and
usage. Moreover, it is important to verify that the images
produced are not affected by tip instabilities due to

foreign material on the tip. Thus, they are changed
frequently. Because each cantilever is somewhat differ-
ent with respect to its resonance properties, the set
points used in Figures 4 and 5 are different.

Imaging of TfRscFv–Lip–Mag Nanocomplex. The
complete TfRscFv–Lip–Mag nanocomplex was prepared
and imaged by SEM and SPM as described in Materials
and Methods. Results, shown in Figure 6 indicate that
the solvent film undergoes phase separation; however,
examples of isolated NDS can be readily observed on the
dried film. Note that the SEM beam clearly causes some
damage to the film, but the particles can be repeatedly
scanned several times before beam damage becomes
significant. The appearance of the full complex is differ-
ent from that of the (Lip+Mag) only. The shape is less
regular and considerable texturing of the liposome
surface following drying is consistent with protein dena-
turation. Also, SEM TE images indicate that the well-
defined boundary between the outer ring and center of
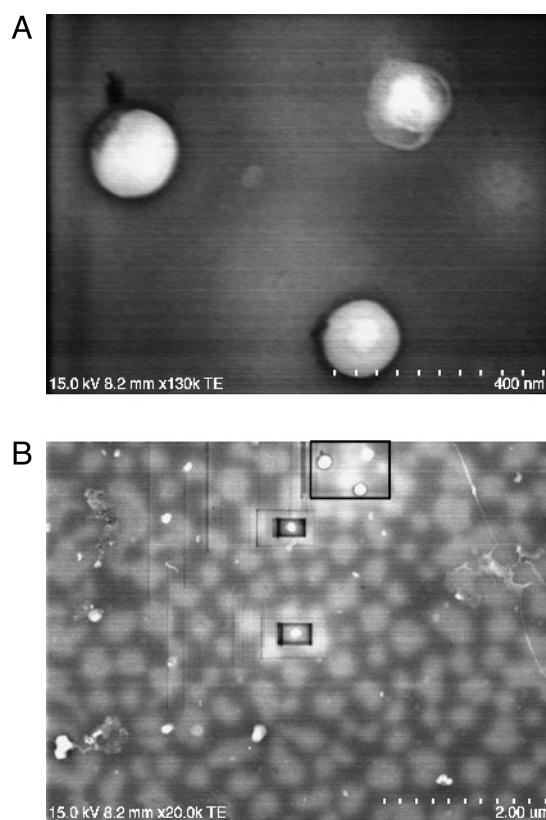the liposome seen with the (Lip+Mag) particles is less

Figure 6. *SPM topographic and phase imaging of TfRscFv–Lip–Mag nano-
complex. (A) 15 keV SEM (TE) (transmission-mode electron detector) image of
the full nanocomplex. A suitable choice of amplitude set point readily
distinguishes intact nanocomplex particles from decomposition products. It
is not known if the decomposed material was present in the solution before
sample preparation or is the direct result of interaction with the substrate. (B)
power image of the field. The boxed area is the image in A.*

apparent and the shape much more variable. This is consistent with the view that the presence of protein within the liposome has altered the osmotic outflow across the liposome during film drying.

It is possible to obtain additional information about these NDS particles by using the magnetic force microscopy imaging capabilities of the SPM (MFM). Because the magnetic moment of gadolinium-containing Magnevist is quite large, it should be possible using a magnetized SPM tip to interact with the oriented Magnevist concentrated within the liposomes. This is shown in Figure 7 for MFM of several approximately 100- to 200-nm-diameter nanocomplexes. We establish that, in fact, we are producing an image that is truly magnetic in nature by using the lift-mode capabilities of the SPM: In this mode, a topographic image under normal tapping

mode conditions is obtained. The reference surface information is then used to offset the tip by a specified height away from the surface and the surface is then scanned at this increased height. This removes the influence of topography on the signal. MFM images obtained in lift mode at a height of 15 nm or more from the surface are given by the magnetic phase image. The appearance of a signal confirms the presence of gadolinium encapsulated within the complex.

Discussion

The development of nanoparticle-sized delivery systems that have greater tumor and tissue penetrance is a major direction in medical research in general and cancer research in particular. Combining the capabilities of these small particles with the ability to home specifically to tumor cells wherever they occur in the body could lead to significant advances in cancer treatment and diagnosis. We have previously shown that our ligand–liposome–DNA complex can specifically target and efficiently transfect tumor cells (primary and metastatic) [3–8]. When encapsulating plasmid DNA, this targeted delivery system is truly a nanocomplex, with a uniform size of less than 100 nm [29]. Used in combination with conventional radiation/chemotherapy, delivery of therapeutic genes such as wild-type p53 by means of this nanodelivery system has resulted in tumor growth inhibition and even tumor regression in animal models [3–5,29]. This tumor regression and concomitant decrease in blood flow due to p53-mediated antiangiogenesis have also been demonstrated using Power Doppler ultrasound imaging [30]. Adapting such a tumor-targeted nanocomplex to deliver imaging agents would have the potential to improve early diagnosis as well as detection of metastatic disease. The results described above demonstrate that we can encapsulate and deliver the commonly used MRI agent Magnevist® to tumor cells both in vitro and in an orthotopic animal model and in doing so produce a more defined and intense image than seen with uncomplexed Magnevist®.

Other nanometer-sized delivery systems for contrast agents are being developed. A chylomicron-remnant-like vehicle of approximately 90 nm containing polyiodinated triglyceride analogs in a neutral lipid core has been developed as a hepatocyte-selective contrast agent for computed tomography in animals [31]. A paramagnetic liquid perfluorocarbon nanoparticle of approximately 250 nm to which an anti-$\alpha_v\beta_3$ antibody has been conjugated is being developed for MRI to assess angiogenesis and atherosclerosis [32,33]. However,
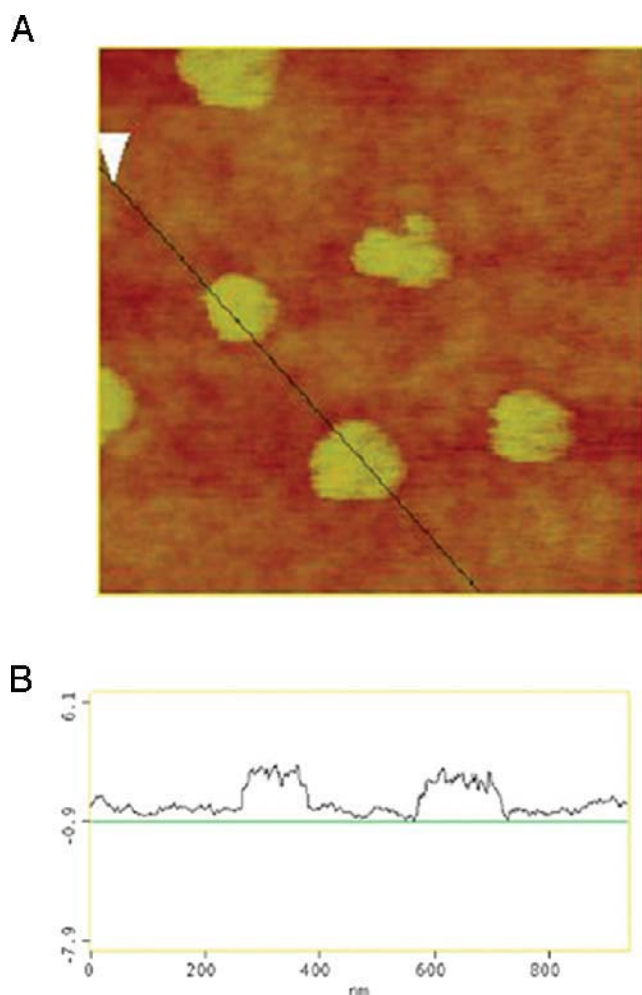

Figure 7. *Cross-sectional comparison of SPM topographic and magnetic phase image in lift mode using 25-nm height displacement. (A) SPM topographic/magnetic phase image of the full TfRscFv–Lip–Mag nanocomplex. The appearance of a double dipole-like signal in B consisting of attractive and repulsive in-plane magnetic interactions suggests that the cause of this interaction is the nonuniform toroidal distribution of Magnevist within the NDS, consistent with SEM and nonmagnetic SPM phase images.*

none of these are tumor targeting or currently applicable for cancer. However, given, as shown in Figure 1, that our nanocomplex can target metastatic disease it is anticipated that use of the nanocomplexed Magnevist® would also enhance detection sensitivity for metastases. The results shown here are with primary tumors. Studies are currently under way to compare the sensitivity of detection between free Magnevist® and the TfRscFv–Lip–Mag complex in metastases.

Using SEM and SPM we have also shown that the TfRscFv–Lip complex maintains its nanometer size when Magnevist® is encapsulated (particles of approximately 100–200 nm are shown in Figures 6 and 7). We have also demonstrated that the structural and mechanical properties of liposomes containing a payload are sufficiently different from those without one for it to be possible to confirm that Magnevist® is indeed encapsulated with the liposome. This was further confirmed by MFM imaging of the complex.

A tentative explanation for the internal structure of (Lip+Mag) is that the slight bulge in the SPM topographic image, represents a liposome-confined phase separation, that is, formation of a dense Magnevist–lipid toroidal distribution around the periphery of the particle with a preferential aqueous phase at the particle's center. This response is probably attributable to several important factors: First, the properties of Magnevist solution are pH approximately 6.5–8, an osmolality of 1,960, and viscosity of 4.9 at 20°C according to the manufacturer. A plausible chemical basis for this separation of the solution noted in the Magnevist data sheet: The meglumine salts dissociate completely from the complex, so changes in the local osmotic conditions. Coupled with the charge interaction of the gadolinium complex and cationic lipid, these interactions may provide a strong driving force for a hypertonic phase separation within the liposome. The charge distribution between the cationic lipid and Magnevist solution is effective at stabilizing the liposome and at providing structural support in solution and apparently in the bloodstream. This enhanced structural support is an important benefit for our studies because it enables most particles to remain intact during the film-drying process, in contrast to the extensive decomposition observed with the liposome-only solutions.

Therefore, we have been able to successfully encapsulate an MR contrast agent in our tumor-targeted nanodelivery system. The image enhancement demonstrated by the complex over conventionally delivered Magnevist® indicates the potential of this system to improve early detection of cancer via MRI.

References

[1] Gillies RJ, Bhujwalla ZM, Evelhoch J, Garwood M, Neeman M, Robinson SP, Sotak CH, Van Der SB (2000). Applications of magnetic resonance in model systems: Tumor biology and physiology. *Neoplasia.* **2:**139–151.

[2] Degani H, Chetrit-Dadiani M, Bogin L, Furman-Haran E (2003). Magnetic resonance imaging of tumor vasculature. *Thromb Haemost.* **89:**25–33.

[3] Xu L, Pirollo K, Tang W, Rait A, Chang EH (1999). Transferrin–liposome-mediated systemic p53 gene therapy in combination with radiation results in regression of human head and neck cancer xenografts. *Hum Gene Ther.* **10:**2941–2952.

[4] Xu L, Pirollo K, Chang EH, Murray A (1999). Systemic p53 gene therapy in combination with radiation results in human tumor regression. *Tumor Targeting* **4:**92–104.

[5] Xu L, Tang WH, Huang CC, Alexander W, Xiang LM, Pirollo KF, Rait A, Chang EH (2001). Systemic p53 gene therapy of cancer with immunolipoplexes targeted by anti-transferrin receptor scFv. *Mol Med.* **7:**723–734.

[6] Xu L, Huang C-C, Huang W-Q, Tang W-H, Rait A, Yin Y, Cruz I, Xiang L-M, Pirollo K, Chang EH (2002). Systemic tumor-targeted gene delivery by anti-transferrin receptor scFv-immunoliposomes. *Mol Cancer Ther.* **1:**337–346.

[7] Rait A, Pirollo KF, Xiang LM, Ulick D, Chang EH (2002). Tumor-targeting, systemically delivered antisense HER-2 chemosensitizes human breast cancer xenografts irrespective of HER-2 levels. *Mol Med.* **8:**476–487.

[8] Rait A, Pirollo KF, Ulick D, Cullen K, Chang EH (2003). HER-2-targeted antisense oligonucleotides result in sensitization of head and neck cancer cells to chemotherapeutic agents. *Ann N Y Acad Sci.* **1002:**1–12.

[9] Cristiano RJ, Curiel DT (1996). Strategies to accomplish gene delivery via the receptor-mediated endocytosis pathway. *Cancer Gene Ther.* **3:**49–57.

[10] Cheng PW (1996). Receptor ligand-facilitated gene transfer: Enhancement of liposome-mediated gene transfer and expression by transferrin. *Hum Gene Ther.* **7:**275–282.

[11] Keer HN, Kozlowski JM, Tsai YC, Lee C, McEwan RN, Grayhack JT (1990). Elevated transferrin receptor content in human prostate cancer cell lines assessed in vitro and in vivo. *J Urol.* **143:** 381–385.

[12] Rossi MC, Zetter BR (1992). Selective stimulation of prostatic carcinoma cell proliferation by transferrin. *Proc Natl Acad Sci USA.* **89:**6197–6201.

[13] Elliott RL, Elliott MC, Wang F, Head JF (1993). Breast carcinoma and the role of iron metabolism. A cytochemical, tissue culture, and ultrastructural study. *Ann N Y Acad Sci.* **698:**159–166.

[14] Thorstensen K, Romslo I (1993). The transferrin receptor: Its diagnostic value and its potential as therapeutic target. *Scand J Clin Lab Invest Suppl.* **215:**113–120.

[15] Miyamoto T, Tanaka N, Eishi Y, Amagasa T (1994). Transferrin receptor in oral tumors. *Int J Oral Maxillofac Surg.* **23:**430–433.

[16] Ponka P, Lok CN (1999). The transferrin receptor: Role in health and disease. *Int J Biochem Cell Biol.* **31:**1111–1137.

[17] Haynes BF, Hemler M, Cotner T, Mann DL, Eisenbarth GS, Strominger JL, Fauci AS (1981). Characterization of a monoclonal antibody (5E9) that defines a human cell surface antigen of cell activation. *J Immunol.* **127:**347–351.

[18] Batra JK, Fitzgerald DJ, Chaudhary VK, Pastan I (1991). Single-chain immunotoxins directed at the human transferrin receptor containing *Pseudomonas* exotoxin A or diphtheria toxin: Anti-TFR(Fv)-PE40 and DT388-anti-TFR(Fv). *Mol Cell Biol.* **11:**2200–2205.

[19] Jain RK, Baxter LT (1988). Mechanisms of heterogenous distribution of monoclonal antibodies and other macro-molecules in tumors: Significance of elevated interstitial pressure. *Cancer Res.* **48:**7022–7032.

[20] Wolfert MA, Schacht EH, Toncheva V, Ulbrich K, Nazarova O, Seymour LW (1996). Characterization of vectors for gene therapy formed by self-assembly of DNA with synthetic block copolymers. *Hum Gene Ther.* **7:**2123–2133.

[21] Dunlap DD, Maggi A, Soria MR, Monaco L (1997). Nanoscopic structure of DNA condensed for gene delivery. *Nucleic Acids Res.* **25:**3095–3101.

[22] Kawaura C, Noguchi A, Furuno T, Nakanishi M (1998). Atomic force microscopy for studying gene transfection mediated by cationic liposomes with a cationic cholesterol derivative. *FEBS Lett.* **421:**69–72.

[23] Choi YH, Liu F, Choi JS, Kim SW, Park JS (1999). Characterization of a targeted gene carrier, lactose–polyethylene glycol-grafted poly-L-lysine and its complex with plasmid DNA. *Hum Gene Ther* **10:**2657–2665.

[24] Diebel CE, Proksch R, Green CR, Neilson P, Walker MM (2000). Magnetite defines a vertebrate magnetoreceptor. *Nature.* **406:** 299–302.

[25] Rasa M, Kuipers BWM, Philipse AP (2002). Atomic force microscopy and magnetic force microscopy study of model colloids. *J Colloid Interface Sci.* **250:**303–315.

[26] Yu W, Pirollo KF, Yu B, Rait A, Xiang L, Huang W, Zhou Q, Ertem G, Chang EH (2004). Enhanced transfection efficiency of a systemically delivered tumor-targeting immunolipoplex by inclusion of a pH-sensitive histidylated oligolysine peptide. *Nucleic Acids Res.* **5**.

[27] Alisauskus R, Wong GY, Gold DV (1995). Initial studies of monoclonal antibody PAM4 targeting to xenografted orthotopic pancreatic cancer. *Cancer Res.* **55:**5743s–5748s.

[28] Foo JJ, Chan V, Liu KK (2003). Contact deformation of liposome in the presence of osmosis. *Ann Biomed Eng.* **31:**1279–1286.

[29] Xu L, Frederick P, Pirollo K, Tang W, Rait A, Xiang L, Huang W-Q, Chang EH (2002). Self-assembly of a virus-mimicking nanostructure system for efficient tumor-targeted gene delivery. *Hum Gene Ther.* **13:**469–481.

[30] Freedman M, Sarcone A, Pirollo KF, Lin C, Chang EH (2001). Ultrasound images of implanted tumors in nude mice using Sono-CT® correlated with MRI appearance. *SPIE Medical Imaging: Physiology and Function from Multidimensional Images.* **4321:**163–167.

[31] Wisner ER, Weichert JP, Longino MA, Counsell RE, Weisbrode SE (2002). A surface-modified chylomicron remnant-like emulsion for percutaneous computed tomography lymphography: Synthesis and preliminary imaging findings. *Invest Radiol.* **37:** 232–239.

[32] Winter PM, Morawski AM, Caruthers SD, Fuhrhop RW, Zhang H, Williams TA, Allen JS, Lacy EK, Robertson JD, Lanza GM, Wickline SA (2003). Molecular imaging of angiogenesis in early-stage atherosclerosis with alpha(v)beta3-integrin-targeted nanoparticles. *Circulation.* **108:**2270–2274.

[33] Morawski AM, Winter PM, Crowder KC, Caruthers SD, Fuhrhop RW, Scott MJ, Robertson JD, Abendschein DR, Lanza GM, Wickline SA (2004). Targeted nanoparticles for quantitative imaging of sparse molecular epitopes with MRI. *Magn Reson Med.* **51:**480–486.